Observations of X-ray Counterparts to Gamma-ray Bursts in RXTE's All-Sky Monitor

by

Donald Andrew Smith

B.A., Physics, The University of Chicago (1992)

Submitted to the Department of Physics
in partial fulfillment of the requirements for the degree of

Doctor of Philosophy of Physics

at the

MASSACHUSETTS INSTITUTE OF TECHNOLOGY

September 1999

Author .....
Department of Physics
August 11, 1999

Certified by .....
Hale V. D. Bradt
Professor of Physics
Thesis Supervisor

Accepted by .....
Thomas J. Greytak
Associate Department Head for Education

Observations of X-ray Counterparts to Gamma-ray Bursts in RXTE's All-Sky Monitor

by

Donald Andrew Smith

Submitted to the Department of Physics
on August 11, 1999, in partial fulfillment of the
requirements for the degree of
Doctor of Philosophy of Physics

Abstract

In this thesis, I report on a system I designed and implemented to rapidly indentify and localize new transient X-ray sources observed by the All-Sky Monitor (ASM) on the Rossi X-ray Timing Explorer (RXTE). I used this system to identify fourteen Gamma-Ray Bursts (GRBs). Eight of these events were found in archived ASM observations from the first 1.5 years of operation, but the rest were detected and reported within 2 – 32 hours of the event. In thirteen of the fourteen cases, I was able to provide error boxes with a reliable confidence level. I report here on the ASM instrument, the system to identify new X-ray sources, the ASM localization capability, the current state of the field of GRB studies, the thirteen GRB positions, and fourteen GRB light curves. I interpret these observations in the context of the Synchrotron Shock Model for GRB emission.

Thesis Supervisor: Hale V. D. Bradt
Title: Professor of Physics

Acknowledgments

I'd like to thank my advisor, Prof. Hale Bradt, for his support, encouragement, criticism, and confidence. Dr. Al Levine has been with me every step of the way, and I've appreciated his thorough attention to detail and his skill at cutting to the heart of the topic at hand.

The most rewarding aspect of this project has been working as part of the ASM team. In addition to providing an opportunity to participate in an exciting scientific endeavor, the group fostered an atmosphere of cooperation, collaboration, and friendliness. I'd like to thank Hale, Al, Ron Remillard, Ed Morgan, Wei Cui, and Deepto Chakrabarty for creating such a fun and productive working atmosphere.

When I first arrived at MIT, I shared a small room with three other graduate students, Robert Shirey, Chris Becker, and Charlie Collins. Although we eventually moved to larger quarters and all three of them have since graduated, I could not have made it through this program without their help and camaraderie. Robert Rutledge, Derek Fox, Jefferson Kommers, and Patrick Wojdowski have also been wonderful friends and colleagues. Thanks also to Linqing Wen and Mike Muno for joining the ASM team and contributing to the effort. I have greatly appreciated the support, advice, and assistance of Peggy Berkovitz.

I'd like to thank Dale Frail and Shri Kulkarni for giving me the opportunity to travel to exotic places, see kangaroos and learn the basics of radio astronomy. I'd also like to thank Scott Barthelmy, Kevin Hurley, Garrett Jernigan, Luigi Piro, Marco Feroci, and Frank Marshall for their friendly willingness to share data and time to make the ASM more useful as a GRB-chasing tool.

Thanks to the Bab5 crew: David Bogartz, Alana and Alysia Parkes, Elizabeth Rogers, Kaj Telenar, and Christine Parker, for all fun evenings of food and friendship. Thanks also to my friends through the Beacon Hill Friends House extended community, who are too numerous to name, but are none the less wonderful.

Lastly and most importantly, I'd like to thank my mom and dad, for raising me with the curiosity to seek, the confidence to dream, and the passion to know.

Contents

List of Figures

List of Tables

Chapter 1

Introduction

Gamma-Ray Bursts (GRBs) are brief ($< 10^3$ s), intense flares of electromagnetic radiation that transmit the majority of their energy flux above 100 keV. While they are active, their peak emission usually dwarfs the integrated flux from the entire rest of the sky. They appear to come from completely random celestial locations at completely random times, at an average frequency of once a day. No one knows exactly what causes them, and for many years there was vigorous debate over whether they originated in our solar system, in our galaxy, or halfway across the visible universe. Until a few years ago, no unambiguously identified counterparts had been observed at wavelengths longer than X-rays, and no prolonged intervals of emission beyond the initial burst had ever been observed at any wavelength.

It has long been recognized that rapid, accurate positions would be necessary to convincingly identify a GRB counterpart at long wavelengths. This goal was first achieved through the Italian-Dutch satellite *BeppoSAX* on February 28, 1997, when the Wide-Field Camera (WFC) was used to determine an arcminute localization of a GRB within a few hours of the event, and rapidly-executed follow-up observations with X-ray and optical telescopes detected a fading source within the WFC error circle. This late-time emission was promptly dubbed the "afterglow" of the GRB. Similar rapid follow-up observations for a GRB on May 8, 1997, yielded not only

the first-ever detection of a counterpart at radio wavelengths, but also the first-ever determination of a cosmological redshift associated with a GRB, thus settling the decades-old debate over the distance to GRB events.

For many years, the "Soft Gamma Repeaters", or SGRs, were not recognized as a separate class of objects from the GRBs. Now they are understood to have a very different origin from the "classical GRBs". I explain, briefly, the difference between SGRs and GRBs in Chapter 2, but the work presented in this thesis focuses solely on classical GRBs.

This thesis presents a project I developed to use the All-Sky Monitor (ASM) on the *Rossi X-ray Timing Explorer* to complement the *BeppoSAX* program and to provide rapid GRB locations to arcminute accuracy. The ASM was designed and constructed at MIT, by a team that included Prof. Hale Bradt, Dr. Alan Levine, Dr. Ron Remillard, and Dr. Ed Morgan. The instrument consists of three position-sensitive proportional counters (PSPCs) mounted on a rotating base. Through the regular scans of its normal operation, the ASM allows the measurement of the intensity and spectral states of around 300 known X-ray sources, several times a day, down to a limiting intensity of approximately 15 mCrab (1.5–12 keV). The ASM has been in operation at an average duty cycle of approximately 40% since March 1996.

Occasionally, the X-ray portion of a GRB is detected by the ASM. I have developed software to rapidly determine and distribute the location of any GRBs thus detected. The primary goal of this project was to provide the scientific community with useful data for follow-up searches for afterglow emission. The ASM data have also provided useful timing and spectral data to study the relation between the GRB emission above and below 15 keV.

1.1 Overview of this Work

I joined the All-Sky Monitor Team on the *Rossi X-ray Timing Explorer* when I arrived to begin my graduate studies at MIT in August of 1993. I initially assisted in pre-flight testing and calibration of the instrument. Specific projects included correcting for the non-linear effects of analog to digital conversion on the measurement of the position of low-energy photons, as well as measuring the distortion of the detector resolution when radiation is not normally incident on the detector. I also assisted Drs. Levine and Remillard in developing the software to be used for the analysis of the data recorded in flight.

Since the launch of *RXTE*, I have been involved in monitoring the health and behavior of the instrument. I have developed a system of software (described in Chapter 5) to detect and localize new transient sources in the ASM data as quickly as possible. These efforts have led to the discovery of X-ray novae and other transients [145, 149, 146, 151], in addition to the Gamma-ray bursts that are the main topic of this thesis. I have also published papers on (1) the rapid oscillations seen in a thermonuclear burst from the low-mass X-ray binary KS 1731–260 [150] and (2) the location of a new Soft Gamma Repeater, SGR 1627–41, and its possible association with a supernova remnant [148].

The remainder of this thesis is structured as follows: Chapter 2 provides an overview of the field of GRB studies and how the dramatic recent discoveries have changed the current understanding of these events. Chapter 3 describes the ASM, its operation, and its data modes.

Chapter 4 describes the calibration of the ASM position-determining ability. This work culminates in a set of functions that assign a reliable confidence limit to an error box size for a single detection of a new X-ray source. Chapter 5 uses these functions to determine the positions of thirteen GRBs discovered in the ASM data. The contents of Chapters 4 and 5 form the bulk of an article that has been accepted for publication by the Astrophysical Journal [147].

Chapter 6 presents a summary of the most popular current model for understanding GRB emission, the "fireball" model, and predicts what we might expect to see in ASM observations of GRBs. Chapter 7 presents the 2–12 keV X-ray light curves for the GRBs of Chapter 5 and compares them with γ-ray count rates when available. The light curve for a fourteenth GRB which could not be localized accurately is also included here.

Several of the well-localized GRBs discovered in this work were not identified until a year or more after the events, so it was not feasible to search for fading optical counterparts to these GRBs. However, long-lived radio emission has been observed from several GRBs, and I proposed to work in collaboration with Dr. Dale Frail (NRAO) and Dr. Shri Kulkarni (CalTech) to search for long-lived radio afterglow from archival ASM-localized GRBs. Chapter 8 reports on the three candidates we detected. Finally, Chapter 9 summarizes the main results and conclusions of this work.

1.2 Terms and Units

Gamma-Ray Bursts are commonly identified by the year, month, and day (in Universal Time) on which they are recorded at Earth-orbiting satellites (e.g. GRB 970815). If multiple bursts are detected on the same day, the brightest one is designated GRB YYMMDD, while the second-brightest is GRB YYMMDDb, the third-brightest is GRB YYMMDDc, and so on.

In this thesis, I follow the convention, common in X-ray astronomy, of referencing a high-energy photon's place in the electromagnetic spectrum by its energy in *kilo-electron-volts* (keV). When speaking of observations in radio wavebands, however, I follow the standard convention and reference by frequency. Fluxes and fluences in the X-ray and Gamma-ray regimes are reported in C.G.S. units such as erg s^{-1}, but radio fluxes are reported in units of the Jansky (1 Jy = 10^{-23} erg cm^{-2} s^{-1} Hz^{-1}).

It is common in X-ray and Gamma-ray astronomy to report the photon flux of a source in units of "Crabs". This convention takes advantage of the fact that the energy spectrum of the Crab nebula is known to be a simple time-invariant power law within the relevent energy ranges. The photon flux density at Earth (0.1–100 keV) is given by

$$\frac{dN}{dE} = 10 \left(\frac{E}{1 \text{ keV}}\right)^{-2.05} e^{-\sigma(E) n_H} \text{ photons cm}^{-2} \text{ s}^{-1}, \tag{1.1}$$

where $\sigma(E)$ is the energy-dependent cross-section for absorption and n_H is the column density along the line of sight [140, 174]. The actual number of counts that will be detected from the Crab per second by a given detector is determined by integrating this density times the response of the detector ($\equiv \mathcal{F}(E)$ cm^2) over the energy range to which the detector is sensitive (between E_1 and E_2):

$$N = \int_{E_1}^{E_2} \mathcal{F}(E) \frac{dN}{dE} dE \text{ photons s}^{-1}. \tag{1.2}$$

The count rate detected from a source is therefore converted into units of "Crabs" through division by N. If a source produces $m \times N$ counts, or m Crab, one can approximate its intrinsic energy flux by integrating Equation 1.1 times $m \times E$ between E_1 and E_2. The approximation is valid in so far as the unknown source has a Crab-like spectrum and a similar intervening absorption column.

Dates are most often given in Coordinated Universal Time (UTC), which includes any necessary leap seconds. They are usually expressed in terms of year, month, day, hour, minute, and second. Sometimes it is convenient to use the Modified Julian Date (MJD), which is 2,400,000.5 days less than the Julian Day (JD). The Julian standard gives the time elapsed since the Greenwich mean noon on 1 January 4713 BCE. Note, then, that MJD begins each day at Greenwich mean midnight, as does the civil usage of Universal Time, while JD begins each day at noon.

Source locations on the sky are always reported as equatorial right ascension and declination for the equinox J2000.0. The values of these angular coordinates will

usually be given in sexigesimal notation, with right ascension normalized to a 24 hour rotation.

Celestial sources of X-rays are named according to several systems. Currently, the practice in high-energy astronomy is to cite the equatorial coordinates of the source, prefaced by an abbreviation of the discovery mission. Hence, XTE J1550-564 is an X-ray source discovered by the *RXTE* at a right ascension of 15 h 50 m and a declination of $-56.4°$ (J2000). An early catalog of sources names sources like GX9+1 or GX354–0 by their galactic coordinates. The first discovered X-ray sources were named according to their constellation (e.g. Scorpius X-1, LMC X-2).

Chapter 2

Gamma-Ray Bursts

The body of accumulated literature on Gamma-Ray Bursts (GRBs) is formidably large. Kevin Hurley maintains a comprehensive bibliography of GRB-related publications on the World Wide Web [65, 66], which on May 10, 1999, contained over 4000 entries. A new publication is added at an average rate of one per day. A thorough treatment of all aspects of GRB science would be impractical and outside the scope of this thesis. This chapter is intended to provide the reader with a brief overview of the history of GRB studies, with particular emphasis on efforts to localize GRB sources and identify counterparts. Chapter 6 will describe in detail the most popular physical model for GRB origins. For more comprehensive reviews of the state of the field in the mid-nineties, see Fishman & Meegan [30] or Hurley [64] and references therein.

2.1 Discovery and Early Developments

The first known GRB event was recorded with the *Vela IV* set of satellites on 1967 July 2 [79], although the discovery was not published until 1973 [81]. The *Vela* instruments were designed to detect gamma radiation from the fission of a nuclear explosion in space [79]. The temporal structure of the observed bursts (of which there

were several) was poorly resolved in the *Vela IV* instruments, but with the *Vela V* and *VI* satellites, sixteen further events were discovered and identified clearly to be of celestial origin [81, 79].

It was recognized immediately that the differences between the arrival times of a given burst at various GRB detectors yield information about the location of the origin of the burst [81]. The distance to the burst is much larger than the distance between two GRB detectors within the solar system, so the burst emission will travel through the solar system as a plane wave. Since the photons from the burst travel at the speed of light, they will traverse the distance between two satellites (d) in a time $\Delta t = (d/c)\cos\theta$, where θ is the unknown angle between the baseline connecting the two satellites and the direction to the burst source. By measuring d and Δt, one obtains θ with some uncertainty. As shown in Figure 2-1, this measurement defines a small circle (as opposed to a great circle) of finite width (i.e., an annulus) on the celestial sphere. The burst must have originated from some point within this annulus.

The width of the annulus is determined by how well the relative positions of the spacecraft are known, as well as the accuracy to which the delay of the burst can be determined. The error in θ depends inversely on the length of the baseline, so one would expect that larger distances would lead to narrower annuli. As an example, the error in determining the delay of the burst arrival at BATSE relative to the arrival time at *Ulysses* is at least 125 ms [68]. The contribution of this error to the width of the annulus will be less than an arcminute if $d\sin\theta \gtrsim 10^8$ km ($\sim$ 1 AU). Satellite positions are generally known to within a few km, so at interplanetary distances, the contribution to the error from the uncertainty in d is negligible.

With three well-separated spacecraft, one can restrict the location of the burst to two possible celestial positions. If a coarse localization is available by some other method, or if the Earth occults one of the two GRB position candidates from one of the satellites, one of these two locations can be eliminated. Alternately additional satellites can be included to generate more annuli, which for well-separated baseline

configurations will only converge on one location.

This method has been used over the last thirty years to obtain GRB positions. GRB detectors have been placed on solar system satellite missions to form the Interplanetary Network (IPN), which includes both earth-orbiting satellites like the initial *Vela* satellites, the KONUS experiment on *WIND*, the *Solar Maximum Mission*, *HEAOs 1 & 3*, *Prognoz*, and *Ginga*, as well as the truly interplanetary missions such as the *Near Earth Asteroid Rendezvous* (*NEAR*) satellite, the *Mars Observer*, the *Pioneer Venus Orbiter* (*PVO*), the *International Cometary Explorer*, and *Ulysses*.

Instruments on board *PVO*, *Ulysses*, *NEAR*, and others have provided long baselines, but not all of these instruments functioned simultaneously. At its height between 1978 and 1980, twelve satellites carrying GRB detectors extended the IPN throughout the inner solar system [79]. Ten of these detectors observed the enormous flux from the famous March 5, 1979, event, yielding multiple annuli with an intersection region only 0.1 arcminutes^2 in area [13]. (This event turned out to be from an SGR, not a GRB, but the localization technique is identical.) In contrast, during the interval from 1996 to 1999, usually only the *Ulysses* detector was available at interplanetary distances to compare with Earth-orbiting satellites.

The main drawback to the IPN technique is that it takes a long time to produce a localization. Data must be telemetered from far-flung missions and coordinated between different projects and countries. Even today with fast and reliable internet connections, IPN positions are often only available a few days after the initial event. Early efforts yielded catalogs that were published up to years after the events they describe [3, 48, 80]. Catalogs like these provided localizations for a few hundred GRBs (including SGR events), over the decades since 1967, but only around forty error boxes with an area less than 100 arcmin^2. Deep searches for counterparts at other wavelengths such as radio [137], infrared [138], optical [109], and X-ray [112] (to name only a few of many efforts) were unsuccessful.

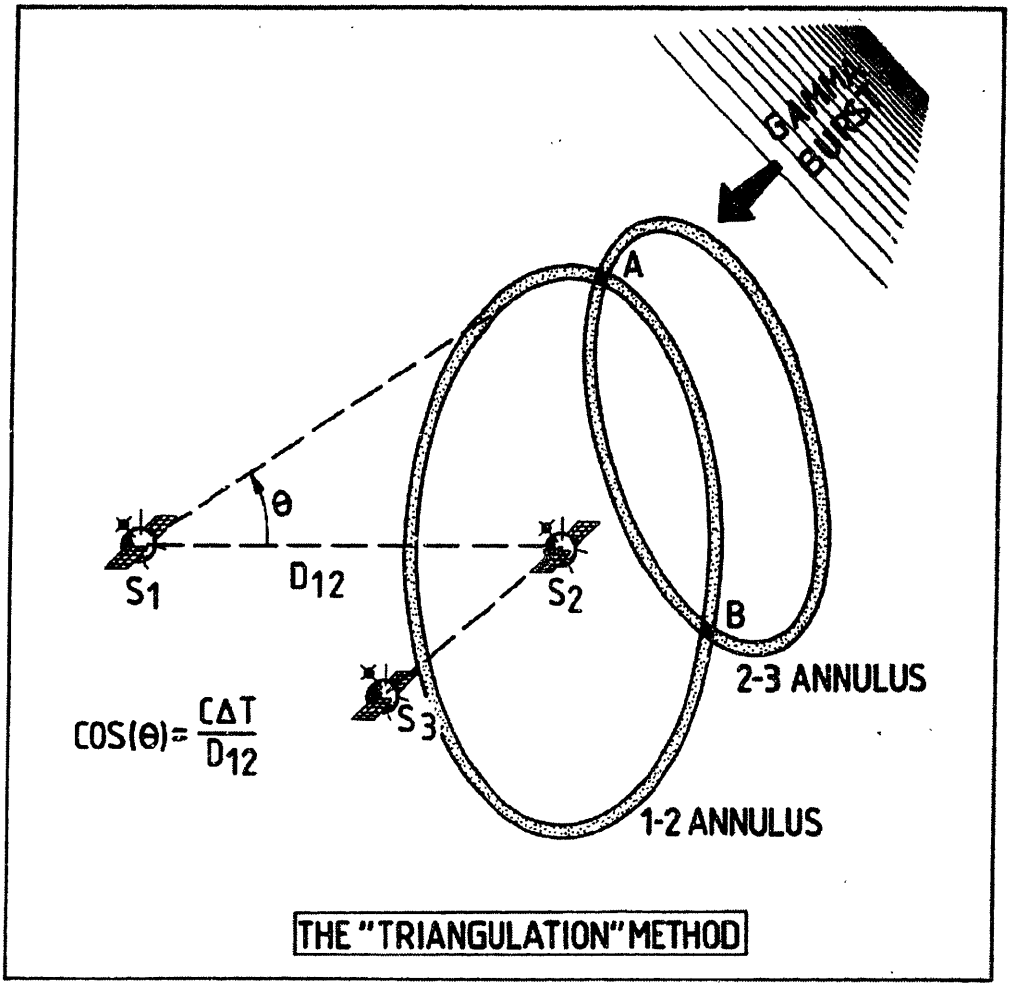

Figure 2-1 A diagram explaining the IPN triangulation method for GRB localization. The figure is from the IPN WWW page [67]. The difference in burst arrival times between two satellites determines the angle (θ) between the vector $\vec{D}_{12}$ that points along the line between the two satellites' positions and the vector that points to the burst source. Since this technique only constrains a single angle, the burst may lie anywhere along a small circle on the celestial sphere. The vector $\vec{D}_{12}$ between the two spacecraft points to the center of the circle, and θ is the angular radius of the circle. Errors in Δt and D_{12} spread the circle out to an annulus. With three well-separated spacecraft, one obtains two possible celestial locations (A) and (B) for the burst. The third possible annulus (1-3; not shown) will intersect the first two at the same positions.

2.2 A Paradigm of Galactic Origin

Early models for the origins of GRBs quickly focussed on galactic neutron stars as the progenitors of these events (e.g. [57, 153]). GRBs had been observed to vary dramatically in flux on ms time scales (e.g. [91]), which demanded small emitting regions. The fluences of the brightest events were on the order of 10^{-4} ergs cm^{-2} [59] (See also Fig. 2-4), which, if placed at extragalactic distances greater than 10^{28} cm, demanded energy budgets in excess of 10^{52-53} ergs, a number that was felt to be unacceptably high [59]. Alternate theories suggesting massive explosions in distant galaxies (e.g. [14, 119]) seem to have been largely discounted.

The picture was further complicated by the recognition in the late 1980s that a subclass of burst events had distinctive properties. They were soft, short (< 1 s), and seemed to recur from the same celestial locations. Two sources of these events were identified as galactic objects, with a third object likely in the Large Magellanic Cloud [4, 85, 89]. A fourth object was discovered toward the Galactic Center in June 1998 [172, 73, 148]. The new class of objects was dubbed "Soft Gamma Repeaters" (SGRs). The compactness and energy constraints cited above still applied to the remaining "Classical Gamma-Ray Bursts" (GRBs), so it was presumed that they, too, would prove to originate in or near galactic neutron stars [59].

This expectation was challenged by the developing body of GRB observations. Distributions of dozens of GRBs displayed both isotropy and inhomogeneity. The interpretation of these distributions is demonstrated in Figure 2-2. A uniform spatial density of sources implies that the number of events increases linearly with the volume of the sample space (which increases as the cube of the radius). However, since the observed intensity falls with distance according to the inverse square law, the number of events brighter than some value F (the "brightness" is sometimes parameterized by the peak flux and sometimes by the total fluence from the burst), that is, the cumulative distribution of F, should fall along the function $N(> F) \propto F^{-3/2}$. Such a distribution is labelled "homogeneous".

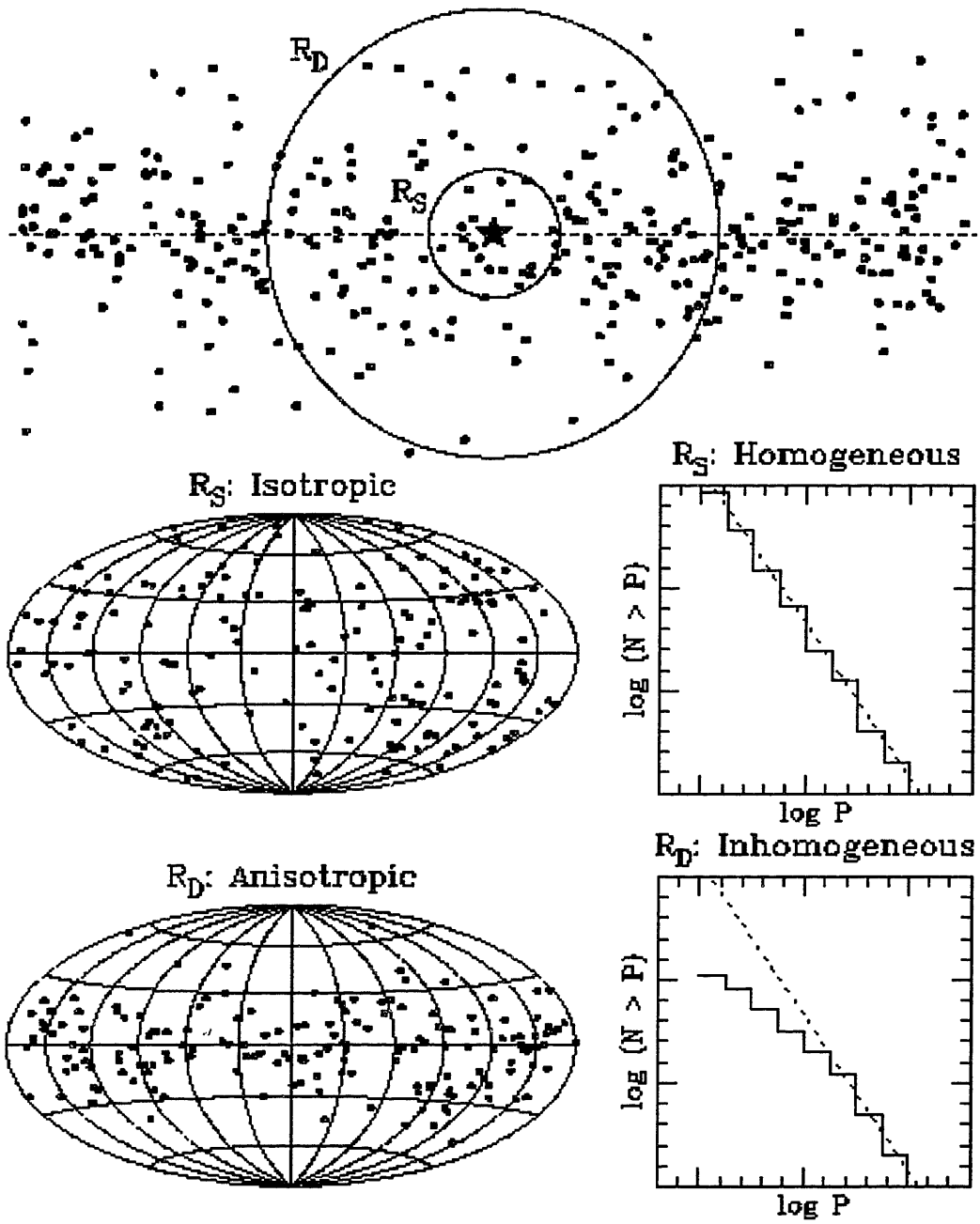

Figure 2-2 An illustration of the implications of a galactic distribution of GRB sources. (From the Marshall Space Flight Center Space Science News WWW page [63].)

A sample of events from such a volume (out to a distance R_S in Figure 2-2, for example) would have an isotropic position distribution and a homogeneous intensity distribution. On the other hand, if the radius of the sample volume extends beyond the region where the sources are uniformly distributed (R_D in Figure 2-2), the number of faint bursts would fall below the 3/2 power law. A distribution of GRB sources within the galactic disc, for example, would result in an anisotropic position distribution clustered along the plane, as well as an inhomogeneous intensity distribution, with fewer faint bursts than the power law would predict.

The earliest GRB catalogs found position distributions consistent with isotropy [3, 48] and fluence distributions with a paucity of faint bursts [6, 101]. This combination implies that the Earth lies at the center of a bounded distribution of objects. The natural distance scales that center on the Earth are either extremely small or extremely large. Some researchers protested that the lack of faint bursts could be due to instrumental sensitivity [60]. Others suggested that the classical GRBs could be coming from a population closer to the Earth than the galactic scale height, while the soft gamma repeaters were much further away: in the galactic bulge or the LMC [79]. It was expected that the data to be collected by the Burst and Transient Source Experiment (BATSE) after its launch in 1991 would either find the "missing" faint bursts with its improved sensitivity, or find clustering of burst positions around the galactic plane with its improved statistics [59].

2.3 BATSE

The Burst and Transient Source Experiment (BATSE) on the *Compton Gamma-Ray Observatory* (*CGRO*) consists of eight uncollimated detector modules that view the entire celestial sphere not blocked by the Earth [32]. Its primary function is to detect and localize GRBs. With more than 2300 GRBs accumulated over eight years of observation [99], the BATSE catalog shows a unambiguously uniform spatial

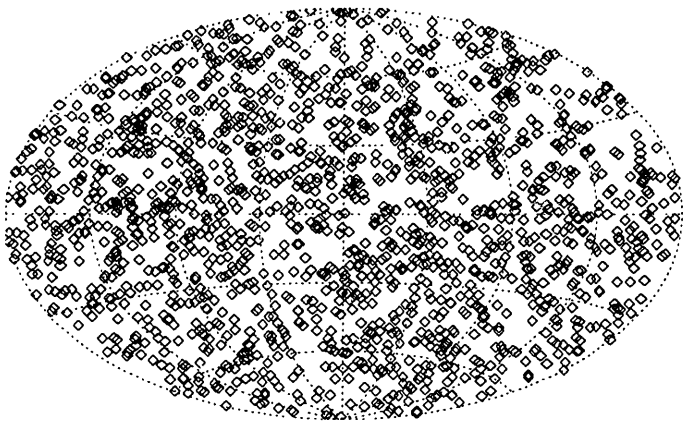

Figure 2-3 The celestial locations of the centers of the 1637 GRB error circles in the BATSE 4B catalog. The coordinate grid indicates Galactic coordinates, with longitude increasing to the left. Compare this location distribution with the examples in Figure 2-2.

distribution (Fig. 2-3) and an inhomogenous fluence distribution (Fig. 2-4).

These results do not lend themselves easily to a galactic model. Clearly the GRB sources are not clustered along the galactic plane. Attempts to posit a source distribution in the galactic halo are confounded by the lack of any clustering around the Andromeda Galaxy [29], which presumably would have its own population of halo GRB sources. However, it is important to note that the data do not exclude the possibility of multiple source populations at various distance scales [97, 98], and it has been claimed that no existing instruments could conclusively settle the question on statistical grounds alone [56].

After firmly establishing the isotropy and inhomogeneity of the GRB distributions, the focus of BATSE GRB observations changed to emphasize providing position information on GRBs as quickly as possible over the newly-formed Gamma-Ray Burst Coordinate Network (GCN), an internet service founded and maintained by Scott Barthelmy at NASA/GSFC. This service is intended to distribute GRB location information worldwide as quickly and efficiently as possible. Although BATSE now

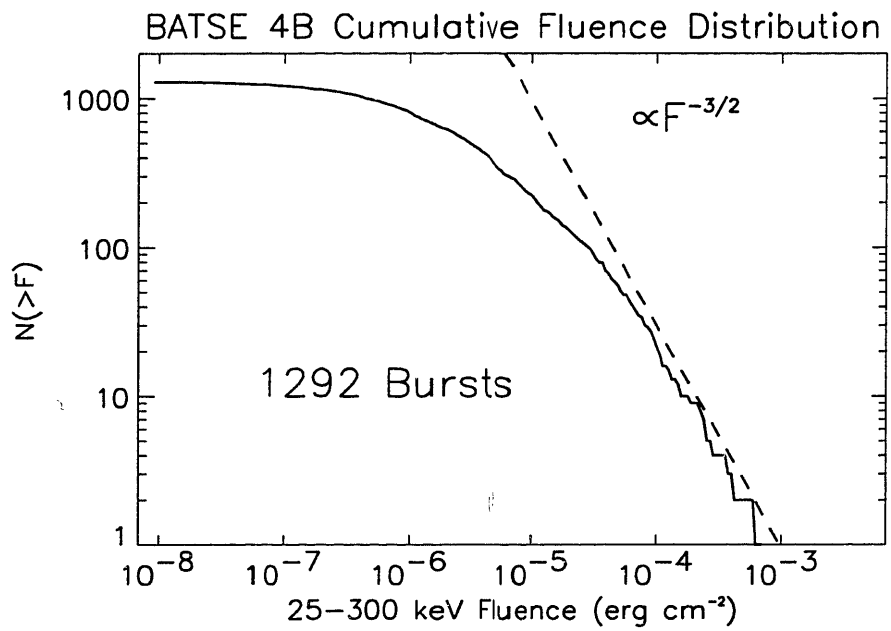

Figure 2-4 The cumulative fluence distribution of GRBs in the BATSE 4B Catalog [118]. Compare this fluence distribution with the examples in Figure 2-2.

alerts the scientific community of a GRB within seconds of the event's onset, the radii of the error circles can be tens of degrees in the first reports. Further processing after the event can reduce the radius for the brightest bursts to a few degrees, but even such circles are far too large for most optical searches.

2.4 The *BeppoSAX* Revolution

On February 28, 1997, a new method of chasing GRBs was introduced. A GRB serendipitously fell within the field of view of the Wide-Field Camera (WFC) on the *BeppoSAX* satellite. The X-ray flash associated with the GRB was localized to within a circle 3′ in radius [123]. Eight hours later this circle was imaged with the *BeppoSAX* Narrow-Field Instruments, and a fading X-ray source was found and localized to within a circle of 50″ in radius [16]. The location of the fading source

was consistent with the WFC position. Both of these positions were widely disseminated among the astronomical community within a few hours, and led to a cascade of reports in the IAU Circulars (25 circulars between Nos. 6572 and 6747), including the first report of a contemporaneous detection of an optical counterpart to a GRB source [160]. These localizations are shown in Figure 2-5.

Further fast accurate positions, provided both by the *BeppoSAX* and ASM/*RXTE* teams, have led to identifications of GRB source counterparts at longer wavelengths. The new wealth of data has enabled scientists to learn more about GRB locations, properties, and behavior. Optical spectroscopy of the fading counterparts of GRB sources and what are thought to be their host galaxies has led to the determination of eight precise cosmological redshifts at the time of this writing. Some were determined from lines in the optical counterpart itself, others were based on the spectrum of the prospective host galaxy. A photometric redshift has been estimated at $z \sim 5$ for GRB 980329 [42]. These results are summarized in Table 2-1. Although there is certainly still room for multiple populations of GRB progenitor objects (GRB 980425 may be an example of a separate class of GRBs [88]), these results conclusively settle the decades-long debate by proving that at least some GRBs must come from cosmological distances.

The All-Sky Monitor was designed to measure the intensities and spectral states of bright galactic sources of X-rays, as well as search for the emergence of transient sources (Chapter 3). A single detection of a bright new source provides a localization in the shape of a long, thin error box (Chapter 4). Multiple detections could constrain the source location to a region a few arcminutes across. After the success of the *BeppoSAX* program, we realized that the ASM could also localize the X-ray counterparts to GRBs. Since the *RXTE* is in constant telemetry contact with the ground, we could even provide a position to arcminute precision within 10 minutes. Unfortunately, nature has not provided us with such an ideal GRB detection since my automated system for identifying new transients and distributing their locations was

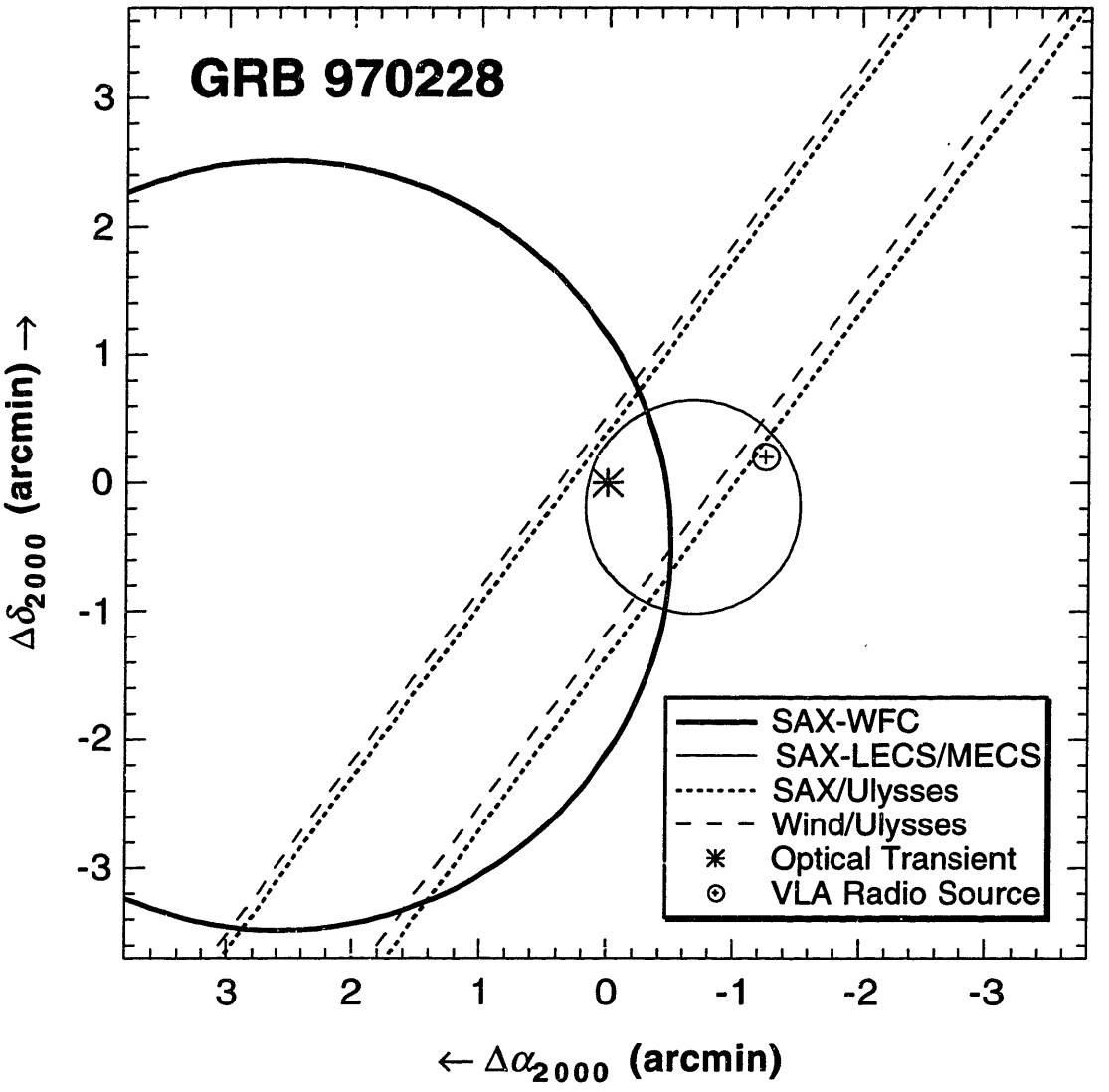

Figure 2-5 Closing in on GRB 970228. This figure courtesy of Marc Kippen (NASA/MSFC), created for [160].

GRB	z	Method	References
970228	0.695	Host	[22]
970508	0.835	Transient	[107, 108]
970828	0.9579	Host	[21, 35]
971214	3.14	Host	[87]
980329	~ 5?	Photometric	[42]
980425	0.0085	Transient	[158]
980613	1.096	Host	[23]
980703	0.966	Transient	[24]
990123	1.60	Transient	[77, 61]
990510	1.619	Transient	[164]
990712	0.430	Transient	[45]

Table 2-1: Redshifts Associated with GRBs

put into operation in August of 1998. Our manual efforts have provided the astrophysical community with five rapid GRB localizations to search for GRB afterglow. Four of these searches would not otherwise have been possible, and they have led to two of the above-mentioned redshifts (GRB 970828 and GRB 980703), as well as the most rapidly acquired X-ray afterglow to date (GRB 970828). The latter burst yielded no measurable optical counterpart, despite deep searches begun less than four hours after the burst.

2.5 The Future

This is a rapidly-changing field, and new discoveries are reported almost monthly. Further progress in all areas of GRB investigation now depends primarily on the rapid and accurate determination of the positions of more GRBs, so as to quickly bring the source positions under the scrutiny of powerful X-ray, optical, and radio telescopes.

The second *High Energy Transient Experiment* (*HETE-II*) will provide the next major increase in the pace of GRB studies. The first *HETE* was lost due to a mal-

function of the launch vehicle, but funds were allocated to rebuild it and try again. *HETE-II* will carry three co-aligned, wide-field telescopes that observe at energies spanning 0.5–500 keV. An on-board computer will calculate GRB positions with an accuracy of 0.1–10′. Internet-capable ground stations around the globe will forward the information to MIT, where a computer will perform additional checks and automatically disseminate a position over the GCN to observers worldwide. A localization should arrive at observers' sites within a few minutes of the burst onset. Mission planners expect *HETE-II* to detect on the order of 30 GRBs per year in its nominal 2-year mission [161]. By combining multiwavelength studies of the bursts themselves with the rapid distribution of accurate positions to others, *HETE-II* will greatly increase the amount of information available about gamma-ray bursts.

Chapter 3

The All Sky Monitor

3.1 The Satellite

The *Rossi X-ray Timing Explorer*, named after pioneering X-ray astronomer Bruno B. Rossi, was launched from Cape Canaveral at 08:48 EST Saturday December 30, 1995. It carries three X-ray telescopes and a sophisticated on-board computer (Fig. 3-1) to study the rapid temporal and spectral behavior of the X-ray sky [11]. The three telescopes are called the Proportional Counter Array (PCA) [75], the High Energy X-ray Timing Experiment (HEXTE) [54], and the All-Sky Monitor (ASM) [94].

The PCA is a set of five Xenon proportional counters that offers a 7000 cm^2 collecting area and moderate spectral resolution (18% at 6 keV) over the range between 2–60 keV. With its large area and the flexible data modes of the on-board processor, the Experiment Data System (EDS), it is suitable for studying the variability of X-ray sources on many different time-scales from tens of microseconds to years. The free-fall time of a particle near ($R \sim 10$ km) a 1.4 $M_\odot$ neutron star is $\sim R/v = \sqrt{R^3/(2GM)} \sim 50$ μs, so this is the temporal resolution one must achieve to observe fluctuations in X-ray emission from matter near the neutron star surface, and the EDS provides time resolution at this level. The large collecting area of the PCA also allows researchers to study the long-term variability of weak X-ray sources such

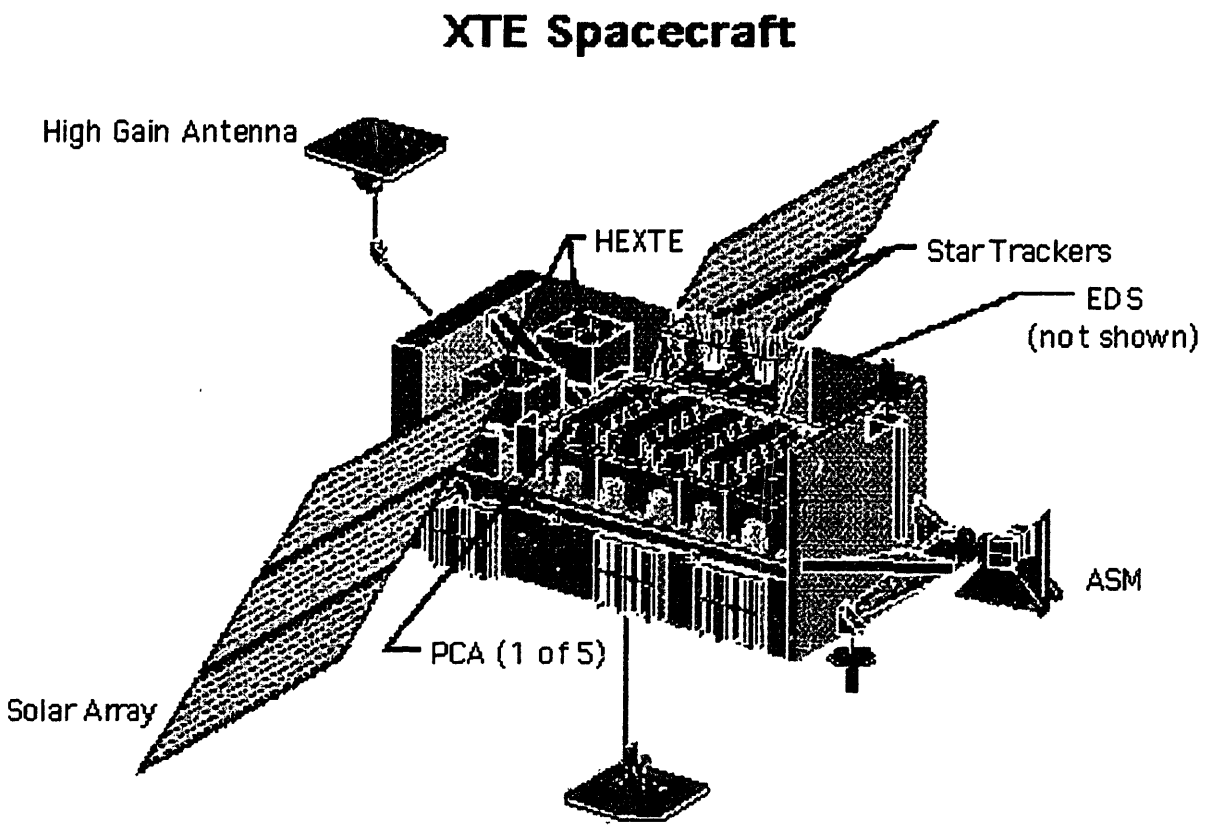

Figure 3-1 The *Rossi X-ray Timing Explorer* spacecraft with instruments and on-board data system.

Figure 3-2 A picture of the assembled All-Sky Monitor, awaiting shipment to GSFC to be built into the *RXTE*.

as the distant active galactic nuclei. The HEXTE is a cluster of phoswitch detectors that extend the energy range observable by *RXTE* up to 150 keV, while providing a comparison with the PCA's response down to 20 keV.

This thesis will focus exclusively on data from the All-Sky Monitor (ASM). The ASM is mounted on the end of the *RXTE*, and continually scans the sky. The ASM team maintains histories of the intensity and spectral state of about 300 known X-ray sources, and we use the near-continuous telemetry contact to search for the emergence of X-ray emission from previously unknown sources. This instrument has not only successfully allowed researchers to schedule efficient observations of active X-ray sources, but its data (100% publically available) have proven useful on their own for furthering the understanding of galactic X-ray sources.

3.2 ASM Physical Construction

The ASM consists of three Scanning Shadow Cameras (SSCs) mounted on a motorized rotation drive (Figs. 3-2 and 3-3). The assembly holding the three SSCs is generally held stationary for a 90-s "dwell", during which data are accumulated. The drive then rotates the SSCs through 6° (one-half of the azimuthal width of an SSC field of view) to the next dwell position, except when it is necessary to rewind the assembly. Each SSC contains a position-sensitive proportional counter (PSPC), a steel chamber filled with a gas mixture of 95% xenon and 5% carbon dioxide at a total pressure of 1.2 atm. X-rays enter the chamber through a 50-μm thick beryllium window with a total surface area of about 80 cm^2 (the effective area is less, as explained below). Each PSPC contains eight resistive anodes of carbon-coated quartz. These permit the measurement of the position of an incident photon along the length of an anode. Twelve metal wires that serve as anticoincidence anodes are located below and to the sides of the position-sensing layer. The position-sensing layer is 1.27 cm deep, and the total depth of the PSPC is 2.54 cm. The steel walls of the counter are held at -1800 V relative to the anodes.

When an X-ray enters the chamber, the photon ionizes one of the xenon atoms. This photoelectron dissipates its energy by ionizing other atoms. The resulting free electrons accelerate toward the anode. When they attain sufficient energy, they, too, ionize atoms along their paths. The total number of electrons deposited onto the anode is roughly proportional to the energy of the incident photon. The relative amounts of current measured at each end of the anode reflect the location of the impact site of the photon event. Thus, both the location and the energy of the incident photon are recorded. Each event detected on exactly one resistive anode is characterized by SSC and anode number, total pulse height, and a one-dimensional position. Each position is recorded as one of 338 electrical position bins. The photon energy is recorded in one of three channels that have the nominal energy ranges of 1.5–3 keV, 3–5 keV, and 5–12 keV.

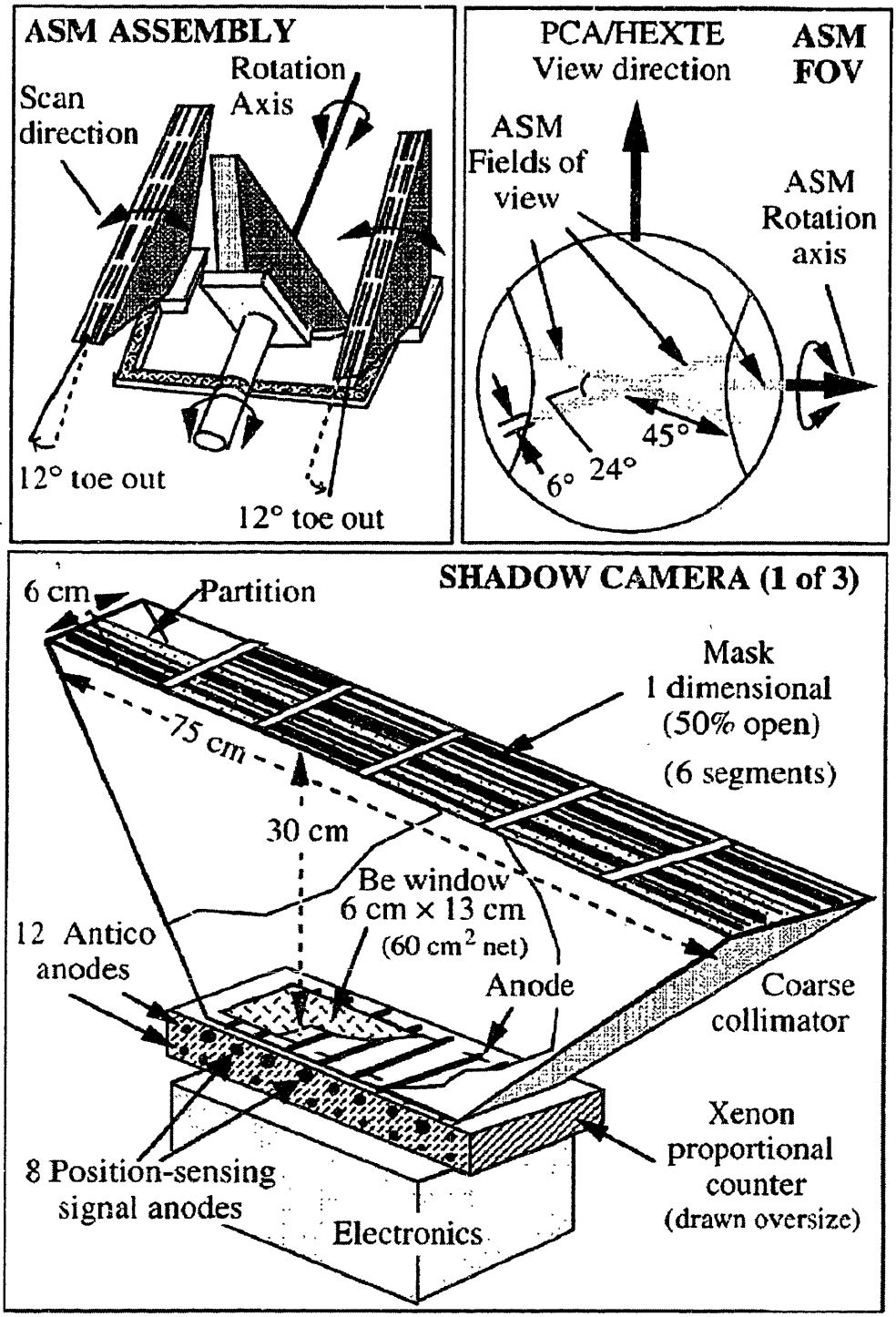

Figure 3-3 Schematic diagram of the construction and mounting of the three SSCs.

Each SSC views a 12° × 110° (FWZI) field through a 74 cm × 8 cm mask mounted on an aluminum collimator 30 cm above the face of the PSPC. Each mask is divided into 6 × 62 elements, where each element is 0.10 cm × 11.1 cm. These elements are chosen to be open slits or closed metal so as to generate six distinct slit-patterns along the length of the mask, although each pattern leaves half of the surface open. Through exhaustive simulations, the exact patterns of open and closed mask elements were chosen to minimize the height of the side lobes in the simulated response function to a source in the FOV.

The long axes of the slits run perpendicular to the anodes in the PSPC. The collimator has an aluminum wall down the center of its long dimension that effectively splits the detector in two, preventing photons that enter the left side of the mask from registering in the right side of the detector. The 31 elements on the right side of the mask repeat the same sequence of open versus closed as the 31 elements on the left side. The six patterns along the length of the mask do not resemble one another.

The SSCs are oriented such that one of them (SSC 3) is co-aligned with the rotation axis of the ASM drive assembly (the vertical axis in Figure 3-2). The other two SSCs point the centers of their fields of view at a mutual celestial location, but the long axes of their FOVs (the axes parallel to the mask slits) are tilted 24° with respect to each other (Fig 3-3).

The total effective area of each PSPC is $\sim$ 30 cm^2. The total surface area of the window is 80 cm^2, but half of the surface is blocked by the mask, and there is a steel support structure above the beryllium that blocks a further $\sim$ 10 cm^2. The effective area must be further reduced by an energy-dependent factor to account for the absorption of X-rays by the window. This factor is different for each SSC because in a late stage of construction, it was decided to add a sealant to the inside of the windows of the detectors which were placed in SSC 2 and SSC 3. This sealant consisted of a thin layer of the plastic polyimide, which in turn had to be coated with a conductive layer of aluminum to preserve the voltage configuration within the

chamber. As a result, SSCs 2 and 3 show stronger absorption in the lowest energy channel. In practice, this effect is accounted for empirically by a normalization factor a, described below in Section 3.3.1.

Also for SSC 2 and 3, the effective area must be further reduced because several of the position-sensitive anodes have failed over the course of the mission. Over time, the continual cascading of electrons onto the anodes will wear away the carbon coating, but this process should take years under normal operating conditions. The carbon coating on one anode in SSC 2 and two anodes in SSC 3 began to be stripped off at a vastly accelerated rate within hours of the initial commencement of operation in January 1996. It was decided to instruct the computer to ignore any signal from those anodes and let the process run its course. Normal operations were underway by March 1996, using the unaffected anodes. A third anode in SSC 3 burned in August 1996. The cause of these losses remains unknown, although impurities in the chamber may have enhanced the already strong electric field and hence triggered electrical breakdown. The large amount of electrical activity on the damaged anodes as they rapidly deteriorated caused the neighboring anodes to age at an accelerated rate. In February 1999, we declared a fourth anode of SSC 3 (anode 6) to have decayed too far to be of further use. This anode lies between two dead anodes, and it was bombarded from both sides during the times of breakdown. The remaining anodes function normally, but the effective areas of SSCs 2 and 3 are reduced by $\sim$13% and $\sim$50%, respectively, due to the loss of collecting area.

3.3 ASM Data Modes and Analysis

Over the course of a typical 90-s observation, a few thousand photons are recorded by each SSC. Although an "event mode" that would preserve the time, energy, and location of each individual photon is currently under development, the standard for the first three years of ASM operation has been to preserve this information only

in three aggregate modes: histograms of photon arrival locations on each position-sensing anode, time-series data recording the total number of photons detected in each one-eighth second time interval, and pulse-height data recording in 64-s accumulations the total response to each photon in 64 energy bins.

3.3.1 Position Histogram Data

For each dwell, the position histograms are used to derive intensities of known sources in the field of view (FOV) as well as to search for evidence of flux from any previously unknown sources. The intensities of known sources are calculated via a fit of model slit-mask shadow patterns to histograms of counts as a function of position in the detector. For each source in the FOV, we use the recorded orientation of the instrument to convert right ascension and declination into θ and ϕ. These angles are defined relative to the direction of the resistive anodes: ϕ lies in a plane parallel to the anodes, while θ lies perpendicular to this plane (Fig. 3-4).

Given the location of a source in θ and ϕ, the slit-mask pattern and the geometry of the instrument determine which parts of which detector anodes will be illuminated by the source. If one source lies further off-axis in ϕ than a second source, their respective illumination patterns will be shifted along the length of the anodes, while differing θ angles will result in different slit patterns illuminating different anodes (Fig. 3-5).

We therefore construct a vector $\vec{v}_s$ for each source s in the FOV. This vector has $338 \times 8 = 2704$ components; one for each position bin along each anode (It is not the two-component vector shown in Figure 3-4 that defines a source's FOV location.). $\vec{v}_s$ has an arbitrary total amplitude, but the relative magnitudes of each component are defined to represent the fractional area of each bin that is exposed to the source. In other words, an fully exposed bin would have a corresponding component of one, while a fully shaded bin would have a component of zero. A half-shaded bin would be normalized to 0.5, and so forth. The overall amplitude of the vector reflects the

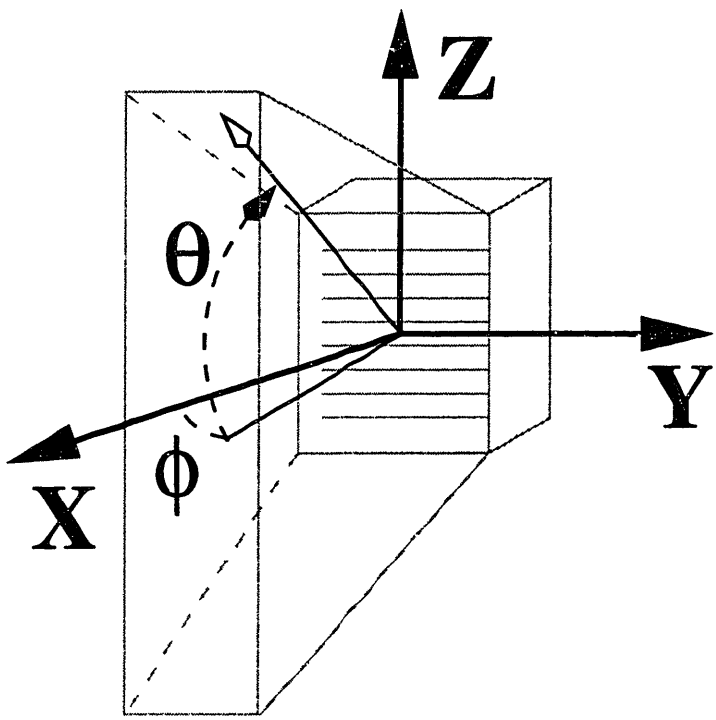

Figure 3-4 This diagram defines a Cartesian coordinate system and associated angles used to describe positions and directions relative to a particular SSC. The coordinate axes are superposed upon a schematic drawing of an SSC which represents the outer shell of the collimator and the proportional counter. The eight parallel lines within the counter represent the resistive anodes which are used to obtain the y coordinates of detected events. The origin of the coordinate system is located at the center of the window of the proportional counter. The x-axis extends through the center of the coded mask so as to point in the direction of the center of the field of view of the SSC. The y-axis points parallel to the resistive anodes, and the z-axis points parallel to the long axis of the mask slits. A direction relative to the SSC may be specified by the angles ϕ and θ, where ϕ is measured in the x-y plane and θ is the angle between the x-y plane and the specified direction. The field of view of the SSC extends over a region defined by $-6° \leq \phi \leq +6°$ and $-55° \leq \theta \leq +55°$ (FWZI). Note that each of the three SSCs has a unique orientation on the ASM (see Figure 1 of [94]).

intensity of the source.

If we define a set of vectors $\{\vec{v}_s\}$ in this manner, then the total shape of the position histogram is the sum of all the vectors for all the sources in the FOV, plus two diffuse components to represent the X-ray and charged particle backgrounds: $\vec{V}_{tot} = \sum_s A_s \vec{v}_s$. The amplitudes A_s of the individual source vectors are determined via a least-squares fit to the position histogram data. An example of the results from such a fit to an observation of Sco X-1 is shown in the middle panel of Figure 3-6.

Once an amplitude for each source in the FOV is determined, it is converted into a measurement of the source's intensity through the application of two multiplicative factors. The transmission function ($\equiv f$), is the fraction of the active detector surface (accounting for any disabled anodes) which is exposed to the source. The normalization factor ($\equiv a$) is an empirically-derived correction factor that depends on the time of the observation, the energy band under consideration, and the position of the source in the FOV. It is derived such that the Crab Nebula maintains a constant count rate, and all three SSCs are normalized to the observed rates for the Crab at the center of the FOV of SSC 1 (Table 3-1). The amplitude from the fit is converted into a total number of counts through multiplication by a/f. Division by the exposure time yields a count rate that represents the source's average intrinsic intensity over this observation.

The second phase of the analysis searches for evidence for the presence of an unknown source in the position histogram data. The residuals from the initial fit for $\vec{V}_{tot}$ are cross-correlated with each of the expected shadow patterns corresponding to one of a set of possible source directions which make up a grid covering the FOV. A peak in the resulting cross-correlation map indicates the possible presence and approximate location of a new, uncataloged X-ray source (Fig. 3-7). Peaks that satisfy certain criteria are analyzed further to confirm the detection and refine the position. For detections of bright sources, the resulting error boxes typically have sizes on the order of $3' \times 3°$ full width at 90% confidence. Detections of new sources

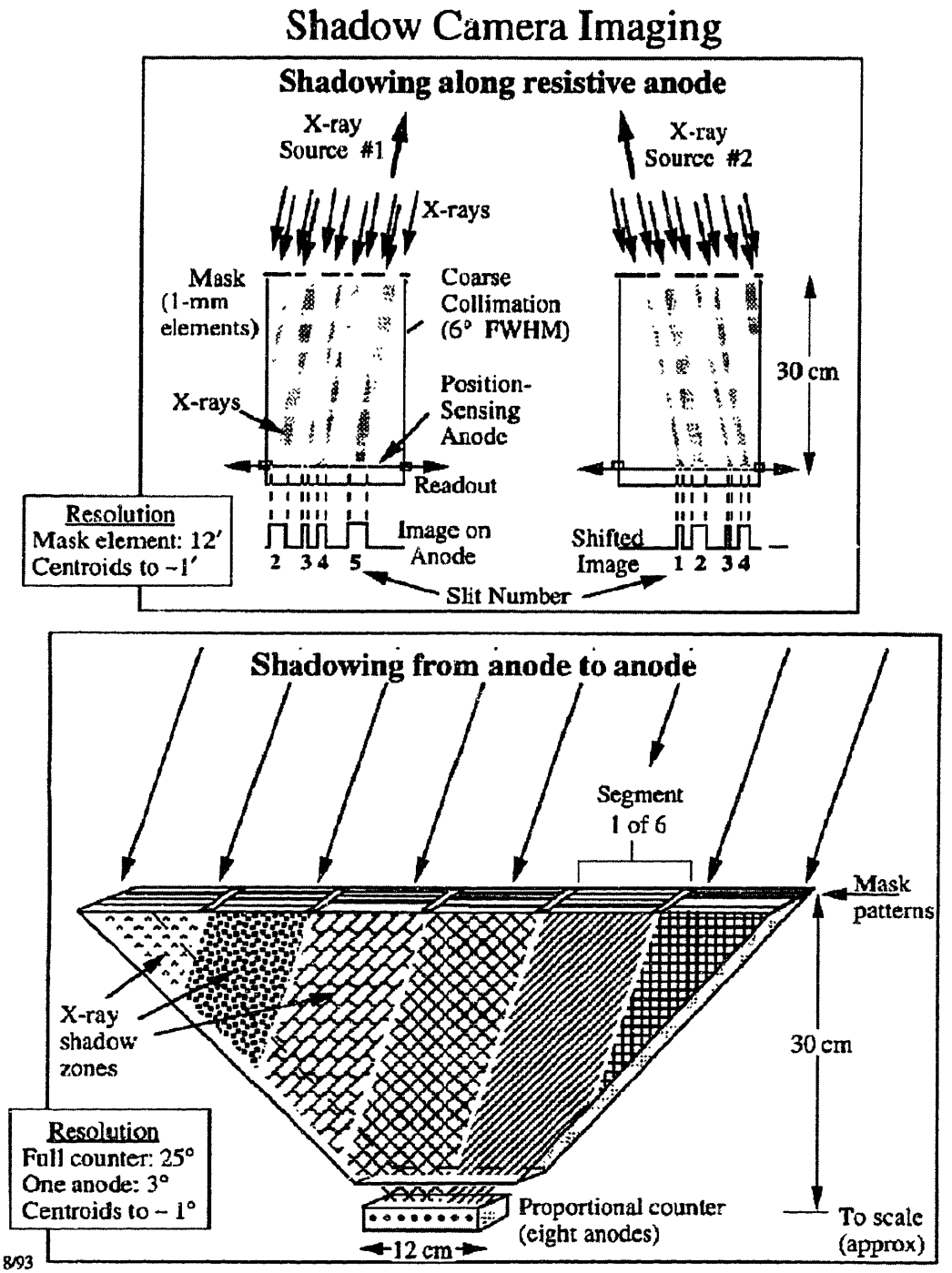

Figure 3-5 Schematic of the effect of source location in ϕ (top panel) and θ (bottom panel) on the position of the slit-mask pattern on the PSPC anodes. The θ-location of a source determines which patterns fall on which wires, while the ϕ-location determines the shift of that pattern along the length of the anode.

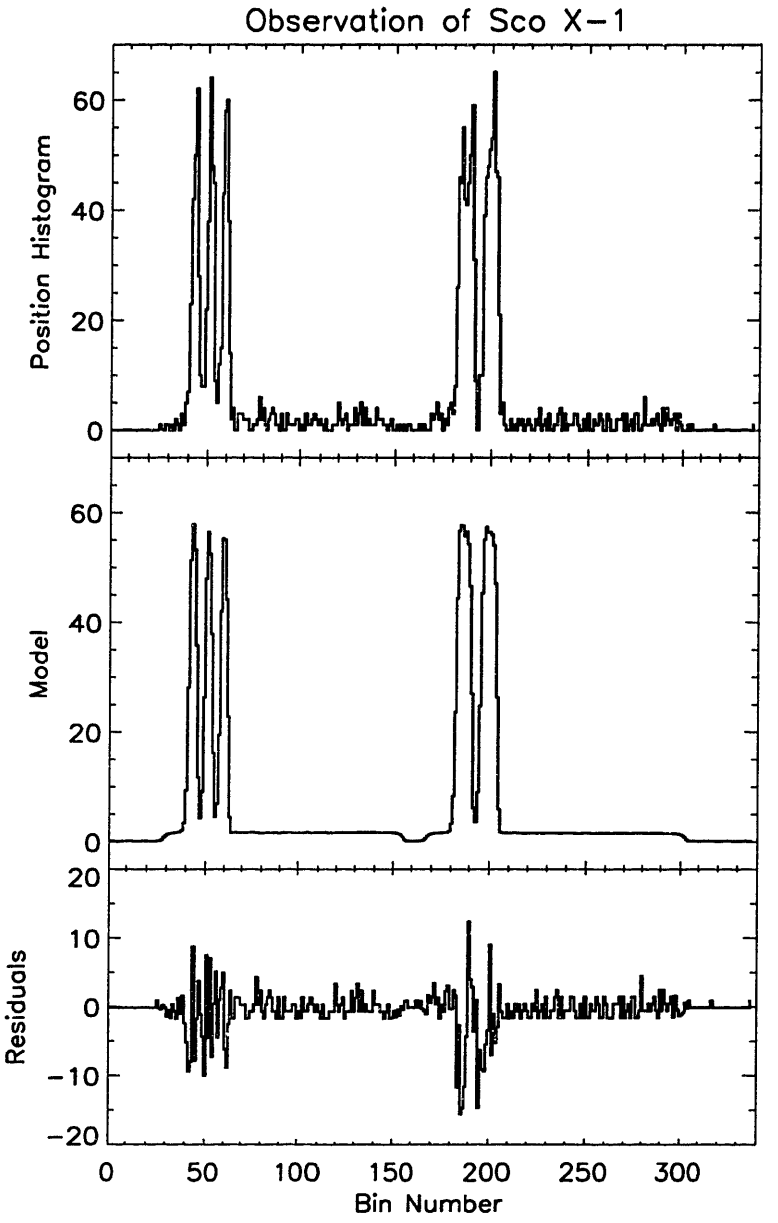

Figure 3-6 The results of a fit for the position histogram data from a single anode in SSC 2. The observation is a 90-s exposure of Sco X-1 at FOV coordinates of $\theta = -11.0°$ and $\phi = -4.3°$. No other detectable point sources are in the FOV. The top panel shows the recorded position histogram data in the 338 bins. The middle panel shows the model derived from a least-squares fit ($\chi^2_r = 1.16$), including components for diffuse backgrounds. The bottom panel shows the difference between the model and the data.

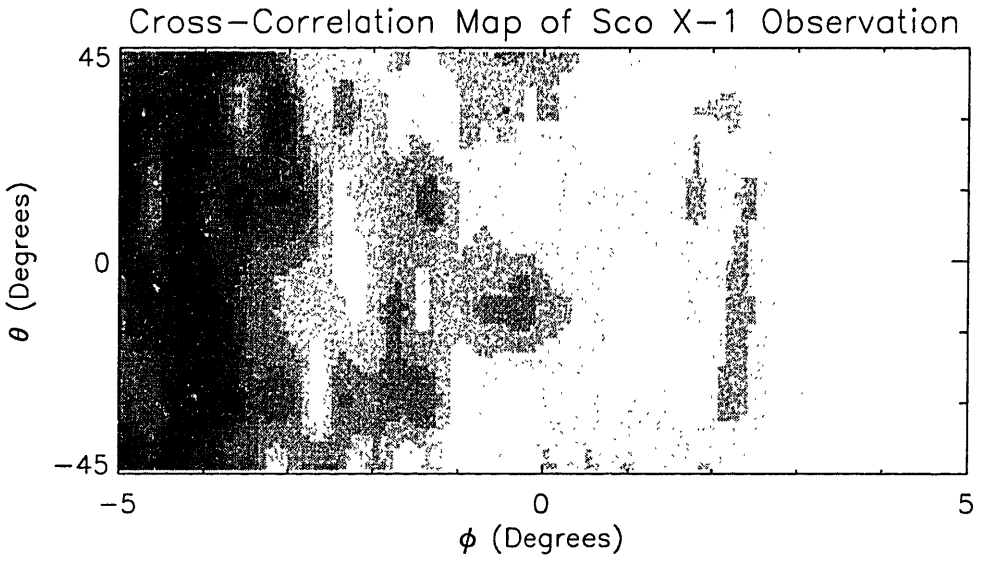

Figure 3-7 An example of a cross-correlation map This image was produced by removing Sco X-1 from the active catalog, then performing a fit on the same SSC and dwell as that shown in Figure 3-6, and finally calculating the cross-correlation coefficient between the residuals from that fit (which still contain the counts from Sco X-1) and the expected response from each point in a 121 × 61 point grid across the FOV. The position of Sco X-1 is at $\theta = -11.0°$ and $\phi = -4.3°$.

in at least two SSCs are preferred because they yield error boxes that cross, thereby constraining the source's location in two dimensions to a diamond-shaped error box, of dimensions $\sim 3' \times 15'$ for bright sources (Chapter 4).

If the model for the expected shadow pattern due to flux from the known sources in the FOV contains errors, the residuals from the fit will still contain contributions from those known sources. When the residuals are cross-correlated with the detector response, the excess counts will yield "ripples" in the map which act as a source of noise in addition to counting statistics. The correct construction of the shadow patterns depends on, among other factors, an accurate calibration of the correspondence between electrical position and physical location within the detector.

The electrical position of an incident photon is derived via application of the charge-division technique. The electrical position is defined as the ratio of the signal

strength measured from one end of the anode to the sum of the signal strengths from both ends. Ideally, the signal strength is proportional to the electrical charge entering the pre-amplifier attached to that end of the anode. The charge deposited on the anode by the cascade of photoelectrons will split according to the total resistance in each direction from the impact site. If the resistivity is uniform across the length of the anode, the fractional charge measured at one end of the anode will be proportional to the fractional position of the impact site along the anode. The correspondence between electrical position and physical location in the SSCs changes as the carbon coating of the resistive anodes is being worn away nonuniformly. We must therefore periodically update our calibration of this correspondence.

To assist in this effort, I identify all observations which have no known X-ray sources in the FOV of each SSC. I sum each of the position histograms from these observations into weekly accumulations. I thus acquire a histogram of counts for each functioning anode that contain only diffuse celestial X-rays and non-X-ray background counts. Figure 3-8 shows summed histograms for anode 6 of SSC 3 and anode 1 of SSC 1 at two different times during the mission. The steel chamber of the PSPC blocks transmission of celestial X-rays around the beryllium window, and there is also a steel support beam running down the center of the window. The electrical positions of the absorption edges as shown in Figure 3-8 correspond to the physical dimensions of the window edges.

Anode 6 of SSC 3 lies between two of the anodes that underwent electrical breakdown early in the mission, as described above. It has therefore been subjected to higher than normal activity. The overall thinning of the carbon coating causes the electrical positions of window edges to stretch, and the fact that the carbon loss is non-uniform leads to jagged bumps and dips in the bright regions of the histogram. The details of these non-uniformities are tracked through fits to the mask pattern responses to Sco X-1 and the Crab, both very bright sources with easily identifiable mask edges. These relations are updated roughly once every six months.

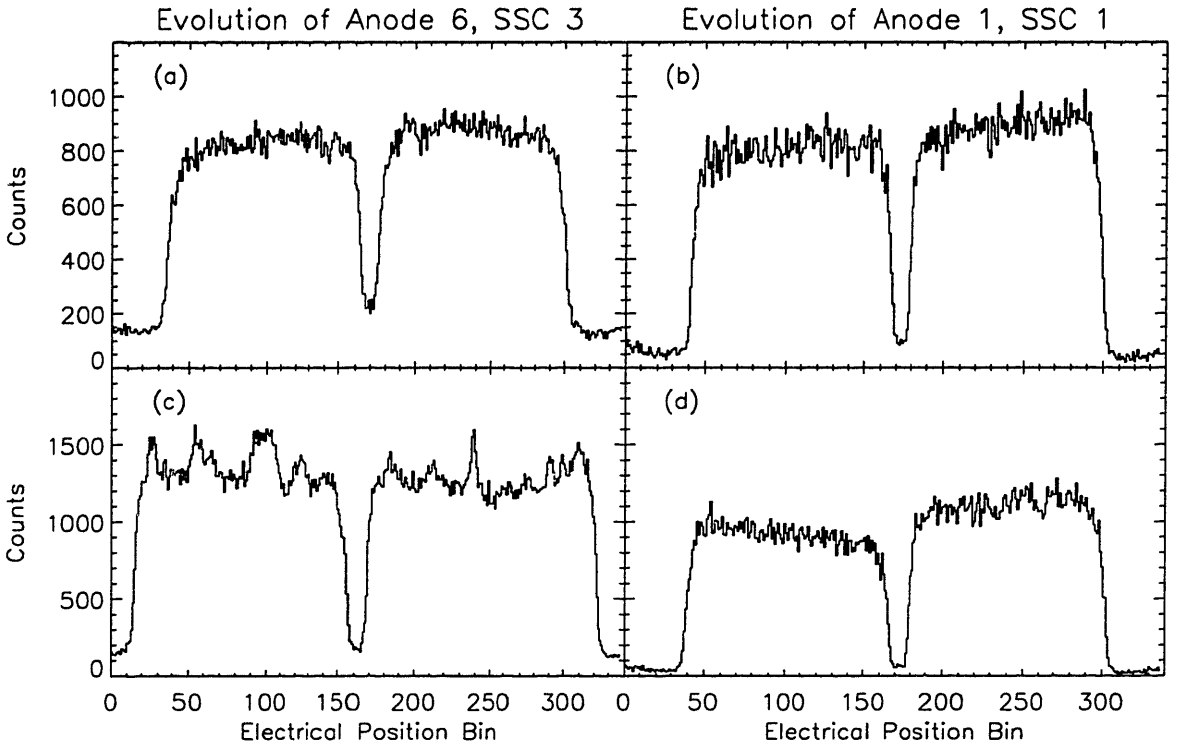

Figure 3-8 One-week sums of the position histogram data from anode 6 of SSC 3 and anode 1 of SSC 1. Only observations with no known discrete X-ray sources in the FOV are included. Panels (a–b) show the interval from March 15–21, 1996, and panels (c–d) show the interval from November 7–13, 1997. The loss of carbon leads to the overall stretching of the window width, while the non-uniformity of that loss leads to the irregularities in the peak counts. Anode 6 of SSC 3 lies between two of the anodes that suffered electrical breakdown, and hence has lost much more carbon than an anode would under normal operation over the same time interval, such as anode 1 of SSC 1. The left panels therefore show the effects of carbon loss more clearly than the right panels, but the right panels are more representative of normal ASM operation.

3.3.2 Multiple Time-Series Data

The EDS also records all the events in each SSC into multiple time-series (MTS) data streams. Events that register on exactly one resistive anode are recorded in three good events rates per SSC, one for each of the three canonical ASM energy bands (1.5–3, 3–5, and 5–12 keV), in 1/8th second time bins. Events that trigger on multiple anodes, or in both a position-sensing and an anti-coincidence anode, or yield a total response outside the discriminator threshholds for the good events energy range, are recorded in seven background rate channels in 1-s time bins. These background events are excluded from the position histogram data discussed above.

For a given source, the fit to the position histogram data results in the measurement of an average intensity during a given observation. It is sometimes possible to recover the light curve of a source on shorter time-scales from the MTS data even though no location information is preserved in this mode. The light curve for a given source can only be reliably recovered if all other sources in the FOV contribute a constant count rate in each time bin.

The total number of counts detected from a given source must be the same in both the position histogram and time-series modes. The results of the position histogram fit for a given source are the averaged count rates in three energy channels, normalized to give the expected count rate from the source if it were at the center of the FOV of SSC 1 (as described in Section 3.3.1). To recover the actual, "raw", number of counts detected from the source, one must multiply this number by the exposure time and the transmission factor (f) and divide by the normalization factor (a).

The sum of the raw count rates thus derived, carried out over all the sources in the FOV, should match the total count rate recorded in the corresponding MTS data. However, the MTS data also include counts that register at the extreme ends of each anode. The outermost position bins at either end of an anode are subject to random and sometimes dramatic electronic noise enhancements. The counts in these bins are not included in the fitting program described in section 3.3.1. The total

number of counts measured in the MTS data from a given observation will therefore be systematically larger than the number of counts one derives from summing the contributions from all the sources in the FOV as derived from the fits to the position histogram data. One must therefore set the background level in the MTS data by subtracting the known count rate of the source of interest, as determined from the fit to the position histogram data.

If no sources besides the source of interest are variable during a given observation, the number of counts from the source of interest recorded in a given time bin can be estimated as:

$$c_j = n_j - s\left(\frac{N}{e} - \frac{R \times f}{a}\right), \tag{3.1}$$

where N is the total number of counts detected in a given SSC energy band during an observation, e is the exposure time, R is the source intensity in c/s derived from the fit to the position-histogram data, f is the transmission factor, a is the normalization factor, s is the time bin size in seconds, and n_j is the number of counts in the jth time bin.

This method of background subtraction yields the number of counts detected from the source in a given energy channel and time bin. To express this as a normalized intrinsic intensity, one divides by s and multiplies by a/f, as is routinely done with the results from the position-histogram fits (Section 3.3.1). To then express the source's flux in Crab units, one divides the source's normalized intensity by the canonical count rate for the Crab in the appropriate energy channel (C_r, as given in Table 3-1):

$$r_j = \left[\frac{n_j}{s} - \left(\frac{N}{e} - \frac{R \times f}{a}\right)\right] \times \frac{a}{f} \times \frac{1}{C_r}. \tag{3.2}$$

3.3.3 Pulse Height Data

Whereas the relative amount of current recorded at each end of a resistive anode indicates the position of the incident photon, the total amount of current measured

at both ends of the anode is roughly proportional to the energy of the incident photon. The amount of current at the end of an anode is recorded as a integer between 0 and 4095, so the total current can produce a pulse-height response up to 8190. The ASM preserves spectral information about the incident photons primarily by recording the position histogram and time-series data in three energy channels, which are defined by the pulse-height bins 410, 1188, 1860 and 4750 (The nominal corresponding energies are given in Table 3-1.). However, there is a third data mode that preserves histograms of the pulse-height data in 64 bins over 64-s accumulations for each anode in each SSC. The primary use of the pulse height data mode is to monitor the gain of the instrument, which informs us of detector health and allows us to calibrate the actual energy boundaries of the three energy channels of the other two modes.

Each SSC collimator has a small amount of radioactive ^{55}Fe implanted in its wall. This source emits approximately one count per second from its K-shell line at 5.9 keV. We measure the gain of each detector by determining the location of this line in the pulse-height data. The actual gain is a multiplicative factor set around 10,000–15,000, but to measure this number we would need to know the number of electrons deposited on the anode. We do not know the number of deposited electrons, but since the detector response is roughly proportional to the energy of the incident photon, we can assume that the number of electrons deposited on the anode will be roughly the same for each photon from the ^{55}Fe source. We can therefore directly calibrate the detector response vs. photon energy.

Band	Range (keV)	Rate (C_r) (c/s)
Sum	$1.5-12$	75.5
A	$1.5-3$	26.8
B	$3-5$	23.3
C	$5-12$	25.4

Table 3-1: Normalized ASM Count Rates for the Crab Nebula

To ensure the isolation of this line with a strong signal to noise ratio, we select only those 64-s histograms that contain between 40 and 150 counts. These observations are typically instances when the camera points directly at the dark Earth. We expect about 64 counts in each histogram to originate from the ^{55}Fe source, but even if the camera is completely occulted by the Earth, there are always non-X-ray background events that will contribute to the histogram. Since those events will be spread out over the 64 bins, though, an upper limit of 150 counts ensures a balance between swamping the ^{55}Fe peak and rejecting so much data that the signal is not strong enough to find. If a 64-s interval yields fewer than 40 counts, the camera most likely was turned off early in the interval, and will likely only contribute to the noise.

We began with weekly sums of the acceptable histograms, but switched to monthly accumulations after the first year, to increase the signal strength. An example of one week's accumulation (from 27 Feb 1998 - 5 Mar 1998), SSC 1, anode 4 is shown in Figure 3-9. Panel (a) shows the sum of all the histograms that pass the abovementioned filter, while panel (b) shows the ^{55}Fe peak after a background model has been subtracted.

If the best-fit center of the ^{55}Fe peak is the bin value B_{55}, the relation between the bin B_x of a given X-ray and its actual energy E_x is taken to be $E_x = 5.9 \text{ keV} \times B_x/B_{55}$. This relation also yields the energies of the channel boundaries. The pulse-height data are binned by the EDS on board the spacecraft from the original 8190 energy channel bins into 64 bins. The location of the peak center in the pulse-height data (e.g., 20.0 as in Figure 3-9) must be multiplied by 128 to make it consistent with the units of the channel boundaries.

Figure 3-10 shows the location of the ^{55}Fe peak in a single anode for each SSC as a function of time. The energy channel boundary values for each SSC during this time period as derived from the mean gain values over all functional anodes are presented in Table 3-2. Note that although the lower boundary of Channel A is 1.0 keV, the effective area of the detector drops sharply below 1.5 keV due to absorption in the

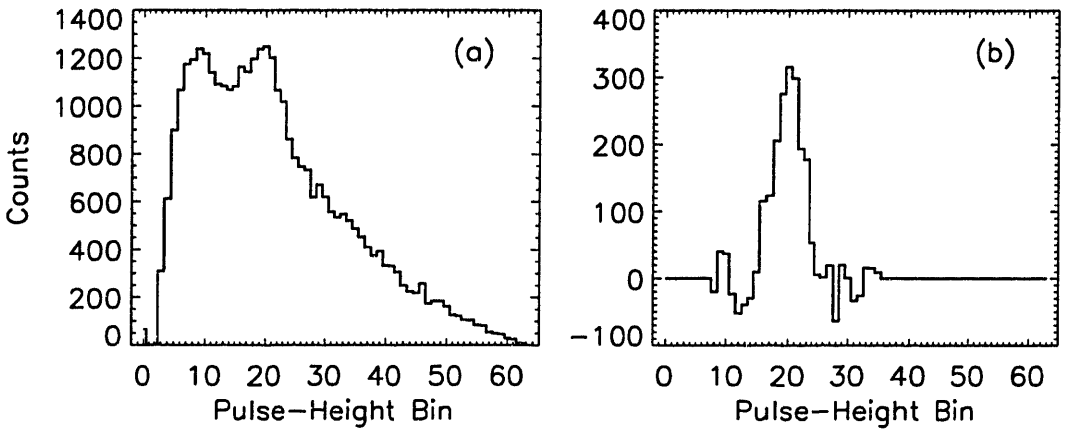

Figure 3-9 (a) The result of summing all pulse-height histograms (SSC 1, Anode 4) from mission week 109 that contain more than 40 and less than 150 counts. The ^{55}Fe emission line is clearly visible at bin 20 above the soft background. A second-order polynomial is fit to the background on either side of the ^{55}Fe peak (e.g. bins 8-12 and 24-35) and subtracted from the histogram shown in panel (a). Bins below 8 and above 35 are set to zero. The resulting histogram is shown in panel (b). The Gaussian center of the peak is found to be at 20.0 bins.

Be window.

Although the gain remains roughly constant in SSC's 2 and 3, the gain of SSC 1 has been consistently rising over the course of the mission. This behavior in SSC 1 is expected, as we knew before launch that SSC 1 had a small leak, and the gain of a PSPC depends inversely on the gas pressure of the chamber. Prior to launch, I tested the flight detectors for possible leaks. With the equipment and assistence of colleagues in atomic physics research (Prof. Daniel Kleppner's Precision Measurement Lab in particular), I placed each detector in a vacuum chamber, pumped the chamber down to a pressure of 7×10^{-7} torr, and used a mass spectrometer to measure the presence of xenon in the vacuum chamber. The leak of xenon from the flight unit for SSC 1 was clearly detectable, but the measured leak rate of $(1.1 \pm 0.1) \times 10^{-8}$ atm cc s^{-1} was below our estimated tolerance of 6×10^{-7} atm cc s^{-1}, which would result in a 1% per month increase in the detector gain. Figure 3-10 shows a roughly 0.6% per month increase in detector gain for anode 1 for the first 1.5 y of the mission, after which the

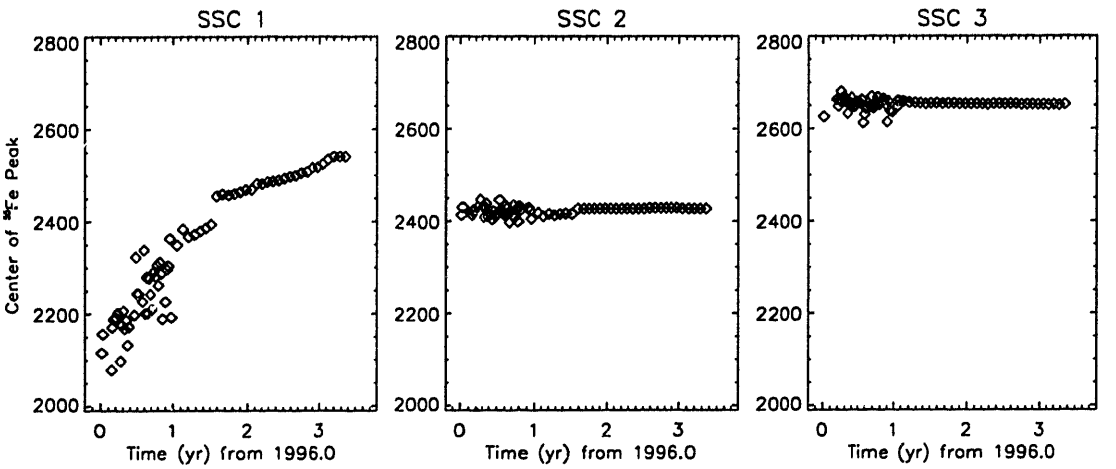

Figure 3-10 The position of the center of the ^{55}Fe peak on a scale of 0 to 8190 for anode 1 of each SSC. The first year is presented in weekly accumulations. After 1997.0, each point represents one month's data. Due to a small leak in SSC 1, the gain is increasing in that detector, while the other cameras remain stable.

rate of increase drops to 0.2% per month (other anodes behave similarly). Eventually, this leak will render the detector inoperable. Although we cannot be certain of the exact time when this will happen, laboratory testing indicates that it should be at least a few years from now.

SSC	Mean Gain	A Channel (keV)	B Channel (keV)	C Channel (keV)
1	2365	1.04–3.0	3.0–4.6	4.6–11.8
2	2324	1.02–3.0	3.0–4.7	4.7–12.1
3	2546	0.95–2.8	2.8–4.3	4.3–11.0

Table 3-2: Mean Energy Channel Boundaries

Chapter 4

Determination of Error Box Sizes

4.1 A Measurement of Error

For a GRB source position, it is essential to report an accurate error box with a reliable confidence level, i.e., a good estimate of the probability that the source is within the box. In this section, we describe our method of determining the association between error box size and confidence level. The method is empirical and relies on observations of persistent X-ray sources. If a source is removed from the catalog of known sources used in the initial fit, it functions as a new source to be detected and localized with our standard software. The derived location may then be compared with the known precise location of that source's optical counterpart.

This procedure was performed on 13,982 observations of six X-ray sources, chosen to provide a wide range of intensities (Table 4-1). These six sources are also relatively isolated on the sky, ensuring that emission from nearby sources will not introduce errors into the localization process. The GRBs detected by the ASM are also isolated sources, but should a new source appear near a familiar source, the results presented in this chapter may not be applicable. We chose the test observations from five 50-d time intervals when these six sources were observed most often.

The best-fit position from each observation of a test source was compared with

the catalogued source position, and the displacement was recorded in the field of view (FOV) coordinates, ϕ and θ (Fig. 3-4). We further assumed that the error can be effectively treated as a function solely of the total number of photons detected from the source. The distribution of the resulting position errors provides the basis for the association between confidence levels and error box sizes.

4.2 Error Distributions

There are four main characteristics of an observation that can affect the accuracy of attempts to localize a source: the source's intrinsic brightness, the source's FOV location, the contribution to the background from other sources in the FOV, and the number of diffuse background counts. One advantage to the coded-mask imaging technique is that the background strength to which the signal strength should be compared is not the total number of non-signal counts in the entire detector, but rather the number of non-signal counts detected in that portion of the detector which is illuminated by the (off-axis) source of interest.

The dominant contribution to the total background is usually from diffuse celestial X-ray emission. Roughly 2500 counts are typically detected from the diffuse X-ray background per 90-s observation. A relatively small number of counts, ~150–450, are contributed from non-X-ray background. Occasionally, substantial fluxes of solar X-rays scattered in the Earth's atmosphere or the inside surface of the one of the collimators are detected. This solar X-ray contamination can contribute up to $\sim$ 1600 counts to the total background. For the ~14,000 observations used in this analysis, the median number of counts in a single SSC per dwell (excluding the counts from the test source) is $\sim$ 3150 (1.5–12 keV). Only $\sim$ 20% of the observations had a total background higher than 5000 counts, and only $\sim$ 5% of the observations had more than 9750 background counts. Half of the observations show a total background between 2000 and 4000 counts, indicating that there were no other strong discrete

Source Name	R.A. (J2000)	Decl. (J2000)	Intensity (mCrab)[1]	No. in SSC 1[2]	No. in SSC 2[2]	No. in SSC 3[2]
Sco X-1	16h 19m 55.13s	−15°38′24.4″	9000-23000	755	816	1153
Crab	05h 34m 31.97s	+22°00′52.2″	930-1100[3]	598	546	1644
Cyg X-2	21h 44m 40.97s	+38°19′18.1″	200-900	1148	1151	353
Cyg X-3	20h 32m 25.54s	+40°57′27.7″	70-600	1378	1368	400
Her X-1	16h 57m 49.73s	+35°20′32.3″	< 200	222	218	44
4U 0614+091	06h 17m 7.32s	+09°08′13.6″	< 200	416	293	300

Table 4-1: Calibration Sources

sources in the FOV besides the test source.

Observations that have more than about 4000 total background counts most often have other point X-ray sources in the FOV. These other sources can increase the statistical noise in an observation, as well as the likelihood for systematic errors in a derived position. However, the effect of a widely separated source on the derived position for the test source tends to be small, since the overlap between the shadow patterns of such sources on the detector surface is generally small. To minimize the effect of other sources on our results, the six test sources were selected in part because they are relatively isolated on the sky. Only two of these six sources are within 15° of another X-ray source bright enough to be detected by the ASM. The smallest separation is the ~ 9° separation of Cyg X-3 from Cyg X-1. In the case of Sco X-1, nearby Galactic plane sources contribute significantly to the total background, and indeed, Sco X-1 is the test source in 73% of the 1271 observations that have more than 8000 total background counts. However, Sco X-1 is so bright (an on-axis, 90-s observation typically yields more than 68,000 counts) that contamination by these sources is not expected to have any significant effect on the localization accuracy. We therefore did not expect, *a priori*, that the presence of other sources in the FOV

[1]Intensity in mCrab derived from detected count rates, adjusted to simulate observations with the source at the center of the FOV of SSC 1, and normalized to a nominal count rate of 75 c/s for the Crab Nebula at the center of the FOV of SSC 1.

[2]The number of observations of each source used to analyze the position error.

[3]Including statistical and systematic errors in ASM detections.

would often have a large effect upon the local statistical noise at the positions of the test sources.

If the counts from other sources are not properly modeled and subtracted via the initial fit, the noise level near the test source may be enhanced by systematic "ripples" in the cross-correlation map, even if the sources are well-separated in the FOV. To minimize these ripples, the calibrated relations between electrical position and physical location at a time near the middle of each 50-d interval were used in the generation of the model shadow patterns used to fit observations taken during that interval. The use of *a posterori* calibration ensures that the detector response will be modeled as accurately as possible, which means not only that the test sources will be localized as accurately as possible, but that other discrete X-ray sources will have a minimal effect on systematic noise near the source of interest. For real-time operations, we generate model shadow patterns based on an extrapolation of the two most recent calibration measurements. Over months, the true calibration will drift from this set of extrapolated values, degrading the localization accuracy and increasing the systematic noise. We therefore update the calibration periodically, but there may be times when the localization accuracy in real-time operations will not achieve the level presented here.

We parameterize the position error as a function of the total number of counts observed from a source during a single observation. The collimator reduces the area of the detector exposed to an off-axis source, so that sources of the same intrinsic brightness will yield different numbers of counts if they are observed at different locations in the FOV. For example, a $\sim$ 300 mCrab source at the center of the FOV will generate $\sim$ 2000 counts in a 90-s observation, while the same source at $\phi = \pm 4.0°$ will only contribute $\sim$ 700 counts. The FOV position of the relevant test source is effectively random. Thus, the 14,000 test observations yield numbers of source counts that span the entire range expected from a single source during a 90-s ASM dwell.

For this analysis, we assume that an off-axis bright source and an on-axis dim

source that both yield the same number of counts in an observation can be localized with approximately the same accuracy. The off-axis source illuminates the detector through fewer mask slits, yielding fewer shadow edges in the position histograms that can be used to localize the source in the cross-correlation process. However, each slit edge will be defined by a greater count rate contrast, and the effective number of background counts will be reduced in proportion to the reduction in the exposed area of the detector. If the localization accuracy were to scale like the detection sensitivity, we would expect it to be approximately inversely proportional to the square root of the exposed fraction of the detector surface, if the numbers of source and background counts are held constant. Therefore, over a restricted region of the FOV, any error in estimating error box sizes using the number of source counts rather than a more sophisticated estimator is expected to be limited. For sources near the edge of the FOV, this approximation is poor and calibration errors have a particularly large effect, so we only consider observations where the test source was located such that $\mid \phi \mid < 4.6°$ and $\mid \theta \mid < 45°$.

We therefore proceed as follows: for each of the $\sim 14,000$ observations we record both the total number of photons detected from the test source and the deviation of the derived position in ϕ and θ from the true position. We separate the location measurements according to the number of detected source counts into seven groups per SSC and bin the angular errors for all observations in each group into histograms. Figure 4-1 shows the resulting distributions for SSC 1. Each histogram shows the distribution of errors in ϕ (left panels) and θ (right panels) between the derived source position and the actual celestial position for detections of sources with measured source counts within a certain range. The number of counts increases vertically in the figure. Note that the abscissa scale is not the same in each panel.

We performed two sanity checks to ensure that our assumptions were consistent with the resulting distributions. We first checked whether the effects of the test sources' FOV locations are adequately approximated by our assumption that the

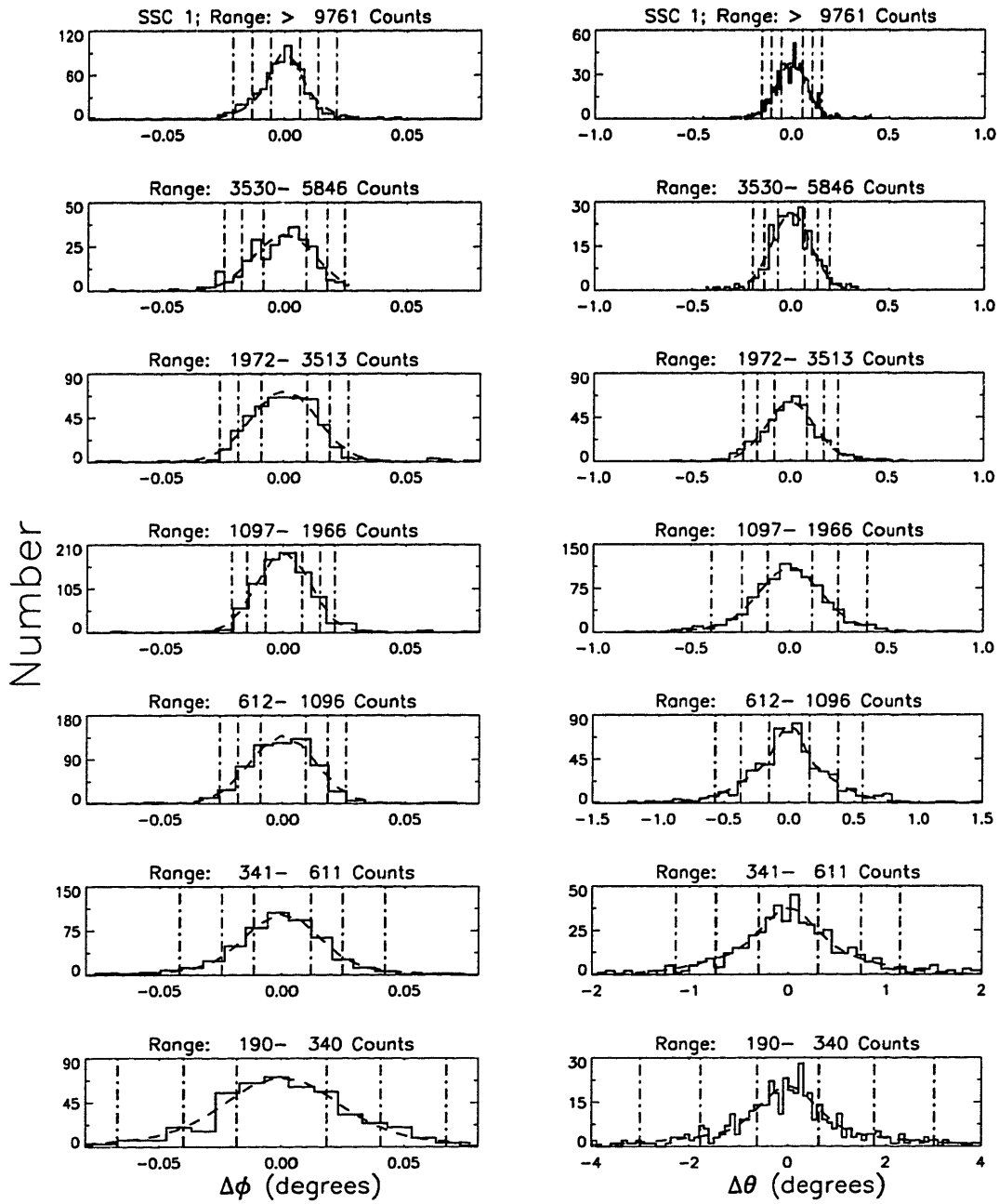

Figure 4-1 A demonstration of the position-determining ability of SSC 1 and the validity of the model used to calculate confidence limits. See text for a detailed description.

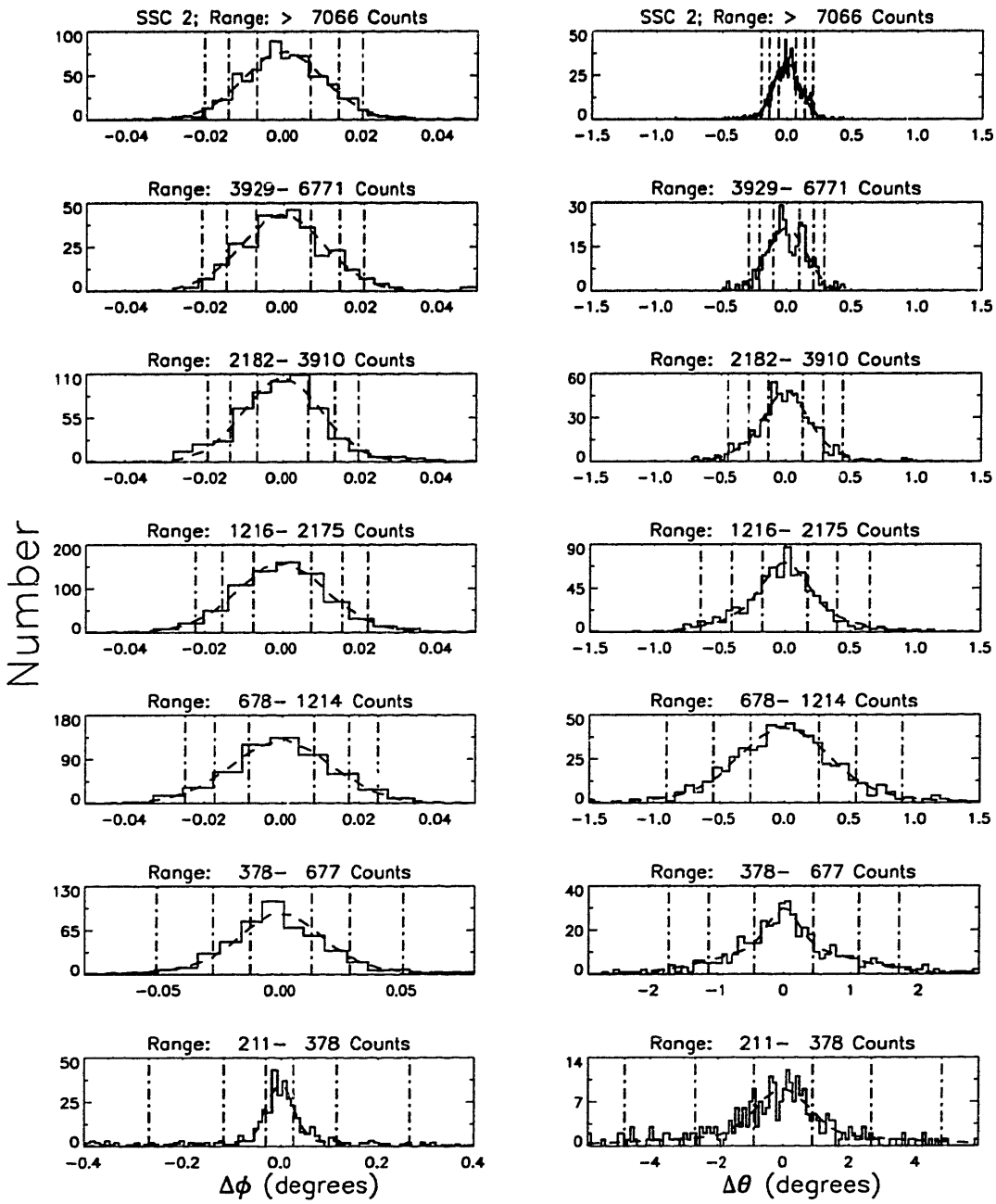

Figure 4-2 A demonstration of the position-determining ability of SSC 2 and the validity of the model used to calculate confidence limits.

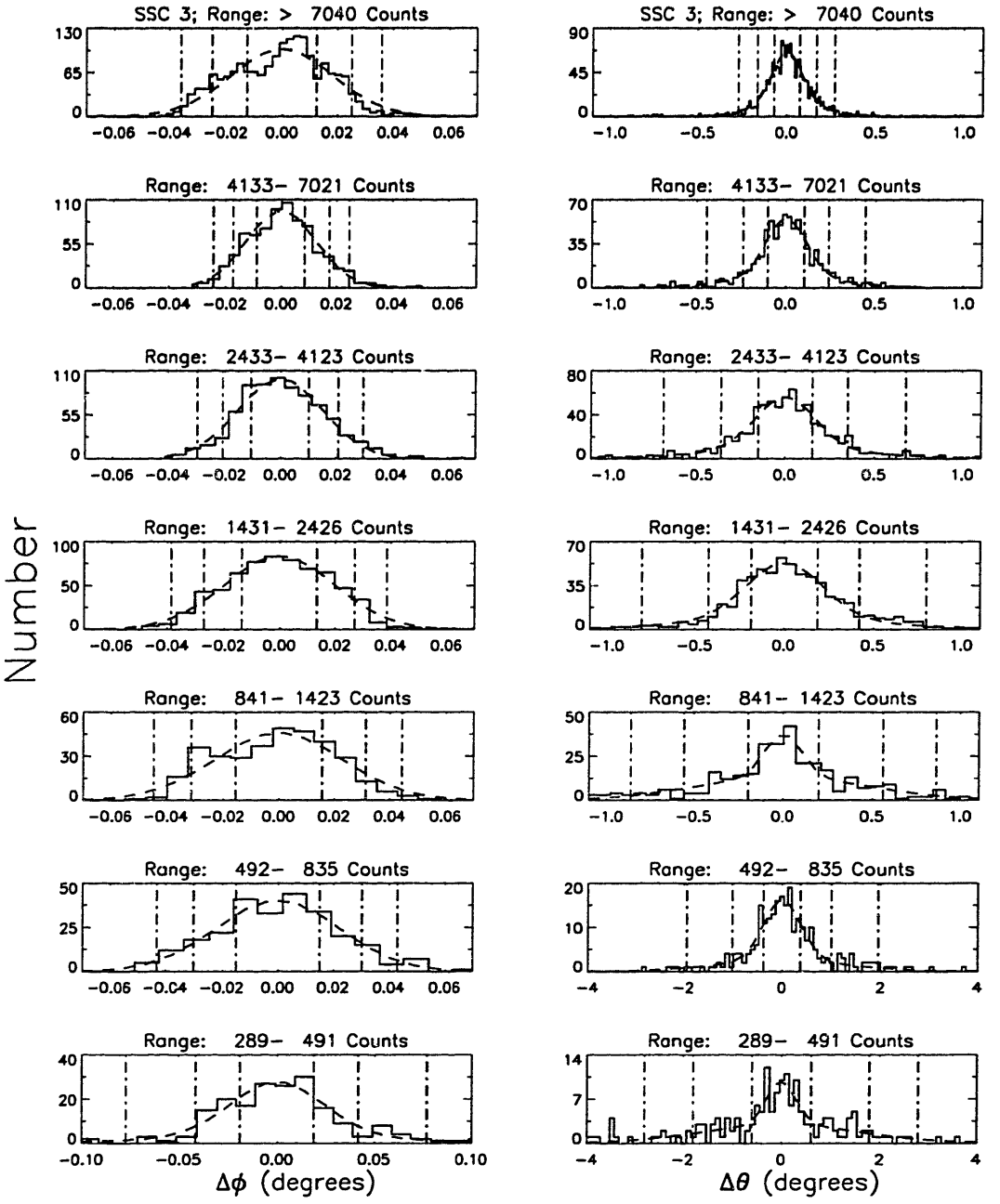

Figure 4-3 A demonstration of the position-determining ability of SSC 3 and the validity of the model used to calculate confidence limits.

localization accuracy depends only on the number of source counts. To do this, we separated the $\sim 14,000$ observations into two groups according to the ϕ coordinate of the test source's actual location, i.e., the two groups were defined by $\mid \phi \mid < 2.0°$ and $2.0° \leq \mid \phi \mid \leq 4.6°$. We binned the deviations between the actual and derived source locations according to number of source counts and FOV group and obtained two sets of error histograms. The widths of the resulting error distributions for either the θ or ϕ coordinate did not show any clear systematic dependence on FOV group.

The effect of the background level on the accuracy of our localizations was similarly checked by dividing the set of observations into groups based on the total background, i.e., all counts excluding those from the test source. We again calculated position error distributions based on test source counts for each of these groups. The error distributions for the high background cases (> 4000 counts) were found to be indistinguishable within statistical limits from the distributions for the low background cases (< 4000 counts). The cases in which the number of total background counts rose above 8000 were also examined. As noted, 73% of these observations used Sco X-1 as the test source. No significant difference between the error distributions from these observations with high total background and those of low total background was found. These results indicate that sources widely separated from the test source have only small effects on the localization of the test source. A new source that appears close to a strong source will not be localized as accurately as indicated by the present results, but we have not tried to quantify the effects of other nearby sources.

4.3 A Model for the Error Boxes

We modeled each histogram of coordinate errors as the sum of a narrow Gaussian, a wide Gaussian, and a constant. For bright sources, a single narrow Gaussian is sufficient to obtain a reasonable fit. For small values of source counts, there is a significant chance that noise in the cross-correlation map will result in an incorrect

identification of the source location. The noise may raise a side lobe of the instrument response to a value higher than the peak at the source location. This yields broad wings on the side of the central peak in the error histograms. These wings are modeled by the wide Gaussian. Noise peaks may even exceed the value of any response to the test source, which results in a population of measured errors that are distributed uniformly across the whole range of allowed values for each angle. This uniform scatter is present but not obvious in Figures 4-1 through 4-3, because only the region near the central peak is displayed. At extremely low source counts, the central Gaussian peak disappears entirely, leaving only the random scatter. There is no evidence for a central peak below ~ 200 counts in SSCs 1 and 2 and below ~ 300 counts in SSC 3.

Our strategy in reporting error boxes is to define uncertainties in each FOV coordinate appropriate to a given confidence level under the assumption that the detection was of a real source. In addition, we quote the probability that the detection was spurious. The estimated probabilities are derived by integrating under the components of the best-fit model distribution. A confidence interval at $x\%$ is defined as the symmetric interval about zero such that the integral of the two Gaussian curves over that interval yields $x\%$ of the integral of the same Gaussians over the entire range of possible errors. Figures 4-1 through 4-3 display as vertical broken lines the values in both the ϕ and θ directions that correspond to 50%, 82% and 95% confidence limits.

The uncertainty in each coordinate associated with each of the selected confidence limits is plotted as a function of the number of detected source counts in the left panels of Figures 4-4 through 4-6. We used these results to derive interpolation functions which give FOV coordinate uncertainties for the source location at three significance levels for any number of source counts (x). We chose as an interpolation function, $I(x)$, the sum of two power laws and a constant:

$$I(x) = Ax^{-\alpha} + Bx^{-\beta} + C. \tag{4.1}$$

The constant C represents the limiting systematic error (with values, for example, of $\sim 1.5'$ in ϕ and $12'$ in θ for SSC 1 at 95% confidence), and the power laws are simply a convenient means to interpolate between the measured angular uncertainties. The best-fit interpolation functions are graphed as broken lines in the left panels of Figures 4-4 through 4-6.

The difference between the total number of measurements in the histogram and the area under the two model Gaussian curves is a measurement of the probability of mistaking a noise peak for the source. This difference is plotted in the right panels of Figures 4-4 through 4-6. The error bars reflect the counting statistics of the total number of actual measurements in each histogram, and are typically 3–7%. These figures show that the probability of misidentifying a source increases as the number of detected photons decreases. To interpolate between these points, we use the formula:

$$f(x) = \frac{1.0}{1 + e^{-b/(x-a)}} \tag{4.2}$$

where x is the number of detected source counts, and a and b are constant parameters determined by a least-squares fitting procedure. This function was selected because it could match the rising behavior of the data at low numbers of counts, while also ensuring that the probability never exceeded one or dropped below zero. The best-fit functions are plotted as broken lines in the right panels of Figures 4-4 through 4-6. Note that extrapolation of this function below the 200–300 count limit mentioned above is not meaningful.

It is our practice to define error box sizes based on the double-Gaussian integration limits (left panels; Figs. 4-4 through 4-6) and to separately specify the probability that the detection is spurious (right panels; Figs. 4-4 through 4-6). The former yield a probability p (= 0.95, 0.82 or 0.50) that the actual GRB location lies within the associated interval. There is a probability of p^2 that the actual GRB location lies within two of these intervals. A box on the sky, defined by 95% limits in each of two

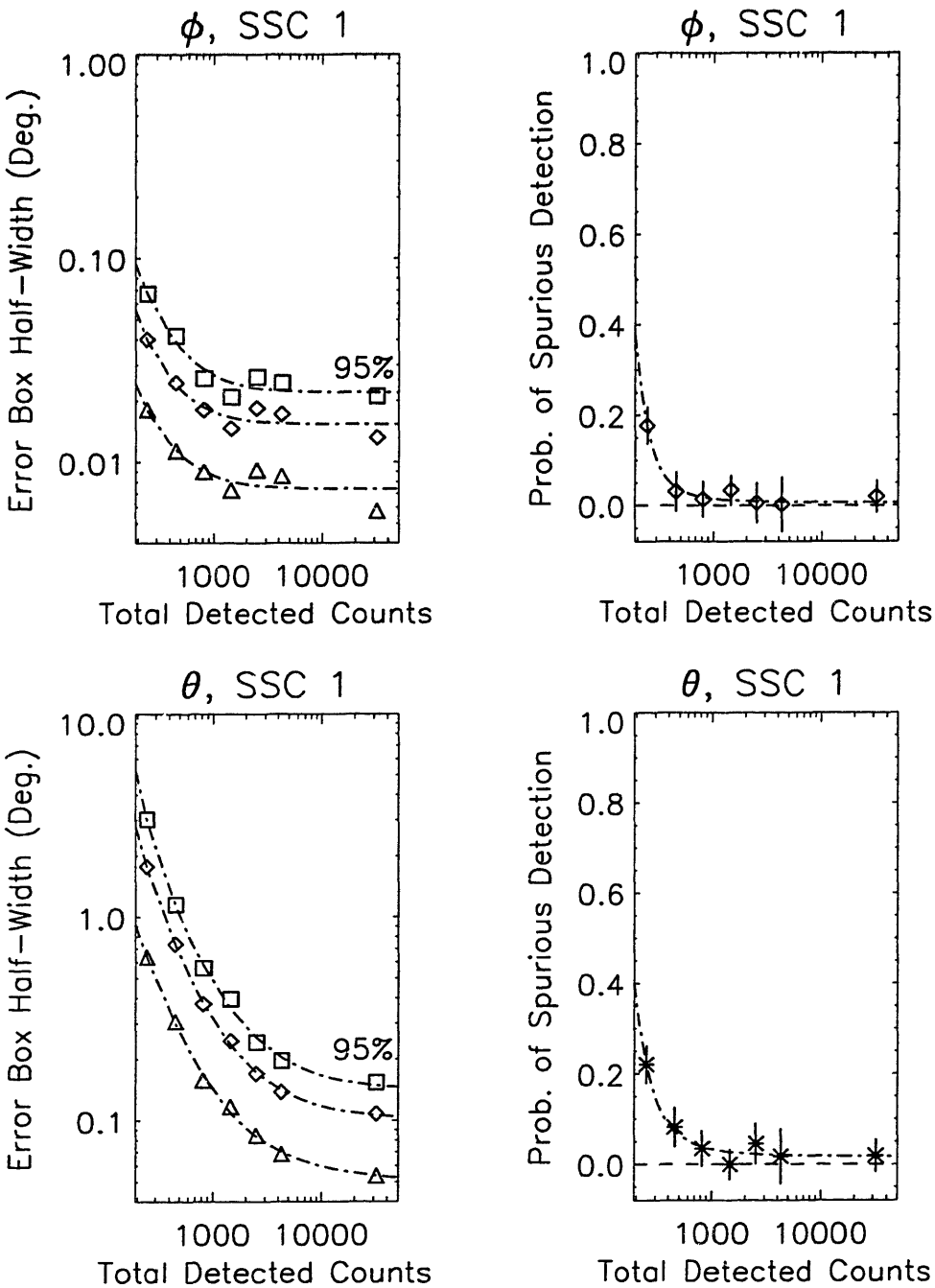

Figure 4-4 The functions used to set the size of the ASM error box for a new X-ray source observed by SSC 1. The left panels display the half-widths of error boxes in each of two dimensions at three levels of confidence (95%, 82%, and 50%), as modeled by the two-Gaussian model for the histograms shown in Figure 4-1. The right panels display the fraction of the measurements unaccounted for by that model; i.e. the fractional area under the constant component to the model. All graphs use the total measured counts from the source as the abscissa.

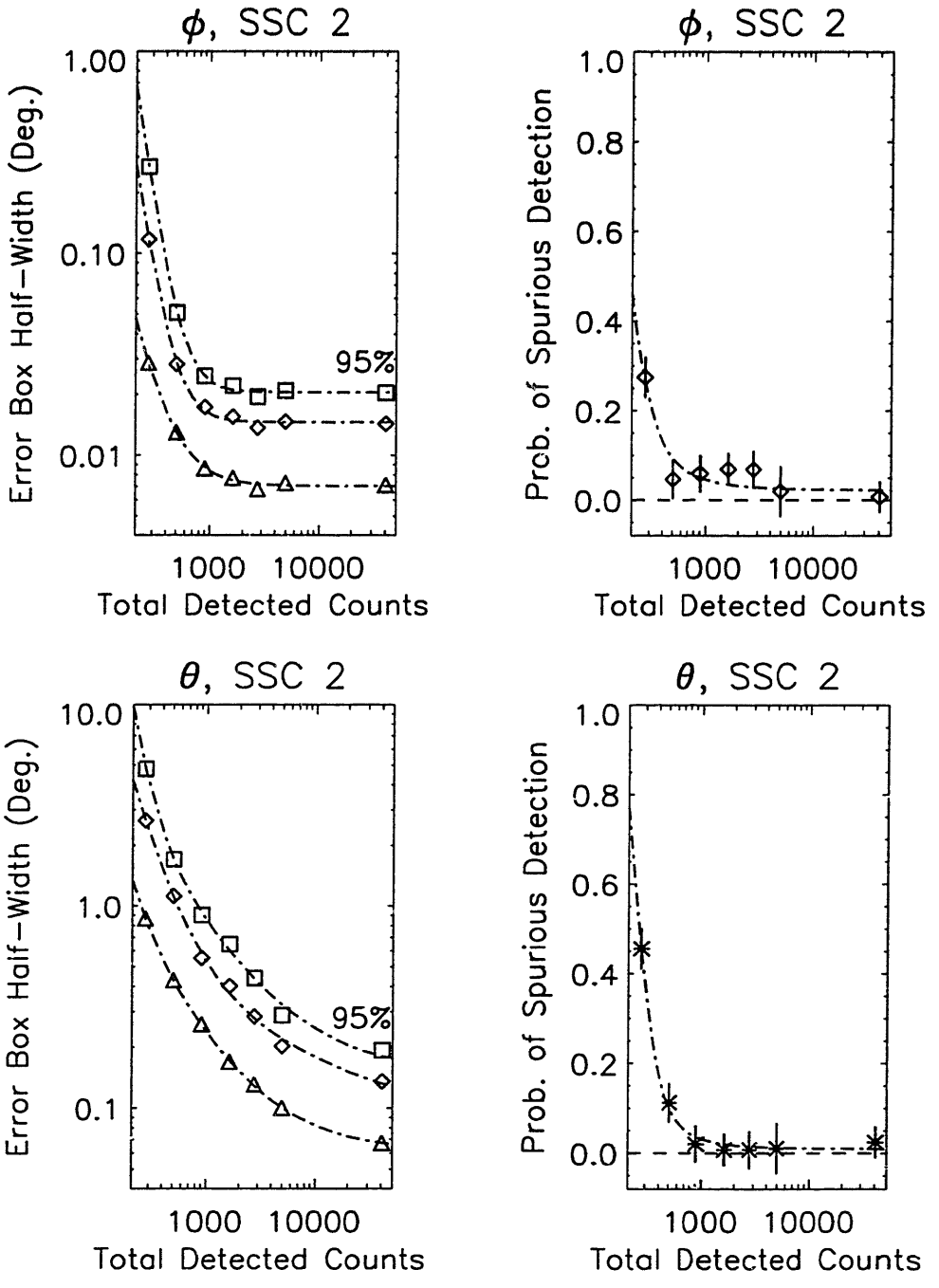

Figure 4-5 The functions used to set the size of the ASM error box for a new X-ray source observed by SSC 2. See caption for Figure 4-4.

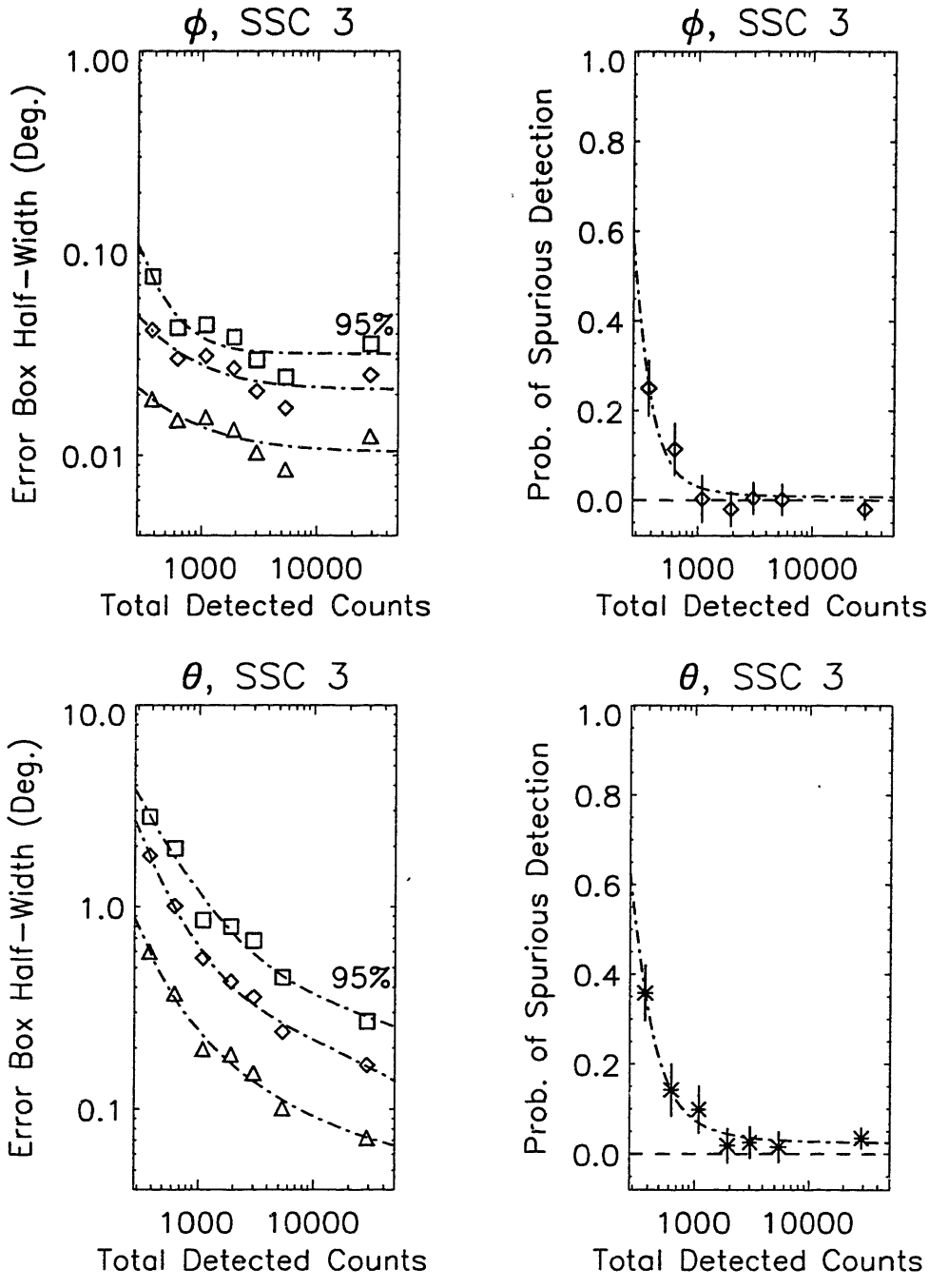

Figure 4-6 The functions used to set the size of the ASM error box for a new X-ray source observed by SSC 3. See caption for Figure 4-4.

directions, is therefore a 90% confidence region. In the case of a single-SSC detection, the two intervals will be in terms of ϕ and θ in that SSC, but if detections of a given source are available in two SSCs, the diamond formed by the intersection of the two ϕ intervals can be taken as the 90% region (e.g. Figure 5-3). Similarly, using the 82% values in each direction will yield an error box at 68% confidence, and the 50% values will yield a joint error box at 25% confidence. In cases of weak source detections, this smallest box helps illustrate the deviations of the actual error distributions from simple Gaussians.

We have thus derived functions to estimate source position uncertainties corresponding to the 95%, 82%, and 50% confidence limits in each of two dimensions, valid for detections of more than 200–300 counts under the assumption that the corresponding peak in the cross-correlation map represents a valid source detection. We find that the width of the error distribution can be effectively parameterized as a function of the total number of counts detected from a source. This analysis is valid for the central region of the FOV, when the sky around the new source is free of contaminating sources, and an accurate calibration of the electrical-physical position correspondence in the detector is available. Under these conditions (which may not hold for all real-time detections), this analysis provides a rational means for associating error-box sizes with confidence levels.

Chapter 5

Thirteen GRB Localizations

In this chapter, I report the positions of thirteen Gamma-Ray Bursts (GRBs) localized with the ASM in its first three years of operation. It is impossible to unambiguously distinguish a GRB from an X-ray burst on the basis of ASM data alone. We therefore report the positions of thirteen events which have been identified as GRBs through the comparison of ASM timing and location information with data from other operational GRB detectors including BATSE on the *Compton Gamma Ray Observatory*, the Gamma-Ray Burst Instrument on *Ulysses*, KONUS on the *Wind* spacecraft, and the Gamma-Ray Burst Monitor on *BeppoSAX* (See Table 5-1). These instruments, as well as the Interplanetary Network (IPN) triangulation technique, are described elsewhere (See, e.g. [30, 70, 67] and Section 2.1).

Pertinent data on these thirteen bursts are given in Tables 5-1–5-5. Table 5-1 gives the onset times, 1.5–12 keV fluences, and centers of the ASM error boxes, Table 5-2 gives the error box sizes and position angles for the single-SSC detections, and Table 5-3 gives the celestial coordinates of the corners of the best intersection diamonds in cases of two-SSC detections. Table 5-4 reports the circular localizations achieved with other high-energy instruments, while Table 5-5 describes the available IPN annuli.

5.1 Archival Searches for GRBs

5.1.1 A Comparison With BATSE Positions

The GRBs described here were discovered through the use of four different techniques. First, we searched the ASM data at the approximate times and rough locations (the radii of the error circles were not available at the time of our search) of 438 GRBs determined from BATSE data between 1996 Jan 6 and 1997 Jul 15 (see, e.g., [103] for times and locations). If the trigger time of a burst corresponded to a time when the ASM was collecting data, and if the BATSE localization was within the ASM FOV at that time, the relevant ASM observation was searched for evidence of a GRB detection. This search resulted in the discovery of X-ray counterparts for GRB 960416 (Figure 5-1a) and GRB 961019 (Figure 5-2a). The former event was detected by two SSCs simultaneously, while the latter was only detected by SSC 2. Both events were also detected by the *Ulysses* GRB instrument, so IPN annuli could be calculated. Both annuli were consistent with the ASM positions, and in the case of GRB 961019, the IPN annulus reduced the length of the error box to 11′.

5.1.2 A Search in the ASM Time-Series Data

Second, we searched through the ASM time-series data up to September 1997 for episodes of transient emission that could be from GRBs not detected by BATSE. We performed linear least-squares fits to the count rates for each 90-s dwell of the ASM. This search was largely conducted by Linqing Wen. Steady or very slowly-changing count rates (on time-scales between 1/8 and 90 s) yielded low values of χ^2. We then examined the observations yielding the highest values of χ^2 for GRB-like events. We excluded cases where a bright, persistent source moved in or out of Earth occultation or a known highly variable source like GRS 1915+105 was in the FOV. We searched the position data from the remaining dwells for indications of new sources. Observations containing a new source candidate with an intensity measurement of

Date of GRB (yymmdd)	Time of GRB (hh:mm:ss)	Confirming Satellite[1]	2-12 keV Fluence (10^{-7} ergs cm^{-2})	R.A. (J2000)	Decl. (J2000)
960416	04:09:00	ub	6.0 ± 0.3	04h15m27s	+77°10′
960529	05:34:34	k	$> 17.5 \pm 0.6$	02h21m50s	+83°24′
960727	11:57:36	uk	9.5 ± 0.5	03h36m36s	+27°26′
961002	20:53:55	uk	9.2 ± 0.5	05h34m46s	−16°44′
961019	21:08:11	ub	4.6 ± 0.6	22h49m00s	−80°08′
961029	19:05:10	k	$> 3.3 \pm 0.4$	06h29m27s	−41°32′
961230	02:04:52	u	1.5 ± 0.3	20h36m45s	−69°06′
970815	12:07:04	ubks	$> 33.3 \pm 0.8$	16h08m33s	+81°30′
970828	17:44:37	ub	$> 14.9 \pm 0.6$	18h08m23s	+59°19′
971024	11:33:32	b	1.1 ± 0.3	18h25m00s	+49°27′
971214	23:20:41	ubks	3.4 ± 0.3	12h04m56s	+64°43′
980703	04:22:45	ub	$> 18.3 \pm 0.8$	23h59m04s	+08°33′
981220	21:52:21	uks	12.6 ± 0.5	03h43m38m	+17°13′

Table 5-1: Properties of 13 ASM-detected GRBs

5σ significance or greater in addition to excess short-term variability in the time-series data were flagged as containing possible GRB candidates. This search yielded five additional events that could be confirmed as GRBs by *Ulysses* and/or KONUS detections. There were no other obvious GRB-like events that we could not identify as coming from previously known X-ray sources.

GRB candidate 960529 (Fig. 5-1b) was detected in two SSCs over two consecutive dwells, yielding four position determinations. The two smallest boxes are plotted in Figure 5-1b; the largest two are consistent with the intersection of these two. This event was detected by KONUS, but not by *Ulysses*, rendering an IPN annulus impossible to calculate. Both the ASM and KONUS observed three successive peaks, lasting a total of $\sim$ 200 s, but KONUS detected no emission above 50 keV (P. Butterworth, private communication). It is therefore possible that this event was not a GRB but was a series of hard flares from an unknown X-ray source.

GRB 960727 (Fig. 5-1c) and GRB 961002 (Fig. 5-1d) were bright events, but both

[1] u - *Ulysses*; b - BATSE; k - KONUS; s - *BeppoSAX*

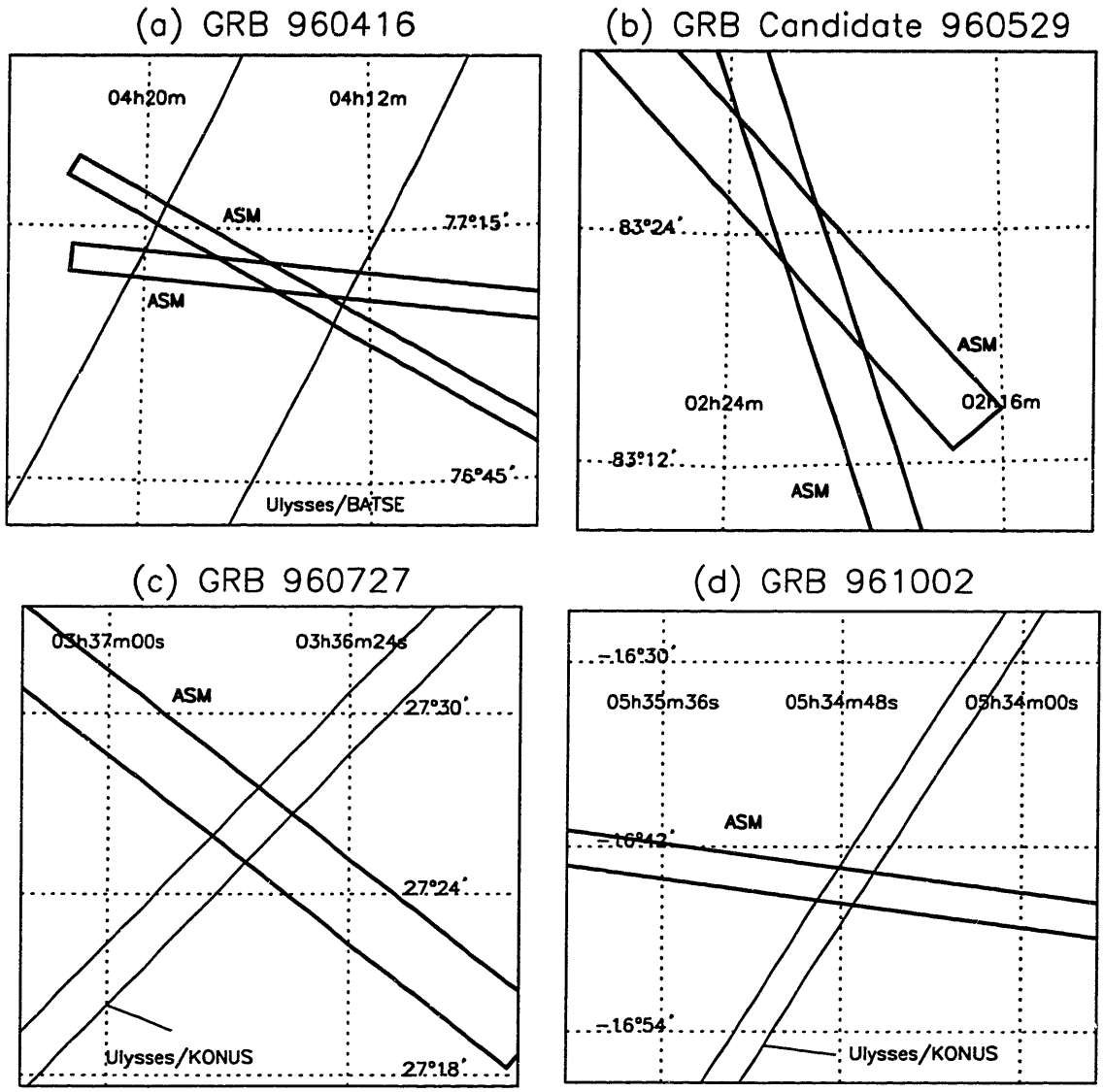

Figure 5-1 The ASM localizations of four GRBs, shown with position information from other satellites when available. Each frame is mapped at a different scale. ASM (dark lines) and BATSE locations are given at 90% confidence, while IPN annuli are 3 σ. Positions and sizes of the 90% regions are given in Tables 5-1–5-3, while references to the other instruments are given in the text and in Tables 5-4–5-5.

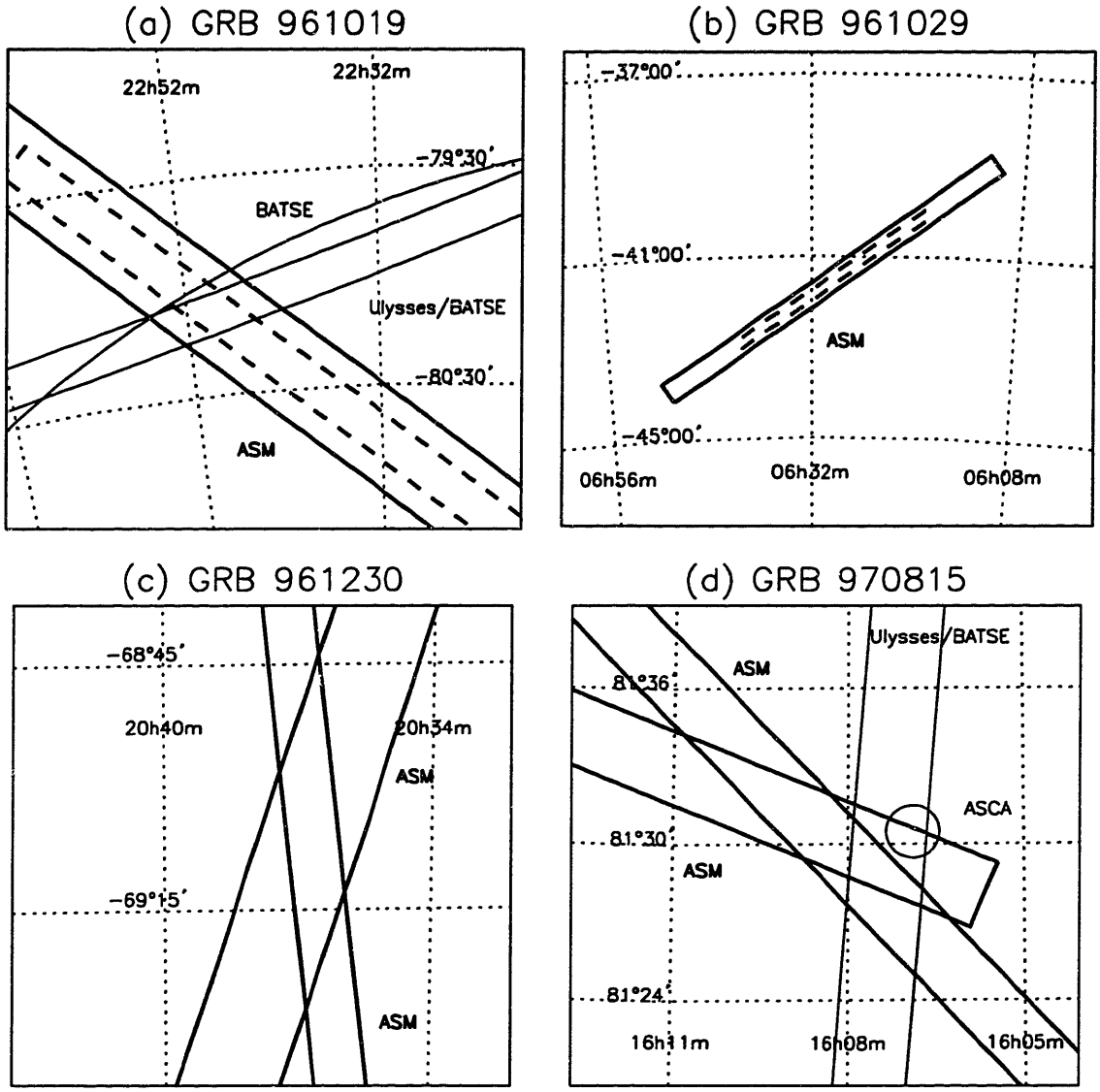

Figure 5-2 The ASM localizations of four GRBs, shown with position information from other satellites when available. For cases where the burst detections are very weak (Table 5-6), boxes at 68% confidence are also plotted as dashed outlines. See caption for Figure 5-1.

Date of GRB (yymmdd)	Length (arcmin.)	Width (arcmin.)	Position Ang.[1] (deg.)
960727	65.4	2.5	51.85
961002	76.3	2.6	82.19
961019	493.2	25.6	52.34
961029	522.5	28.0	-54.71
971024	249.5	6.5	64.38
971214	204.2	5.7	-62.54
981220	58.9	2.5	75.64

Table 5-2: Properties of Single-SSC ASM Error Boxes

were seen in only one ASM SSC. However, they were both detected by KONUS and *Ulysses*, so annuli could be calculated that reduced the lengths of the error boxes to 1.4′ and 2.1′, respectively. GRB 961029 (Fig. 5-2b) was seen as an abrupt rise in the last few seconds of a single-camera ASM observation, so despite reaching a peak flux of $\sim$ 3 Crab, the ASM measured only a total of 289 counts from this GRB. GRB 961230 (Fig. 5-2c) was also weak (see Table 5-6), but was detected in two cameras. Neither GRB 961029 nor GRB 961230 was detected by more than one IPN instrument, so triangulation annuli were impossible to calculate in these cases.

5.2 Real-Time Responses to GRBs

5.2.1 A Response to GCN Alerts

Third, as of May 1997, we began searching for GRB events in the real-time ASM data. We first developed software to respond directly to the GRB alerts released by the BATSE team over the Gamma-ray burst Coordinate Network (GCN). The ASM observing plan cannot be changed in response to alerts, but on occasion the ASM FOV will overlap with a BATSE GRB error circle at or shortly after the trigger time.

[1]Defined such that positive is east of north.

GRBs have been observed by BATSE to last hundreds of seconds, often with multiple peaks [102], and there is evidence that GRBs last longer at lower energies than at higher energies [25, 123]. Since the ASM rotates 6° every 90 s, a rotation may put the FOV of an SSC onto the position of a burst which is in progress.

The automated program compares the BATSE information for each new trigger with the planned observing schedule for the ASM, and alerts members of the ASM team if the ASM is scheduled to scan over the BATSE error circle within 1000 s from the time of trigger. This effort has led to the detection of five GRBs between June, 1997, and December, 1998, and the resulting ASM positions were distributed to the community within 2–12 h after the events, enabling rapid follow-up by other observers. The positions reported here represent refinements that supercede any GRB positions previously reported in IAU or GCN Circulars by the ASM team. However, unless stated explicitly below, these positions differ from the initial error boxes reported in the Circulars by no more than an arcminute.

GRB 970815 (Fig. 5-2d) had multiple peaks in its light curve, and it was located such that it was detected in a single SSC during a single 90-s dwell [144]. During the next dwell, it became much brighter while it was observed with both SSCs 1 and 2. As the event faded during a third dwell, the source location was less than a degree from the edge of the FOV of SSC 1 (and outside the FOV of SSC 2). This location is outside the region of the FOV considered in the present analysis, and a reliable position could therefore not be obtained from this dwell. As with GRB candidate 960529, only the two smallest error boxes are shown in Figure 5-2d. This GRB was also seen by both BATSE and *Ulysses*, and an IPN annulus confirms the ASM position. Three days after the GRB event, a weak X-ray source with constant intensity near the ASM position was seen by *ASCA* [113] (included in Fig. 5-2d); it is unlikely to be related to GRB 970815.

GRB 970828 (Fig. 5-3a) was localized in two SSCs, and its location was published within two hours of the onset of the event [129]. The PCA on *RXTE* slewed to observe

Date of GRB (yymmdd)	R.A. 1 Decl. 1 (J2000)	R.A. 2 Decl. 2 (J2000)	R.A. 3 Decl. 3 (J2000)	R.A. 4 Decl. 4 (J2000)
960416	04h15m32.8s	04h13m30.0s	04h15m21.9s	04h17m25.4s
	+77°11′17″	+77°07′20″	+77°08′00″	+77°11′54″
960529	02h21m19.8s	02h19m57.3s	02h22m17.3s	02h23m43.3s
	+83°25′33″	+83°18′07″	+83°22′38″	+83°30′03″
961230	20h37m25.6s	20h36m34.9s	20h35m58.9s	20h36m50.3s
	−68°58′27″	−68°44′07″	−69°13′09″	−69°27′29″
970815	16h08m18.7s	16h06m16.7s	16h08m47.1s	16h10m51.1s
	+81°32′00″	+81°27′14″	+81°29′32″	+81°34′15″
970828	18h08m42.4s	18h07m58.6s	18h08m36.9s	18h09m20.7s
	+59°19′33″	+59°18′08″	+59°17′00″	+59°18′25″
980703	23h59m07.0s	23h59m23.3s	23h59m02.0s	23h58m45.7s
	+08°32′05″	+08°38′01″	+08°34′43″	+08°28′47″

Table 5-3: Corners of Multiple-SSC Error Boxes

Date of GRB (yymmdd)	Instrument	R.A. of Center (J2000)	Decl. of Center (J2000)	Radius (Degrees)
960416	BATSE	04h27m24s	+73°36′0″	4.8
961019	BATSE	21h27m29s	−84°10′50″	5.0
970815	BATSE	15h37m58s	+81°42′0″	4.0
970815	*ASCA*	16h06m54s	+81°30′34″	0.0167 [113]
970828	BATSE	17h56m53s	+59°25′10″	4.8
970828	*ASCA*	18h08m30s	+59°19′20″	0.025 [113]
970828	*ROSAT*	18h08m31.7s	+59°18′50″	0.00278 [51]
971024	BATSE	18h01m53s	+49°38′20″	6.9
971214	BATSE	12h03m19s	+66°12′40″	4.1
971214	*BeppoSAX*- WFC	11h56m30s	+65°12.0′	0.065 [58]
971214	*BeppoSAX*- NFI	11h56m25s	+65°13′11″	0.0167 [2]
980703	BATSE	23h56m17s	+12°00′40″	4.0
980703	*BeppoSAX*- NFI	23h59m07s	+08°35′33″	0.0139 [44]

Table 5-4: Sizes of Error Circles

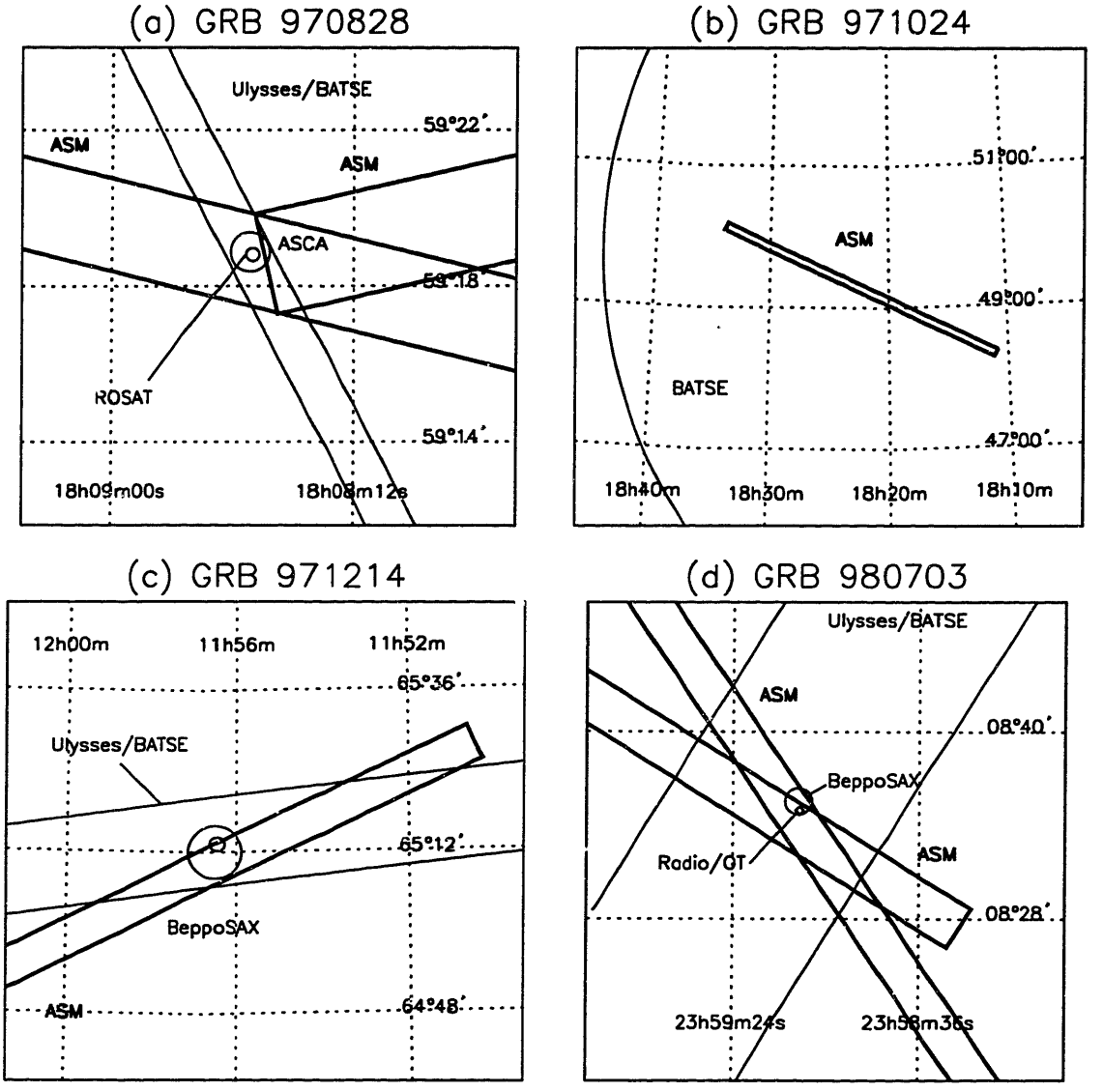

Figure 5-3 The ASM localizations of four GRBs, shown with position information from other satellites when available. See caption for Figure 5-1.

the fading X-ray flux within 4 h, confirming the ASM position [100]. An IPN annulus based on BATSE and *Ulysses* detections was made available about 1 d after the ASM report [72]. A fading X-ray source was observed with *ASCA* over the interval of 1.2 to 2.1 days after the burst trigger [114]. Later ROSAT observations narrowed the position to within a radius of 10″ [51]. Optical and radio instruments observed this location within 4 h of the trigger time, but despite intense monitoring over the following weeks, no counterpart was seen at wavelengths longer than X-rays [52].

GRB 971024 (Figure 5-3b) was detected in two cameras, but the event proved to be extremely weak in the ASM energy band. Due to its position near the edge of the field of view of SSC 2, only 159 counts were detected. The position analysis described above indicates that positions for detections this weak are unreliable, so we do not report an error box from this SSC. The error box derived from the detection of GRB 971024 in SSC 1 is shown in Figure 5-3b. Because of the extremely large error region, very little follow-up was performed. No candidate counterpart was reported [163, 76].

GRB 971214 (Fig. 5-3c) was detected by SSC 3 within a single dwell. We reported a line of position via the GCN about 2.3 h after the event. This GRB was also detected with BATSE and *Ulysses*, and the resulting IPN annulus, reported two days later, was 7.9′ in width [78]. The error box reported here is smaller in area than that initial position by about a factor of three. This burst was also detected simultaneously and independently in the Wide-Field Camera of *BeppoSAX*, generating a 99% confidence error circle 3.9′ in radius [58]. This region was further reduced through pointings by the Narrow-Field Instruments (NFI), which localized a fading X-ray counterpart to 1′ [2]. The two error circles are shown in Figure 5-3c. A fading optical source was quickly identified [55], and later observations indicated that the host galaxy candidate had a redshift of $z = 3.42$ [87].

GRB 980703 (Figure 5-3d) was a bright burst that was also detected by BATSE. Its onset was recorded in two ASM SSCs simultaneously, leading to a pair of crossed

error boxes. The ASM position was first reported $\sim$ 12 h after the event [93]. Observations with the *BeppoSAX* NFI of a region centered on the ASM localization were performed at 22 h after the BATSE trigger. A fading X-ray source was reported to be within a circle of 50″ radius [44]. An IPN annulus 18.4′ in width was made available within 3 d [71]. The final IPN annulus reported here is 13.5′ wide; it is consistent with the ASM and *BeppoSAX* measurements. Radio and optical observers were also able to identify counterparts [36]. Later spectroscopy revealed a redshift of $z = 0.9653 \pm 0.0007$ [24], the third cosmological redshift to be measured for a GRB source.

5.2.2 An ASM Self-Trigger

Fourth, in September of 1997, we established a "self-trigger" system, in which the incoming time-series data is checked for excess variability using the same criteria developed during the archival search described above. Dwells with significantly non-linear time series sequences are flagged as possible GRB events. If the standard cross-correlation analysis also reports a possible new source detection at better than 5 σ significance, an email alert is distributed. If BATSE and/or *BeppoSAX* data indicate that a GRB was active during the time of the dwell, the significance limit is lowered to 3 σ, to ensure that a dim GRB does not slip through the system. This system has detected one GRB so far that was not also detected by BATSE.

GRB 981220 (Figure 5-4) was detected by SSC 2 during a single dwell, and an alert was distributed 32 h after the initial event. An IPN annulus 2.4′ wide was rapidly calculated, using *Ulysses* and KONUS detections [69]. Although no optical transients were reported, a rapidly varying radio source was discovered within the ASM/IPN error box and attributed to GRB 981220 [46, 37]. The final IPN annulus reported in Table 5-5 is 0.8′ wide and excludes this radio source as a counterpart to GRB 981220. Further monitoring with the VLA has shown that the behavior of this source's light curve does not resemble that of other GRB afterglows [39]. This radio source is

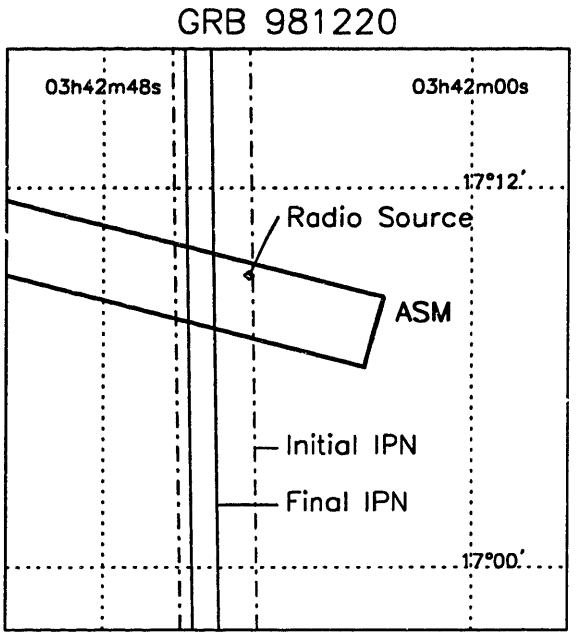

Figure 5-4 The ASM localization of GRB 981220, shown with two IPN annuli constructed by triangulation of burst arrival times at *Ulysses* and KONUS/*WIND*. The radio source at α = 03h42m28.98s±0.07s, $\delta = +17°09'14.7'' \pm 1.6''$ (J2000) was discovered by Galama et al. [46] and found to be highly variable by Frail & Kulkarni [37]. The final IPN annulus (Table 5-5) excludes this radio source as a counterpart to GRB 981220, and further monitoring with the VLA shows behavior inconsistent with that of other GRB afterglow at radio wavelengths [39].

therefore most likely unrelated to GRB 981220. The nature and characteristics of any afterglow from GRB 981220 remain unknown at this time.

5.3 Near-Misses and Borderline Cases

Seven detections of five of these thirteen bursts yielded numbers of counts low enough for the chance that each of the derived positions is spurious to be greater than about 7%. The probabilities of spurious detections in each coordinate as predicted by Equation 4.2 are given in Table 5-6 for all ASM GRB detections. Three weak bursts,

GRB 961019 (Fig. 5-2a), GRB 971024 (Fig. 5-3b), and GRB 971214 (Fig. 5-3c), have positions derived from BATSE, IPN, or *BeppoSAX* which confirm the ASM positions. In the case of GRB 961019 (Fig. 5-2a), the IPN annulus significantly reduces the size of the error box. In the case of GRB 961230 (Fig. 5-2c), the weak ASM positions confirm each other (the probability that two spurious boxes overlap by chance is less than 10^{-3}), but there are no independently derived positions to compare with the ASM error region for GRB 961029 (Fig. 5-1d).

Three further GRBs (GRB 961216, GRB 971216 and GRB 981005) had BATSE positions that were consistent with the ASM FOV at the time of trigger, and ASM analysis indicated the presence of uncatalogued X-ray source candidates in the FOV of at least one SSC. In the case of GRB 961216, a $\sim 4\sigma$ peak was detected less than a degree from the edge of the FOV of a single SSC. This position lies outside the region of the FOV included in the present analysis, so we do not report it here. Observations at the times of GRB 971216 and GRB 981005 were more complex. The highest peaks in the cross-correlation maps derived from SSCs 1 and 2 had low significance ($\sim$2–4σ), fell below the 200-count lower limit for reliability, and mapped to inconsistent celestial locations. We are therefore unable to report reliable detections for either of these bursts. Furthermore, we cannot provide useful upper limits for the X-ray fluxes from these GRBs, since it is possible that the actual GRB sources were located outside the FOV of the ASM during all of these observations.

Although we know of no other bright, burst-like events in the ASM database that we cannot identify, it is possible that the ASM has detected GRBs other than the ones reported here. Our understanding of how to distinguish real short-lived X-ray events from solar- or particle-induced events has improved since the archival search described above was completed. The difficulty in identifying real events in the archival search led us to exclude approximately one-third of the data from consideration. We may also miss GRBs in the real-time search, if the telemetry stream from the satellite is interrupted by internet or server outages on the ground, or if the packets are received

Date of GRB (yymmdd)	Instruments[1]	R.A. of Center (J2000)	Decl. of Center (J2000)	$3-\sigma$ Full-width (Arcmin)	Radius (Degrees)
960416	ub	10h09m15.65s	+67°07′36.8″	23.9	25.706
960727	uk	10h37m45.44s	+42°05′13.3″	1.4	82.222
961002	uk	23h30m18.78s	−33°07′44.4″	2.1	81.847
961019	ub	23h41m20.75s	−31°52′58.3″	11.0	48.530
970815	ub	10h38m36.27s	+20°33′43.9″	2.8	68.519
970828	ub	10h46m12.46s	+19°10′18.6″	1.1	83.514
971214	ub	11h32m40.33s	+11°03′06.3″	13.2	54.331
980703	ub	22h06m35.40s	−9°03′55.7″	13.5	33.132
981220	uk	23h09m29.47s	+7°20′04.3″	0.8	67.142

Table 5-5: Dimensions of IPN Annuli

out of order. These problems are corrected in production data, which are available ~1–4 days after the observations, but these data are not currently being searched for GRBs. Projects to reprocess the archival data and utilize the production data to create a complete ASM GRB catalog are planned.

[1] u - *Ulysses*; b - BATSE; k - KONUS

Date of GRB (yymmdd)	SSC Number	Number of counts	Chance of spurious detection in ϕ (%)	Chance of spurious detection in θ (%)
960416	1	997	2	3
960416	2	1424	4	2
960529	1	1035	1	3
960529	1	1043	1	3
960529	2	2223	3	2
960727	2	1899	3	2
961002	2	1498	4	2
961019	2	297	23	38
961029	2	289	24	41
961230	1	329	8	12
961230	2	386	14	19
970815	2	1060	4	3
970815	1	4843	1	2
970815	2	3769	3	1
970828	1	1348	1	3
970828	2	1230	4	3
971024	1	303	10	14
971214	3	662	6	13
980703	1	1539	1	3
980703	2	1622	3	2
981220	2	2236	3	2

Table 5-6: Probability of Misidentifying Weak Bursts

Chapter 6

Fireballs and Shocks

The first unambiguous identification of X-ray and optical afterglows from a single GRB was achieved on February 28, 1997 [160], as described in Section 2.4. The flux of the transient source was found to decay as a power law in all wavelengths, apparently with the same index independent of bandpass [171]. This result was immediately hailed as a confirmation of the predictions of the "fireball" model for GRB emission, in which a relativistically expanding plasma interacts with a cold surrounding medium to produce synchrotron radiation that fades as the remnant expands [105, 166]. The properties of this model were also successfully employed by Wijers & Galama to explain the spectral evolution of the afterglow from two further GRBs [170]. Successes like these have led to the general adoption of the fireball model as the most popular explanation for the origin of GRBs.

The term "fireball" defines an opaque plasma of high-energy radiation and electron-positron pairs, along with some small component of ionized hydrogen, that has an initial energy significantly greater than its rest mass. The evolution of this fireball can be described by an extension of the solution to the "strong explosion problem" developed by Sedov [139], Taylor [156], and von Neumann [162] in the late '40s. The self-similar solution developed by these authors, known today as the "Sedov-Taylor" solution, describes a shock wave expanding into uniform surroundings. It has been

applied successfully to the adiabatic stage of supernova remnant evolution. Blandford & McKee (1976) later extended this solution into the relativistic regime [8], and Cavallo & Rees (1978) shortly thereafter applied the model to the question of gamma-ray burst origins, outlining qualitatively several possible paths for the evolution of the fireball [12]. Goodman (1986) and Paczyński (1986) described the evolution of a fireball with no matter component [49, 119], and then Shemi & Piran (1990) considered the effects of contaminating baryons [142].

Today, it is widely accepted that the observed radiation from the GRB and its afterglow does not originate in the fireball itself, but rather is emitted when the expanding plasma undergoes shocks. There are two primary interactions that can generate shocks: as the fireball expands, it will sweep up the surrounding material, which may be typical interstellar medium or may include a wind that was ejected from the GRB progenitor prior to the explosion. Mészáros & Rees (1992) first explored this kind of shock [104, 126], and their model has become successful in explaining many properties of the observed afterglow. It is also possible that inhomogeneities in the fireball itself will lead to different regions with differing bulk Lorentz factors. As the faster regions catch up with the slower regions, they will build up internal shocks. Narayan, Paczyński & Piran (1992) suggested that these shocks produce the prompt emission of the GRB itself [115].

In this chapter, I will outline the "fireball" model, how it leads to internal and external shocks in the outflow of material from the burst site, and how these shocks might produce the observed radiation in the GRB. Along the way, I derive key parameters and scale values, and I highlight several predictions for the global characteristics of GRB emission that can be used to interpret the features observed in the GRB light curves presented in Chapter 7. This chapter represents no original work on my part; it is a synthesis of the salient features of models already presented in the literature. A comprehensive review was recently written by Piran [120].

6.1 The Fireball Model

The standard description of a GRB begins with a large amount of energy (typically $E_0 \sim 10^{52}$ ergs) in the form of photons and electron-positron pairs in a small volume along with some amount of ionized hydrogen plasma. The relation between the rest mass of the baryons and the total energy in the event is conveniently defined via the equation $E_0 = \eta M_0 c^2$. M_0 in this case represents the rest mass of the baryons mixed in with the photon-lepton plasma. There may be more mass present within the progenitor object, but this mass is not ejected in the fireball, and hence is not included as part of M_0. The nature of the progenitor event is not addressed in this discussion. There are many specific suggestions for what types of events could cause that much energy to be released in a small volume, although most of them fall into two broad categories: the collision of two compact objects or the sudden collapse of the core of a massive star into a black hole. However, the evolution and characteristics of the aftermath proceed in much the same manner, regardless of the cause of the explosion.

The first critical characteristic of a dense photon-lepton plasma is that it is opaque. This counter-intuitive result was first explored by Goodman [49], and I follow his presentation here. He noted that if one assumes the plasma is at thermal equilibrium, one can estimate the energy density by integrating the Planck function:

$$\frac{E_0}{4\pi R_0^3/3} = \frac{\pi^2}{15}\frac{(kT)^4}{(\hbar c)^3}. \tag{6.1}$$

This equation can be solved for R_0. If we define $E_{52} \equiv E_0/10^{52}$ erg and $\Theta_6 \equiv kT/1$ MeV, then the solution has the form

$$R_0 = 2 \times 10^8 \text{ cm } E_{52}^{1/3}\, \Theta_6^{-4/3}. \tag{6.2}$$

The scale factor in this equation is on the order of the size of the Earth ($R_\oplus \sim$

6×10^8 cm), a very small scale in astrophysical terms.

The energy density is high enough that there will be copious collisions between photons to produce electron-positron pairs. This interaction can occur if the joint energy of the photons is more then the rest mass of the two leptons. With a large population of pairs present, the photons will also scatter off of the leptons via Thomson scattering. If we assume thermal equilibrium, and we assume the pairs dominate over any residual electrons associated with local hydrogen, and we assume that the fraction of photons with $E > m_e c^2$ (This fraction is defined as f_g, and m_e is the electron mass.) is close to one, there will be roughly the same density of photons and leptons. We can therefore compute the optical depth of the plasma to Thomson scattering, to within factors of order unity, as

$$\tau = n_e \sigma_T \, R_0, \tag{6.3}$$

where n_e is the lepton density, and $\sigma_T = 6.7 \times 10^{-25}$ cm^2 is the cross-section for Thomson scattering.

If we assume that the typical photon has an energy $\sim kT$, then the photon density (and hence the lepton density) is just the energy density from Equation 6.1 divided by kT. The optical depth of the plasma due to Thomson scattering is then (again to within factors of order unity)

$$\tau \sim \frac{\pi^2}{15} \frac{(kT)^3}{(\hbar c)^3} \sigma_T \, (2 \times 10^8 \text{ cm}) \, E_{52}^{1/3} \, \Theta_6^{-4/3} = 1.5 \times 10^{16} \, E_{52}^{1/3} \, \Theta_6^{5/3}, \tag{6.4}$$

a huge number. The total optical depth will be even higher, because there will be an additional contribution from the photon-photon collisions that produce the electron-positron pairs.

If, then, the total optical depth of the plasma is high, the vast majority of the radiation cannot simply escape into space. Photons that are not at the outermost edge of the region will scatter before they can escape. The photons are strongly

coupled to each other due to pair production and Compton scattering, and to the leptons via Thomson scattering, which implies that the fireball behaves like a single fluid. Any baryons present will be dragged along with the photon-lepton fluid by electromagnetic forces, so the two components can, at least initially, be treated as one.

The pressure of this fluid will be much higher than that of the surrounding medium, and the fluid will expand. This expansion is covered in great detail in, e.g., Kobayashi, Piran, & Srai [83], and I will simplify their discussion here. The initial acceleration phase of the expansion is also termed the "radiation dominated" phase because most of the energy is in the photon/lepton gas, i.e., η is large, and $e \gg \rho c^2$, where e is the energy density and ρ is the mass density. Conservation of energy and momentum in a relativistic fluid expanding at a Lorentz factor Γ yield the conservation laws $r^2 e^{3/4}\Gamma = \text{constant}$, and $r^2\Gamma^2(\rho c^2 + 4e/3) = \text{constant}$ [168, 121]. In the radiation-dominated regime ($e + \rho c^2 \approx e$), these two equations imply $\Gamma \propto r$.

As the plasma accelerates, the bulk kinetic energy of the fireball is increasing, so the energy in the radiation must be decreasing. At the "acceleration radius", when the bulk Lorentz factor of the fireball reaches η, the bulk kinetic energy of the plasma is equal to the initial available energy in the fireball, and the plasma will coast at a constant Lorentz factor $\Gamma \sim \eta$. The radius at which this transition occurs is then estimated by $R_a \sim \eta R_0$. Beyond this radius, the energy of the explosion is contained in the bulk motion of the plasma, and there is no available energy for radiation. Equation 6.2 implies that R_a is approximately:

$$R_a = 6 \times 10^{10} \text{ cm } \Gamma_{300}\, E_{52}^{1/3}\, \Theta_6^{-4/3}, \tag{6.5}$$

where $\Gamma_{300} \equiv \Gamma/300$. For most quantities in this discussion, I use the convention $A = 10^x\, A_x$, but for Γ and η I use $A = xA_x$. This is to avoid confusion later, when the subscript 2 will be used to designate the region within a forward shock.

If $\eta < 1$, the fireball is matter-dominated and will never achieve relativistic speeds. This immediately constrains the amount of baryonic matter that can be present in the fireball. In order to reach relativistic speeds, $\eta \gg 1$, or $E_{52}\ 10^{52}$ erg $\gg M_0\ c^2$, implying $M_0 \ll (E_{52}/c^2)\ 10^{52}$ erg $= 10^{31}\ E_{52}$ g, or $M_0 \ll E_{52}\ 10^{-2}\ \mathrm{M}_\odot$. For the fireball to be highly relativistic, with $\Gamma \gtrsim 1000$, $M_0 \lesssim E_{52}\ 10^{-5}\ \mathrm{M}_\odot$. This is a strong constraint, as presumably the progenitor of a GRB will involve at least several solar masses of material. The model demands that only a tiny fraction of that material actually be ejected in the fireball. Compare this value to that of a supernova, where approximately $10^{-1}\ M_\odot$ of matter is ejected to become the supernova remnant.

As the gas expands, the temperature will fall, until $kT \sim 0.5$ MeV, after which the photon gas won't have enough thermal energy to sustain the pair production. For the discussion of this transition, I follow the dimensional analysis in [120]. The optical depth for $\gamma\gamma \to e_+e_-$ will plummet exponentially, because the occupation number of a fermion distribution depends exponentially on temperature. If the fireball has not yet reached R_a, there will still be thermal energy available, and the radiation will emerge at the temperature associated with this transition time.

An absolutely critical fact for constraining the evolution of the fireball model with respect to GRBs is that the observed spectra of GRBs are non-thermal. The emission (the cause of which I will address in the next section) must escape without being thermalized, so the GRB must occur after the optical depth to pair production drops to unity. This places a lower limit on the Lorentz factor of the ejecta.

Assume that the ejecta at late times is contained in a shell of width Δ, expanding symmetrically at a high Lorentz factor $\Gamma \sim \eta$. By conservation of energy, the total energy in this shell is still E_0, so the energy density is $E_0/(4\pi R^2\Delta)$. Since we are assuming that the shell maintains thermal equilibrium until it becomes optically thin, the photon density near the transition will be the same as the lepton density, so the photon density will be on the order of $E_0/(4\pi m_e c^2 R^2\Delta)$. The optical depth of a shell due to pair production is given by a modified Equation 6.3: $\tau = f_g n_g \sigma_T \Delta$, where n_g

is the photon density in the shell, and f_g is the fraction of the available photons that can produce pairs. The cross section for pair production is on the order of the cross section for Thomson scattering because the Feynman diagrams for the two processes are identical.

One can estimate f_g by integrating the observed photon spectrum above 0.5 MeV, but photons arriving at the observer will be blue-shifted relative to their energy as emitted in a frame moving with the shocked fluid. The number of available photons at a given energy in the comoving frame will therefore be reduced relative to the observed number by a factor of Γ. If the energy spectrum goes as $dF/d\nu \propto \nu^{-\alpha}$, then the total number of available photons at a given energy in the comoving frame will be less than the observed number by a factor of $\Gamma^{-\alpha}$. Since it takes two photons to collide and produce pairs, the total fraction of available photons will drop by a factor of $\Gamma^{-2\alpha}$ in the comoving frame relative to the observed spectrum.

In the frame of a distant observer (assumed to be at rest with respect to the explosion site), light emitted at the same local time from a spherically expanding shell will arrive at the observer at different times, such that the apparent shape of the shell is distorted into an ellipse as shown in Figure 6-1. Relativistic effects therefore allow the radiation observed at time t after the explosion to be emitted from a radius larger than vt by a factor on the order of $2\Gamma^2$ [125]. Observations of GRBs indicate that the shortest time-scale upon which they vary is $\delta T \sim 10$ ms. Light travel-time arguments imply that the expanding shell must have a radius less than $\sim c\delta T$, but the relativistic expansion implies that the actual radius is larger, $R \sim 2\Gamma^2 c\delta T$.

The optical depth of a shell that is expanding at $v \approx c$ is therefore

$$\tau = n_g \frac{f_g}{\Gamma^{2\alpha}} \sigma_T \Delta = \frac{f_g}{\Gamma^{2\alpha}} \frac{E_0 \sigma_T}{4\pi c^2 R^2 m_e} \tag{6.6}$$

$$\tau = \frac{f_g}{\Gamma^{4+2\alpha}} \frac{E_0 \sigma_T}{16\pi c^4 m_e (\delta T)^2} \sim \frac{2 \times 10^{15}}{\Gamma^{4+2\alpha}} E_{52} f_p \left(\frac{\delta T}{10 \text{ ms}} \right)^{-2}. \tag{6.7}$$

In order, then, for emission to escape as non-thermal radiation with a spectral index

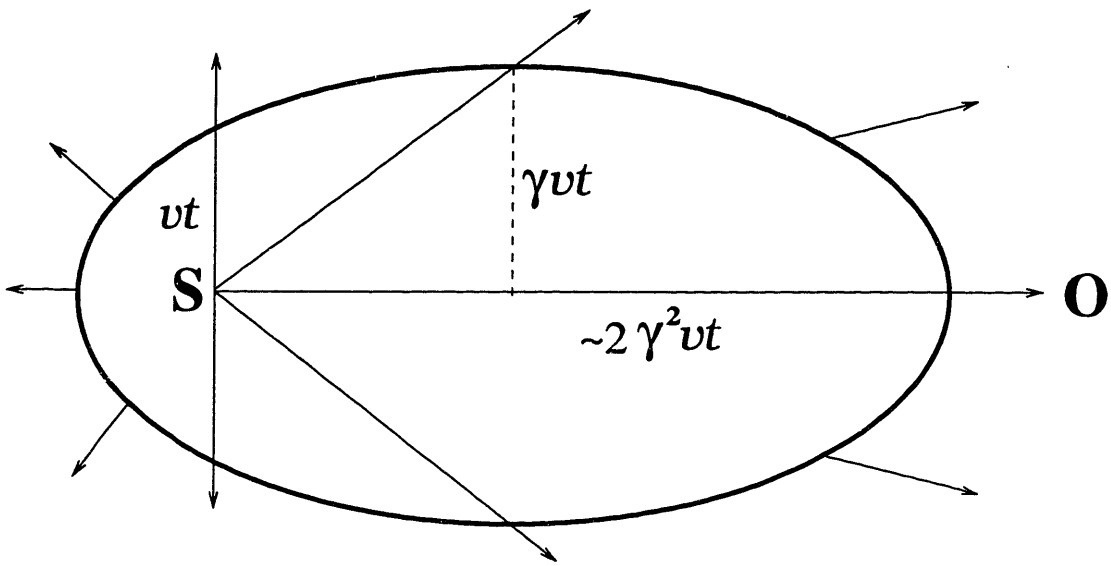

Figure 6-1 A diagram adapted from Figure 1 in Rees [125]. If a radiating shell expands from point **S** with spherical symmetry at a highly relativistic speed (Lorentz factor γ), photons that arrive at the location of a distant observer (in the direction of **O**, at rest with respect to the explosion center) at the same time t will have been emitted from an ellipse from an ellipsoid with a projected eccentricity $\epsilon = v/c$ and semi-latus rectum $\alpha = vt$. The radius along the line of sight is then $\gamma^2 vt(1 + v/c)$, which is $\sim 2\gamma^2 ct$ for $v \sim c$. This is the true radius of the shell at time t, but only emission from the nearest point has had time to reach **O**. Radiation observed from other parts of the shell at the same time in the observer frame was emitted at earlier times in the frame moving with the shell.

of $\alpha = 2$, Γ must be greater than about 10^2. This limit is highly sensitive to the value of α. Observations show that the high energy spectral index can vary from ~ 1.6 to higher than 5, with no particular preferred value [5]. Although 100 is often cited in the literature as a lower limit on Γ, the observed range of α allows the lower limit on Γ to be as low as 12 (for $\alpha = 5$). Still, even a lower limit of $\Gamma > 12$ corresponds to remarkably high velocities, as typical relativistic jets around AGN or microquasars only achieve Lorentz factors on the order of a few, 10 at the highest. Fireballs must be extremely relativistic objects to emit non-thermally.

The presence of additional electrons associated with baryonic matter produces an additional opacity that will cause the plasma to remain optically thick past the point when pair production ceases. The radius at which the ejecta becomes completely optically thin, referred to as the "transparency radius", can be estimated by a similar analysis of the optical depth to Thomson scattering in the ejecta shell. Lazzeti, Ghisellini and Celotti [92] use the values of this radius and other radii of interest to place constraints on Γ. I simplify one of their arguments here. In this case, however, the particle density will be determined by the amount of hydrogen contamination in the shell, because transparency to the electron-positron pairs will occur prior to complete transparency. We also assume that this transition occurs before any appreciable mass is swept up from the external medium, i.e. we assume the fireball is expanding into a vacuum. Thus, if we define m_p as the mass of a proton, the electron density (which we assume is the same as the proton density to make the plasma globally neutral) is $n = M_0/(4\pi m_p R^2 \Delta)$, and the optical depth is $\tau = (M_0 \sigma_T)/(4\pi m_p R^2)$ [92]. Define R_τ as the radius for which $\tau \sim 1$, remember $\Gamma M_0 c^2 = E_0$, and the resulting equation for R_τ is

$$R_\tau = \left(\frac{E_0 \sigma_T}{4\pi m_p c^2 \Gamma}\right)^{1/2} = 3 \times 10^{13} \text{ cm } E_{52}^{1/2} \, \Gamma_{300}^{-1/2}. \tag{6.8}$$

If the fireball becomes optically thin while it is still radiation-dominated ($R_\tau < R_a$), most of the energy will escape as thermal radiation from a high-temperature plasma. If the fireball becomes matter-dominated before it becomes optically thin

($R_\tau > R_a$), then it will radiate very little, as most of the energy is in the relativistic bulk motion of the plasma, and very little is available for radiative losses. The spectra of GRBs are non-thermal, so it is believed that the latter scenario is the path that is most likely to be followed by GRB evolution. The condition that $R_\tau > R_a$ places a constraint on Γ, namely that $\Gamma < 2 \times 10^4 \, E_{52}^{1/9} \, \Theta_6^{8/9}$ (Equations 6.8 and 6.5).

If the initial state is a dense region of high-energy photons, and the final state is the emission of a non-thermal spectrum as observed from gamma-ray bursts, the evolutionary scenario for a fireball describes an initial rapid acceleration to a bulk Lorentz factor $\Gamma \sim \eta$, followed by a coasting phase until the optical depth of the expanding material drops to one. This scenario implies that Γ, and hence η, be constrained to be $10^2 \lesssim \Gamma \lesssim 10^5$. The immediate problem with this scenario so far is that there is no actual burst. In the coasting phase, even after the optical depth drops to unity, there is no available energy to generate radiation. The radiation associated with the GRB event (including any afterglow) is believed to originate in shocks that develop as the plasma expands into the surrounding medium.

6.2 External Shocks

As the fireball expands, it will sweep up the mass in its local environment. At first, the swept-up mass will have a negligible effect on the shell, but over time, the mass will decelerate the leading edge of the fireball. After the ejecta undergoes significant deceleration, a pair of shocks will form: a shock front expands forward into the medium and a second shock front moves back into the blast wave (in the frame comoving with the boundary). A schematic diagram of four regimes in the region around the shocks is shown in Figure 6-2. In the following discussion, a regime near the shock front will be referenced by appending a subscript to the variables describing the properties of that regime. A subscript of 1 refers to conditions upstream and a subscript of 2 refers to conditions downstream of the forward shock front.

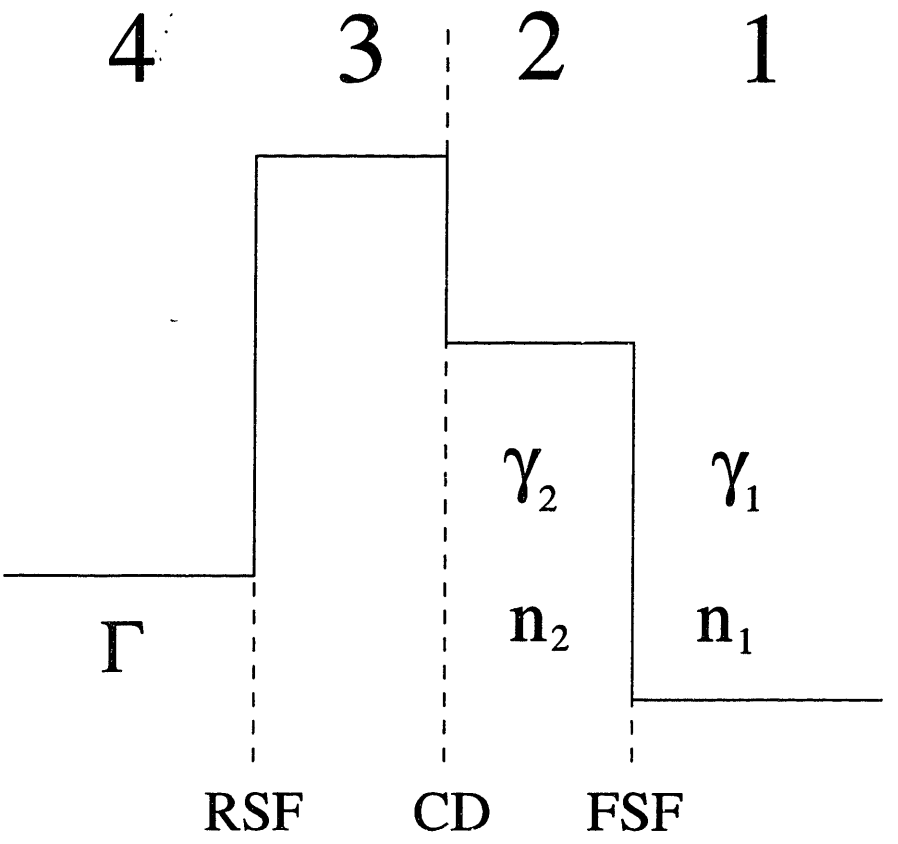

Figure 6-2 A shock generically forms four regions, separated here by dashed lines. The solid line represents the density, n_i, in each region i. The upstream region, labelled 1, is the undisturbed surrounding medium. The downstream region, labelled 4, is the blast wave, expanding with a Lorentz factor Γ. As the material in region 4 sweeps up the material in region 1, a forward shock front (FSF) will form at the contact discontinuity (CD) between the two regimes. This front will expand into region one slightly faster than the speed of the material within the shock, which moves at γ_2 with respect to the observer frame, $\gamma_1 = 1$. At the time the shock forms, $\gamma_2 = \Gamma$. As material from region 4 plows into region 2 from behind, a reverse shock front (RSF) will form that propagates backwards in the frame of region 2. Within the simplified scenario presented in this chapter, I assume that region 3 is short-lived and I ignore its contribution to the evolution of the system.

Sari, Narayan, and Piran [132] and Sari & Piran [133] give a full discussion of the differences between the forward and reverse shock, but for the moment, I will continue the discussion as if only the forward shock were relevant.

How much mass must be swept up to cause a significant deceleration? To answer this question, I follow Piran [120], and I consider the effect of a series of inelastic collisions between the fireball and a small amount of external mass. The fireball has an effective mass of M (rest mass plus the internal thermal energy over c^2), moving with bulk Lorentz factor γ_2. The external mass is approximated by a symmetrical shell of mass dm. We assume that the radiative losses are negligible, and we define an effective mass after the collision as M', moving with a Lorentz factor γ_2'. We then use the conservation of momentum and energy to compare the conditions before and after the collision:

$$\gamma_2 M v = \gamma_2' M' v' \tag{6.9}$$

$$\gamma_2 M c^2 + dm\ c^2 = \gamma_2' M' c^2 \tag{6.10}$$

I use these equations to eliminate the primed quantities and derive relations between the swept up mass, the rest mass of the fireball, and the bulk Lorentz factor of the shocked mass. Since $\gamma^2 \equiv (1 - (v/c)^2)^{-1}$, we can eliminate v and v' in Equation 6.9. We can then use Equation 6.10 to eliminate M'. Under the assumption that dm is very small, one can derive to first order that

$$\frac{d\gamma_2}{\gamma_2^2 - 1} = -\frac{dm}{M} \tag{6.11}$$

Apply this equation to Equation 6.10 to show that (again to first order) $dM = \gamma_2\ dm$. Physically, this means that the external matter contributes more effective mass to the fireball than its rest mass, by a factor of γ_2.

One can therefore rewrite Equation 6.11 in terms of just γ_2 and M, and integrate both sides from an initial state with mass M_0 and Lorentz factor Γ to some arbitrary M and γ_2. That is, the shock is presumed to form after the fireball has reached its

matter-dominated, coasting phase, moving with the bulk Lorentz factor $\Gamma \approx \eta$ as derived in the previous section. One thus obtains a relation between M and γ_2:

$$M = M_0 \left(\frac{\Gamma^2 - 1}{\gamma_2^2 - 1} \right)^{1/2} . \tag{6.12}$$

Again we return to Equation 6.11 and use Equation 6.12 to eliminate M. We thus achieve a differential equation in γ_2 and m, which we can integrate to arrive at an equation for the swept-up mass as a function of the fireball bulk Lorentz factor, under the assumption that $\gamma_2 \gg 1$. Begin with Equation 6.12 substituted into Equation 6.11:

$$\frac{d\gamma_2}{\gamma_2^2 - 1} = -\frac{dm}{M_0} \left(\frac{\gamma_2^2 - 1}{\Gamma^2 - 1} \right)^{1/2} . \tag{6.13}$$

Group like variables and integrate the left side from Γ to γ_2 and the right side from 0 to m (a subscript i indicates a dummy variable for integration):

$$\int_\Gamma^{\gamma_2} \frac{d\gamma_i}{(\gamma_i^2 - 1)^{3/2}} = -\frac{m}{M_0(\Gamma^2 - 1)^{1/2}} \tag{6.14}$$

If we assume $\gamma_2 \gg 1$, then the integral becomes trivial, and

$$m = \frac{M_0 \, \Gamma}{2} \left(\frac{1}{\gamma_2^2} - \frac{1}{\Gamma^2} \right) \tag{6.15}$$

The swept-up mass therefore goes as $M_0 \Gamma \gamma_2^{-2}$, which means that $mc^2 = E_0(\gamma_2^{-2} - \Gamma^{-2})/2$.

Once the expanding fireball has swept up a mass $m \sim E_0(c\Gamma)^{-2}$ of material, the ejecta will experience significant deceleration ($\gamma_2 \sim \Gamma/\sqrt{3}$). It is straightforward to estimate the radius and time associated with this γ_2, and one can also chart the subsequent evolution of the system.

If the ambient medium is a spherically symmetric distribution of cold hydrogen at constant density ($\rho_1 = m_p n_1$), the swept-up mass is ρ times the spherical volume

enclosed by the shell: $m = 4\pi R^3 m_p n_1/3$. Since $m = E_0(c\gamma_2)^{-2}$ at the deceleration radius, one can solve for R:

$$R^3 = (3\ E_0)/(4\pi\ m_p\ c^2\ n_1\ \gamma_2^2). \tag{6.16}$$

To characterize the evolution of the resulting deceleration, I follow Mészáros & Rees [105]. The swept-up mass will be distributed along a spherical shell. At a time t from the explosion, as measured by the observer, when the first information from the shock arrives, the actual spherical radius of the shell is $\sim 2\gamma_2^2 ct$ (Fig. 6-1). This means that $R^3 = (2ct\gamma_2^2)^3$, which can be substituted into Equation 6.16:

$$(2ct\gamma_2^2)^3 = \frac{3\ E_0}{4\pi\ m_p\ c^2\ n_1\ \gamma_2^2}. \tag{6.17}$$

This equation yields $\gamma_2 \propto t^{-3/8}$, which can be cast in terms of the conditions at the time of deceleration, when $\gamma_2 \approx \eta$:

$$\gamma_2(t) = \eta(\frac{t}{t_{\rm dec}})^{-3/8}. \tag{6.18}$$

Equation 6.18 can be substituted into Equation 6.17 to yield

$$R(t) = R_{\rm dec}(\frac{t}{t_{\rm dec}})^{1/4}. \tag{6.19}$$

To estimate the scale of the numbers at which these events occur, define $E_{52} \equiv E_0/10^{52}$ erg, $\eta_{300} \equiv \eta/300$, and let n_1 be expressed in units of cm^{-3}, as in Wijers & Galama [170], then the original rest mass of the baryons in the fireball is $M_0 \sim 10^{-5}\ {\rm E}_{52}\ \eta_{300}^{-1}\ {\rm M}_\odot$ (from $E_0 = \eta M_0 c^2$), and Equation 6.17 yields

$$R_{\rm dec} = 3 \times 10^{16}\ (\frac{E_{52}}{n_1})^{1/3}\ \eta_{300}^{-2/3}\ {\rm cm} \tag{6.20}$$

and

$$t_{\rm dec} = 10\ (\frac{E_{52}}{n_1})^{1/3}\ \eta_{300}^{-8/3}\ {\rm s}. \tag{6.21}$$

It is important to note that nothing actually moves faster than the speed of light. But after the ejecta shell reaches its terminal velocity, it will be moving at a speed of at least 99.995% of the speed of light. This means that any episodes of emission during the $\sim 10^6$ s it takes the shell to reach the deceleration radius, as measured in the rest-frame of the observer, will seem to last only ~ 10 s as actually measured by the observer. As the shell expands beyond $R_{\rm dec}$, however, it will lag further and further behind any emitted photons.

If we define $t_d \equiv t/1$ d and substitute Equations 6.20 and 6.21 into Equations 6.18 and 6.19, we get equations for the subsequent evolution of the radius and bulk Lorentz factor (of the shocked fluid) in the frame of the observer:

$$R(t) = 3 \times 10^{17}\ (\frac{E_{52}}{n_1})^{1/4}\ t_d^{1/4}\ {\rm cm} \tag{6.22}$$

and

$$\gamma_2(t) = 10\ (\frac{E_{52}}{n_1})^{1/8}\ t_d^{-3/8}. \tag{6.23}$$

It is the evolution of this "external" shock that is believed to underlie the emission of the afterglow. It may also produce some of the high-energy emission within the GRB itself, but it has been almost universally accepted as the origin of the afterglow. Usually the emission is assumed to originate in the forward shock. Afterglow has been observed days to months after the GRB event began, and it is hard to imagine the reverse shock maintaining itself that long, since the fireball ejecta are presumed to be in a relatively thin shell (even thinner in the observer frame due to Lorentz contraction). The simplest models assume that the reverse shock is weak and/or an inefficient radiator [105], although Sari, Narayan, & Piran [132] suggest that radiation from the forward shock during short bursts would be at energies too high for BATSE to detect, and that the detected emission may originate in the reverse shock. The

emission itself is believed to be due to synchrotron radiation.

6.3 Synchrotron Cooling

In a shocked plasma, particles undergo acceleration as the bulk kinetic energy of the fluid is converted into the energy of the random motions of the component particles. The macroscopic processes of compression and heating are straightforward results of requiring the conservation of mass, momentum and energy across the shock front [143]. The details of the microscopic processes are complex and impossible to determine from first principles. However, many properties of the post-shock plasma and the evolution of its radiation can be inferred through assuming that the shock imparts a certain amount of energy into the random electron motions, and a certain amount of energy into the local magnetic field. The origin of this local magnetic field is unknown, but presumed to originate through dynamo processes within the shock and to be unrelated to any magnetic field associated with the progenitor.

Following the work of, e.g., Sari, Narayan, & Piran [132, 135], and Wijers & Galama [170], I express the redistribution of energy in terms of ratios with respect to the kinetic energy density within the shocked fluid, which is dominated by the energy of the protons. The shocked electrons will then spiral around the local magnetic field and radiate their energy primarily by synchrotron radiation.

The parameter ϵ_e is defined as the fractional energy in the motions of the downstream electrons. The post-shock thermal energy per nucleon is $\gamma_2 m_p c^2$, and the ratio of electron to nucleon density will be the same on either side of the shock. Since we are assuming only hydrogen is present, that ratio must be unity. The energy density in the electrons is $n_e \langle E_e \rangle$, so we can define the parameter as

$$\epsilon_e \equiv \frac{n_e \langle E_e \rangle}{n_p \gamma_2 m_p c^2} = \frac{\langle E_e \rangle}{\gamma_2 m_p c^2}. \tag{6.24}$$

In a post-shock plasma, it is generally presumed that the Lorentz factors of the

shocked electrons will have a power law distribution (See [1] for an example derivation.), $N(\gamma_e) \propto \gamma_e^{-p}$, above some minimum Lorentz factor $\gamma_{\rm min}$. To ensure that the total energy is finite, $p > 2$. The average energy of the electrons, $\langle E_e \rangle$, can then be calculated by direct integration:

$$\langle E_e \rangle \equiv \frac{\int_{\gamma_{\rm min}}^{\infty} N(\gamma_e)\, \gamma_e m_e c^2\, d\gamma_e}{\int_{\gamma_{\rm min}}^{\infty} N(\gamma_e)\, d\gamma_e} = m_e c^2\, \frac{\int_{\gamma_{\rm min}}^{\infty} \gamma_e^{-p+1}\, d\gamma_e}{\int_{\gamma_{\rm min}}^{\infty} \gamma_e^{-p}\, d\gamma_e} = m_e c^2\, \frac{p-1}{p-2}\, \gamma_{\rm min}. \quad (6.25)$$

This formula is then substituted into Equation 6.24:

$$\epsilon_e = \frac{m_e c^2\, \gamma_{\rm min}}{\gamma_2 m_p c^2}\, \frac{p-1}{p-2} = \frac{m_e}{m_p}\, \frac{p-1}{p-2}\, \frac{\gamma_{\rm min}}{\gamma_2}. \quad (6.26)$$

This equation can be inverted to provide an equation for $\gamma_{\rm min}$:

$$\gamma_{\rm min} = \epsilon_e\, \frac{p-2}{p-1} \frac{m_p}{m_e}\, \gamma_2. \quad (6.27)$$

The shocked electrons are expected to radiate primarily by synchrotron, and to a lesser extent Compton, processes to produce the emission observed in the GRB [132]. To derive the characteristics of that radiation, we begin in a frame comoving with the shocked fluid. We assume that the shock has jumbled up the magnetic field such that the electrons in this frame move at all possible angles with respect to the local field direction. We also begin with the simplification that all electrons are moving with the same Lorentz factor in this frame, defined as γ_e', and that the energy density in the magnetic field can be expressed as $B'^2/(8\pi)$. Primed quantities are measured in the frame of the shocked fluid, while unprimed quantities are measured in the observer frame at rest with respect to the explosion site.

Conservation laws across the forward shock front demand that the particle density obey $n_2' = 4 n_1 \gamma_2$ [8, 133]. The post-shock energy per nucleon will be $\gamma_2 m_p c^2$, so the

energy density is $e'_2 = 4\gamma_2^2 n_1 m_p c^2$. We are now ready to define a second parameter,

$$\epsilon_B = \frac{B'^2}{8\pi e'_2} = \frac{B'^2}{32\pi\gamma_2^2 n_1 m_p c^2}. \tag{6.28}$$

This can be used to define B':

$$B' = \gamma_2 \, c \, \sqrt{32\pi n_1 m_p \epsilon_B}. \tag{6.29}$$

Now, Equation 6.23 can be used to give the evolution of B' with t:

$$B'(t) = 4 \; E_{52}^{1/8} \; n_1^{3/8} \; \epsilon_B^{1/2} \; t_d^{-3/8} \; \mathrm{G}. \tag{6.30}$$

An ensemble of electrons moving relativistically at the same Lorentz factor γ'_e at random directions to a magnetic field will emit synchrotron radiation at a characteristic frequency given by [131]:

$$\nu' = \frac{3qB'\gamma_e'^2}{4\pi m_e c}. \tag{6.31}$$

I use q as a symbol for the charge of a single electron, to avoid confusion with the energy density, which I have labeled e.

However, we do not need to assume that all the electrons are moving at the same speed. As in Equation 6.25, we assume that the number of electrons with a given Lorentz factor follows a power law ($N(\gamma_e) \propto \gamma_e^{-p}$, $p > 2$) with γ_e above some minimum value γ_{min}. This means that more electrons are moving at γ_{min} than with any other value of the Lorentz factor, and that the maximum power will be emitted at the characteristic frequency corresponding to γ_{min}. That frequency, ν_m, is given by Equation 6.31 at $\gamma_e = \gamma_{\mathrm{min}}$, and we can use Equation 6.27 to eliminate γ_{min}:

$$\nu'_m = \frac{3qB'\gamma_{\mathrm{min}}^2}{4\pi m_e c} \propto B' \, \gamma_2^2. \tag{6.32}$$

Now we can use Equation 6.29 to substitute for B', and we find

$$\nu'_m \propto \gamma_2^3 \tag{6.33}$$

Since the maximum power as measured in the observer frame will be blueshifted to a frequency $\nu_m \approx \gamma_2 \, \nu'_m$, Equation 6.33 and Equation 6.23 combine to make the general prediction that the frequency of the observed peak emission will shift downward across the spectrum with time according to $t^{-3/2}$. Hence, observations of emission from the external shock in two separate bands should see a relative delay of peak emission by a factor of $(\nu_1/\nu_2)^{2/3}$.

Equation 6.33 can be inverted to place an interesting constraint on γ_2, if one knows from observation something about the frequency of peak emission. Multiply both sides of Equation 6.32 by Planck's constant, use Equation 6.29 to eliminate B' and Equation 6.27 to eliminate $\gamma_{\rm min}$. One can then solve for γ_2:

$$\gamma_2 = 14 \, \epsilon_B^{-1/8} \epsilon_e^{-1/2} n_1^{-1/8} \left(\frac{p-1}{p-2}\right)^{1/4} \left(\frac{h\nu_m}{1 \text{ keV}}\right)^{1/4} \tag{6.34}$$

Hence, a larger Lorentz factor for the shock will produce a radiation spectrum that peaks at higher energies. If observations constrain the frequency of maximum emission, this equation implies a constraint on the bulk Lorentz factor of the shocked fluid.

If the shocked plasma cools through synchrotron radiation, we can evaluate the spectral shape of the emitted radiation as well as the effect of cooling on the evolution of the system. First, we derive the spectrum of radiation if cooling does not significantly reduce the energy of the electrons. The average power emitted in the comoving frame from an ensemble of relativistic electrons with random orientations to the local magnetic field, but all moving at the same speed ($\gamma_e \gg 1$), is derived

in [131] to be

$$P'(x) = \frac{\sqrt{3}\ q^3\ B'}{m_e\ c^2}\ F(x). \tag{6.35}$$

The function is parameterized by $x \equiv \nu'/\nu'_e$, where ν'_e is the characteristic synchrotron frequency in the comoving frame

$$\nu'_e \equiv \frac{3\gamma'^2_e qB'}{4\pi m_e c}. \tag{6.36}$$

F is the standard synchrotron function,

$$F(x) \equiv x \int_x^\infty K_{5/3}(y)\ dy, \tag{6.37}$$

and $K_{5/3}$ is a modified Bessel function. Asymptotic limits for $F(x)$ at large and small values of x are

$$F(x) \sim \frac{4\pi}{\sqrt{3}\ \Gamma(1/3)}(\frac{x}{2})^{1/3}, x \ll 1, \tag{6.38}$$

and

$$F(x) \sim (\frac{\pi}{2})^{1/2}\ e^{-x}\ x^{1/2}, x \gg 1. \tag{6.39}$$

So the power radiated by an electron moving with γ'_e in a magnetic field B' will rise as $\nu'^{1/3}$ below the frequency ν'_e and drop exponentially with ν' for frequencies higher than ν'_e.

If γ'_e is greater than some critical value γ'_c, the amount of energy emitted will be a significant fraction of the kinetic energy of the electron, which will cause it to slow down, which in turn will cause its spectrum to shift to lower frequencies. The value of γ'_c is defined via the equation

$$P(\gamma'_c)t = \gamma_2 \gamma'_c m_e c^2. \tag{6.40}$$

The power and time are measured in the observer frame. The total power emitted

across all frequencies in the comoving frame is

$$P'(\gamma_e') = \frac{4}{3}\,\sigma_T\,c\,\gamma_e'^2\,\frac{B'^2}{8\pi}, \tag{6.41}$$

as derived in [131], Chapter 6, assuming $v \sim c$. To convert this into the observer frame, we use Equation 4.97b in [131]:

$$\frac{dP}{d\Omega} = \frac{1}{\gamma_2^4(1-\beta\mu)^4}\frac{dP'}{d\Omega'}, \tag{6.42}$$

where $d\Omega = d\phi d\mu$, and $\mu = \cos\theta$. Since P' is isotropic, $dP'/d\Omega'$ is simply $P'/(4\pi)$. If we assume that $\beta \approx 1$, then we can simply integrate this equation to yield $P \approx 4\gamma_2^2 P'/3$. So the emitted power in the observer frame is

$$P(\gamma_e') = \frac{4}{3}\gamma_2^2 P' = \frac{16}{9}\,\sigma_T\,c\,\gamma_2^2\,\gamma_e'^2\,\frac{B'^2}{8\pi}, \tag{6.43}$$

where Equation 6.41 is used to substitute for P'.

An evaluation of Equation 6.43 at $\gamma_e' = \gamma_c'$ allows us to find a formula for γ_c' from Equation 6.40:

$$\gamma_c' = \frac{8\pi\,m_e\,c}{\sigma_T\,B'^2\gamma_2\,t}. \tag{6.44}$$

We then use Equation 6.29 to eliminate B'.

$$\gamma_c' = \frac{3m_e}{16m_p}\,\frac{1}{\epsilon_B\,\sigma_T\,n_1\,c}\,\frac{1}{\gamma_2^3\,t}. \tag{6.45}$$

This Lorentz factor has an associated frequency in the observer frame (Equation 6.31, blueshifted) given by:

$$\nu_c = \frac{q\,B'}{2\pi\,m_e\,c}\,\gamma_2\gamma_c^2 \propto \gamma_2^{-4}\,t^{-2} \propto t^{-1/2}, \tag{6.46}$$

where we use Equation 6.29 to eliminate B', and Equation 6.23 to eliminate γ_2.

The physical meaning of Equation 6.40 is that an electron with an initial Lorentz factor $\gamma_e' > \gamma_c'$ will cool to γ_c' in the observer time t. The observed spectrum at higher frequencies than ν_c will be steeper than implied by the Bessel function solution above, and this "cooling break" will also shift downward with time as $t^{-1/2}$. At late times, therefore, one expects that both critical frequencies will have migrated below the observation frequency band, and the observed energy spectrum should have a negative slope.

This discussion has assumed that the electrons all move with the same Lorentz factor, γ_e'. To extend this treatment to the full ensemble of shocked electron energies, one must integrate the emitted power per frequency over the distribution of Lorentz factors, $N(\gamma_e) \propto \gamma_e^{-p}$. The resulting spectrum will also be a power law in ν, because $F(x)$ in Equations 6.35 and 6.37 depends on γ_e via $x \equiv \nu/\nu_e \propto \gamma_e^{-2}$. The integral of Equation 6.35 looks like

$$P(\nu) \propto \int_{\gamma_1}^{\gamma_2} P(\gamma)\, \gamma^{-p}\, d\gamma \propto \nu^{-(p-1)/2} \int_{a_2}^{a_1} F(x)\, x^{-(p-3)/2}\, dx, \qquad (6.47)$$

where $a_i \equiv 4\pi m_e c\nu/3qB_2\gamma_i^2$. Evaluation of the integral will yield a formula for $P(\nu) \propto \nu^s$. The value of s and its dependence on p will depend on the range of values of γ. For example, if $\gamma_1 \sim 0$ and $\gamma_2 \sim \infty$, then the result of the integral will be independent of ν, and

$$P(\nu) \propto \nu^{-(p-1)/2}. \qquad (6.48)$$

In a more realistic treatment, one must integrate piecewise with breaks at γ_c and $\gamma_{\rm min}$, as in [105, 170].

The broad-band emission spectrum takes the shape of a piecewise function, consisting of power laws of different indices, separated at three break frequencies: (1) ν_m, the characteristic emission frequency from electrons at $\gamma_{\rm min}$, (2) ν_c, the "cooling frequency", and (3) ν_a, the frequency below which self-absorption becomes important. ν_a generally falls in the radio bandpass, and hence will not be considered here. These

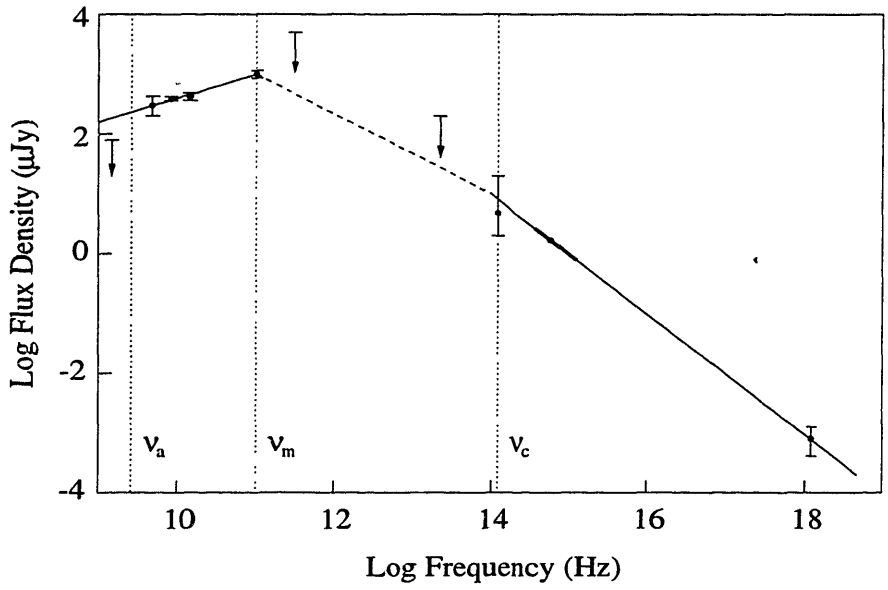

Figure 6-3 A diagram adapted from Figure 1 in Galama et al. [47]. It shows the X-ray to radio spectrum of GRB 970508 on 1997 May 21.0 UT, 12.1 d after the event. The estimated break frequencies are indicated as vertical dotted lines. The dashed line indicates an interpolated power law between the two solid lines that indicate the results of a power law fit to the data.

break frequencies will decrease with time as given in Equations 6.32 and 6.46. At late times, all observable frequencies will fall above both ν_m and ν_c, and the flux from the source should decay over time as a power law with a single index value, regardless of frequency.

The external shock model thus makes specific predictions for the temporal behavior of the GRB spectrum after the initial shock. These predictions have been confirmed in the cases of some GRB afterglows. The initial observations of the fading afterglow from GRB 970228 found (starting about eight hours after the burst) that the flux exhibited a power law temporal decay. The decay curves were consistent with the same index across many magnitudes in frequency, as predicted by the model for late times [171]. Galama et al. [47] used broadband snapshots of GRB 970508 to identify the break frequencies predicted by the model (Figure 6-3).

Although this model has proven successful enough to become the standard inter-

pretation for afterglow studies, it does not explain all aspects of GRB observations. One important complication is a limit set by the relativistic speed of the expansion, regardless of the emission mechanism. Because emission towards a distant observer is beamed along the line of sight, the observer at a given time can only see an emission region with angular size γ^{-1}. Photons leaving different points within this region will reach the observer spread out over a time interval of $R/c\gamma^2$. Thus, any intrinsic variability within the emission region on timescales smaller than this will be washed out [26, 165, 120]. This is the "angular spreading" timescale, and it sets a lower limit on the allowed timescale for variability, as long as the radial width of the emission zone is greater than $R_{\rm dec}/\gamma^2$. A very narrow jet could provide an emission region of smaller size, and hence could produce variability on smaller timescales, but it would have to be very cold to prevent its internal energy from forcing it to widen. It is difficult to see how such a jet could be formed [120]. An external shock formed via interaction with a uniform medium can therefore only produce a smooth, single-peaked burst. The decay must then evolve smoothly according to the synchrotron power law cooling laws derived above.

However, episodes of brightening above the level of the general power law decay have been observed in some bursts, which cannot be explained by this model [9, 19, 128]. Angular spreading also seems to outlaw the complex, multi-peaked structure of many GRBs, since variability along the shell should be smoothed out by the time it reaches the observer. It is believed that both internal GRB structure and the refreshing of afterglow decay curves are caused by shells of ejecta catching up to and ramming into other shells of ejecta from behind. The resulting shocks are referred to as internal shocks, and I will discuss them in the next section with respect to short-term structure in the burst itself.

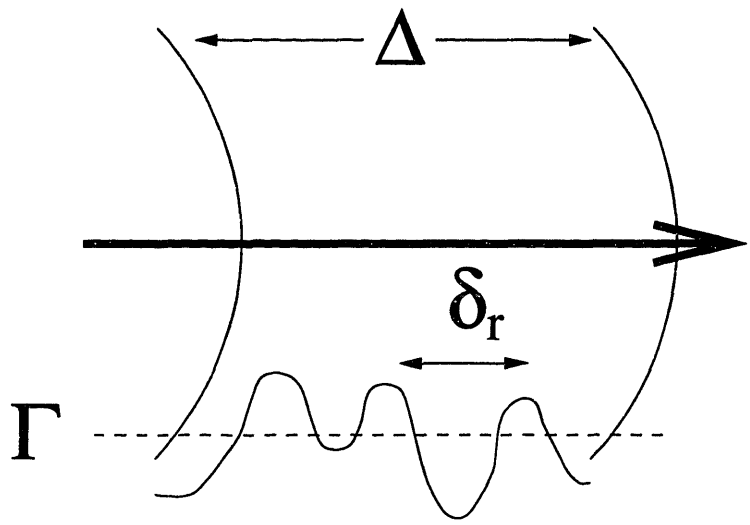

Figure 6-4 This diagram shows a shell of ejecta travelling to the right with an average bulk Lorentz factor of Γ. The shell has a width of Δ, but on shorter distance scales of δ_r, the bulk Lorentz factor fluctuates. A graph of Lorentz factor as a function of radius is superimposed on the shell, at the bottom of the figure. The average value for the Lorentz factor, Γ, is indicated by the dashed line. The faster regions will collide with the slower ones ahead of them, causing internal shocks. In the limit that $\delta_r \rightarrow \Delta$, this model approaches the external shock model.

6.4 Internal Shocks

The external shock model treats the fireball as a single shell of material expanding with a single bulk Lorentz factor that runs into a uniform external medium. The duration and time profile of the burst depend on Γ, the value of the deceleration radius (Equation 6.20), and the width of the shell. The simplicity of the model is not realistic, and despite its success in explaining the behavior of the afterglow, it is generally believed that it cannot support the complex internal structure that is present in most GRBs [96]. At least one recent paper has challenged this claim, however, so the question is not fully settled [20]. One proposed solution to this dilemma suggested that the local medium was not uniform, but rather contained small dense clouds, which would enhance the emission when the blast wave sweeps

them up [141, 132, 26]. Others argue that the data demand the existance of an erratic central engine [96, 27].

If the central engine that produces the GRB functions erratically, the fireball is better approximated by a series of shells within an overall envelope of width Δ, each shell expanding with a different bulk Lorentz factor, as shown in Figure 6-4. Faster shells will catch up with slower shells and their collisions will generate shocks. These shocks can create multiple peaks with highly diverse structure, but should lead to synchrotron radiation in the same manner as described above.

In this scenario, the duration of the burst is directly related to the duration of energy injection from the source, and the time profile is essentially determined by variations in the Lorentz factor. If the distance scale over which the local Lorentz factor varies is δ_r, and the average Lorentz factor is Γ (Fig. 6-4), then the shells will plow into each other at a radius $R_I \sim 2\Gamma^2\delta_r$ in the frame of a distant observer (Fig. 6-1). If this occurs at late times, the collision will reenergize the afterglow [127], but if it occurs early, it will create internal shocks that can produce complex structure within the burst itself at short time scales [82, 18]. The boundary between these two regimes occurs when the distance scale for the shells is the same as the overall width of the ejecta ($\delta_r \sim \Delta$), in which case the shock occurs at the deceleration radius, $R_I \sim R_{\rm dec}$. The total duration of the burst is therefore $t_{\rm dur} \sim (R_{\rm dec}/2c)\ \Gamma^{-2}$.

If the internal shocks generate the burst itself, and the external shock generates the afterglow, then the internal shocks must occur before the ejecta reaches the deceleration radius. Shocks occuring further out than that will refresh the afterglow. $R_I = 2\Gamma^2\delta_r$ must therefore be less than $R_{\rm dec}$, implying by Equation 6.20 that

$$\delta_r < 10^{11}\ {\rm cm}\ \left(\frac{E_{52}}{n_1}\right)^{1/3}\ \Gamma_{300}^{-8/3}. \tag{6.49}$$

Now, if the central engine is about the size of some compact object $R_0 \sim 10^6$ cm, with on the order of a few solar masses of material, the dynamic timescale for rapid vari-

ability is less than a millisecond. Variations in Γ on timescales of 0.1 ms correspond to $\delta_r \sim 10^6$ cm, if $\Gamma \gg 1$. This means that a compact GRB progenitor is capable of producing variations in Γ that will collide before the deceleration radius is reached by the fireball.

If the Lorentz factor at the time of ejection varies on a length scale of $\delta_r \sim 10^6$ cm, the interaction radius will be $R_I \sim 10^{11}$ $(\delta_r/10^6$ cm) Γ_{300}^2 cm. The constraint that $R_I < R_{\rm dec}$ then in turn places a limit on Γ. Let $10^6\delta_6 = \delta_r$, and use $R_{\rm dec}$ from Equation 6.20, then the average Lorentz factor must be constrained by

$$\Gamma < 3 \times 10^4 \ \delta_6^{-3/8} \ \left(\frac{E_{52}}{n_1}\right)^{1/8}. \tag{6.50}$$

We already showed in Section 6.1 that $\Gamma < 2 \times 10^4$ by requiring that the ejecta shell achieves its maximum Lorentz factor before becoming optically thin, so this condition is met for reasonable values of δ_r.

If a rapid shell catches up with a slower shell, the resulting merged shell will have a Lorentz factor somewhere between the Lorentz factors of the shells, depending on how much mass was in each shell. The final, merged, Lorentz factor will be labelled as γ_2 in the following discussion. The dynamical timescale for variability within this shock is the crossing time, which, as measured by the observer, is approximately

$$\delta t \sim \frac{\delta_r}{2c\gamma_2^2}, \tag{6.51}$$

if the shells have approximately the same Lorentz factor before the shock.

If the emission that is produced in these shocks is again synchrotron emission, then we can apply the same equations we derived in Section 6.3 to these internal shocks and derive a relation between observed energy range and burst duration. This analysis follows the derivations in [132] and [134]. We begin with Equation 6.36, cast into the observer frame:

$$\nu = \frac{3qB'}{4\pi m_e c} \ \gamma_e'^2 \ \gamma_2. \tag{6.52}$$

We multiply both sides of Equation 6.52 by Planck's constant, h, and use Equation 6.29 to eliminate B':

$$h\nu = \frac{3hq}{4\pi m_e} \sqrt{32\pi m_p n_1 \epsilon_B}\ \gamma_e'^2\ \gamma_2^2. \tag{6.53}$$

We can now use typical numbers to estimate $h\nu$:

$$\left(\frac{h\nu}{10\text{ keV}}\right) = 2.7 \times 10^{-8}\ \epsilon_B^{1/2}\ n_1^{1/2}\ \gamma_e'^2\ \gamma_{300}^2, \tag{6.54}$$

which allows us to estimate the Lorentz factor of an electron that is emitting at 10 keV in the observer frame:

$$\gamma_e' = 6 \times 10^3 \left(\frac{h\nu}{10\text{ keV}}\right)^{1/2} \epsilon_B^{-1/4}\ n_1^{-1/4}\ \gamma_{300}^{-1}. \tag{6.55}$$

The cooling timescale τ for an energetic electron is given by Equation 6.40 (set $t = \tau$), where P is the observed power from synchrotron radiation, given in Equation 6.43:

$$\tau = \frac{9\pi m_e c}{2\sigma_T \gamma_2 \gamma_e' B'^2}. \tag{6.56}$$

We use Equation 6.30 to eliminate B' and Equation 6.55 to eliminate γ_e:

$$\tau = 2 \times 10^{-2}\ n_1^{-3/4}\ \epsilon_B^{-3/4}\ \gamma_{300}^{-2} \left(\frac{h\nu}{10\text{ keV}}\right)^{-1/2}\ \text{s}. \tag{6.57}$$

This equation sets a lower limit on the width of a peak in the GRB light curve, although other processes such as the angular spreading described above may extend the width of an individual peak beyond this timescale. This equation also makes the interesting prediction that if the emission from an internal shock is dominated by synchrotron processes, then the width of the associated peak in the GRB light curve should depend on the energy of the observation band such that $\delta t \propto E^{-1/2}$.

Fenimore et al. (1995) reported such an inverse correlation in a large sample of

bright bursts (longer than 1.5 s), with a power law index of -0.4 [25], very close to the prediction. Piro et al. (1998) examined the X-ray to gamma-ray emission from GRB 960720 and found the peak widths to vary as energy to the -0.46 power [123]. It is important to note that the value of the exponent is a direct result of the fact that the characteristic synchrotron frequency depends on the square of the Lorentz factor of the emitting electrons. This dependence of τ on E enters Equation 6.56 when Equation 6.55 is used to eliminate γ_e'. The index of -0.5 thus derives from the basic physics of synchrotron radiation, and it does not depend on special assumptions about the shock conditions, nor does it distinguish between internal and external shocks.

The characteristic frequency for synchrotron emission for a relativistic shock may fall below the observable bandpass for gamma-ray or even X-ray instruments. In this case, it has been suggested that the high-energy emission could be provided by inverse Compton upscattering of UV photons off of the relativistic electrons in the shock [132, 134]. It has also been suggested that a power law distribution for γ_e is inadequate, and that a Maxwellian component will also be present in the post-shock fluid [154]. The presence of this component would cause the extrapolation of the $\nu^{1/3}$ spectrum (Equation 6.38) from high energies to be inaccurate in the X-ray regime [155]. For the purposes of this thesis, I will limit my discussion to purely synchrotron radiation from a power law post-shock distribution of Lorentz factors.

6.5 Summary

In this section I have outlined a highly simplified scenario that can explain the salient features of observed gamma-ray bursts. A large amount of high-energy radiation in a small volume undergoes a rapid expansion to relativistic speeds. When it reaches its maximum velocity all the available energy is in the bulk motion, so the fluid will be cold and will not radiate, even after its optical depth drops to unity. It coasts at this constant speed until it accumulates enough mass from the external medium to begin

decelerating. A shock will then form between the expanding shell of the fireball and the ambient medium. This shock will cause the energy of the bulk kinetic motion to be transferred into random motions of the particles in the shock, which may then radiate that energy via synchrotron radiation.

If the central engine is erratic, shells of matter will be ejected that will reach different terminal bulk Lorentz factors. These shells may collide with each other, again producing shocks that will result in synchrotron radiation. After the shock is produced, the particles will cool according to the synchrotron cooling laws, producing a piecewise powerlaw spectrum with several break frequencies. These frequencies will evolve to lower values with time, causing the observed burst/afterglow to peak at later times in longer wavelength bands.

If this scenario accurately reflects the important features of the physical processes that actually occur in the generation of a gamma-ray burst, then the typical bulk Lorentz factor of the ejecta must be $10^2 \lesssim \Gamma \lesssim 10^4$, which implies that GRBs involve some of the fastest speeds in the universe. The success of the model in predicting the spectrum of the observed afterglow, as well as the relation between peak width and observed energy, have led to this paradigm's widespread adoption over the last two years as the standard explanation for the GRB phenomenon. However, the underlying cause of the initial high-energy, high-density photon fluid remains controversial.

Chapter 7

Fourteen GRB Light Curves

The first detection of a gamma-ray burst at X-ray energies (~1–15 keV) was made in 1972 by the two proportional counters on the *OSO-7* satellite [169]. For the next 15 years, observations of GRBs at these low energies were rare, due to the lack of available wide-field X-ray instruments to catch them. Instruments on *Apollo-16* detected a GRB, also in 1972, and the 8-s integrations of the burst emission in several energy bands showed evolution from soft to hard to soft again over the burst's single peak [106, 159]. The Air Force *P78-1* satellite detected four bursts in 1979, and found that the peak X-ray emission tended to lag the peak gamma-ray emission [90]. A few other instruments captured the rare event or two. *HEAO-1*, for example, detected 21 bursts at high energies, but only two of those yielded detections at better than 2σ significance in X-rays, and one of those two came through the side walls of the detector [15].

The *Ginga* satellite was equipped with co-aligned wide-field detectors to cover the energy range from 2–400 keV [110]. During its operation between 1987 and 1991, it detected $\sim$ 120 GRBs [117]. Twenty-two of these were strong enough to yield useful spectral data and were believed to have entered the detector from the forward direction [152]. These GRBs confirmed that a spectral softening was common in the tails of bursts, and that X-ray flux can comprise a large fraction of the energy

emitted from a GRB [152]. The mean ratic of X-ray fluence to gamma-ray fluence in these 22 bursts was $\sim$ 24%, but could sometimes exceed unity, as also found in BATSE data [124]. X-ray precursors were observed in a few cases [111]. Between 1989 and 1994, the GRANAT/WATCH all-sky monitor detected 95 bursts in two energy bands, 8–20 keV and 20–60 keV, and found 13 of them to exhibit significant emission in the lower energy band before or after (or both!) the activity in the higher energy band [136].

The Wide-Field Camera on *BeppoSAX* has detected 24 GRBs between 1.5–26.1 keV to date [50]. Their first detection was GRB 960720, a singly-peaked GRB that showed clear spectral softening, such that the width of the peak fell with the energy band to the power of -0.46 [123]. As explained in the last section, the synchrotron cooling timescale is expected to follow an $E^{-1/2}$ power-law (Equation 6.57), so this result was immediately linked to synchrotron emission [123]. Only one of those 24 bursts (GRB 980519) exhibits significant pre-burst activity, and in't Zand et al. (1999) make the tentative suggestion that the GRB event may be the result of internal shocks superposed upon the ongoing process of an external shock that began earlier [74]. Late X-ray activity in the light curve for GRB 970228 was also suggested to result from the same external shock process that powered the later afterglow [17, 41].

The general picture that has emerged, therefore, is that although X-ray lightcurves for GRBs tend to track with their gamma-ray counterparts, there is great diversity in form. Spectral evolution may or may not be present. This spectral evolution sometimes takes the form of a soft-to-hard evolution in the rise of the burst, and sometimes takes the form of a hard-to-soft evolution in the decay of the burst. Sometimes both forms of evolution are present. In general, the times of X-ray peak emission tend to lag behind the peaks at higher energies, but not always. Bursts tend to last longer as seen in X-rays, but not always. A small fraction of bursts exhibit X-ray activity with no detectable emission at gamma-ray energies. This activity sometimes precedes the GRB and sometimes follows it. In very rare cases, it does both. Since the synchrotron

shock model has been successful in explaining many features of the afterglow, and the observed spectra are continuous from X-ray to gamma-rays, the variability observed in the X-ray lightcurves is usually interpreted as the low-energy tail of the synchrotron emission from internal shocks, as described in Section 6.4 of this work.

In this chapter I present the light curves for the GRBs detected by the ASM and interpret them in the context of the synchrotron shock model. I include each of the thirteen GRBs described in Chapter 5, as well as GRB 961216, which was detected by the ASM, but could not be localized accurately. Eight of these events were observed by either BATSE or the *BeppoSAX* GRB Monitor, so in those cases the count rates at higher energies are available for comparison with the ASM results. Section 7.1 describes the data presented in this chapter and the analysis techniques used to process them. Section 7.2 presents the observations and the GRB light curves. Section 7.3 summarizes the common features and striking differences among these light curves.

7.1 Data

As described in Section 3.3.2, the ASM records the total number of good events detected from all sources in the field of view (FOV) of each SSC in 1/8-s bins and three energy channels. These channels are named A, B, and C, and they span the nominal energy ranges 1.5–3, 3–5, and 5–12 keV, respectively. The sum of the counts in these three bands is referred to as the "sum band", or "S".

In order to extract the light curve of the GRB from the time-series (MTS) data, we use information provided by the position histogram data (See Section 3.3.1). If we assume that the GRB is the only variable source during a given observation, the constant background rate (i.e. the count rate in the MTS data caused by everything else but the GRB) is set by subtracting the number of counts detected from the GRB (as determined from the fit to the position-histogram data) from the number

of counts detected in the MTS data during the entire 90-s dwell. Any counts above this background rate in a given MTS time bin are attributed to the GRB (Eq. 3.2).

The figures in this chapter present the ASM time-series data in one of two ways: either as the raw data showing the total number of counts detected in each time-series bin, with a broken line to indicate the estimated background level, or as the background-subtracted flux histories that result from the application of Equation 3.2. In the latter case, the uncertainty in the flux measurement is also displayed. The derivation of these error bars is described in section 7.2.3.

Where possible, the ASM light curves are compared with the BATSE or *BeppoSAX* GRBM count rates during the same event. The BATSE count rates shown here are recorded in four energy channels. The rough energy ranges of these channels are 25–60, 60–110, 110–320, and $>$ 320 keV. BATSE records counts in 64, 256, and 1024 ms bins until the on-board software recognizes a trigger event (when the number of counts in a single bin is a significant excess above the running average). Then the binsize is reduced to 0.016 s for 242 s, and an alert with a rough position is telemetered to Earth immediately. The counts recorded at high resolution are saved on-board the spacecraft and sent down at the next convenient time [103]. When the *BeppoSAX* GRBM registers a burst, the 40–700 keV count rate is stored in 0.48 ms bins from 8 s before to 98 s after the trigger time; all on-board data is sent down once every $\sim$ 90-m orbit for operators to examine manually [40, 28].

7.2 The Observations

7.2.1 Archival GRB Events

The multiply-peaked structure of GRB 960416 was observed in both SSCs 1 and 2 during a single dwell, and the raw count rates in each energy band are shown in Figure 7-1 in 2-s bins. The background estimates are in good agreement with the lowest observed count rates, which implies there are intervals when no emission is detected

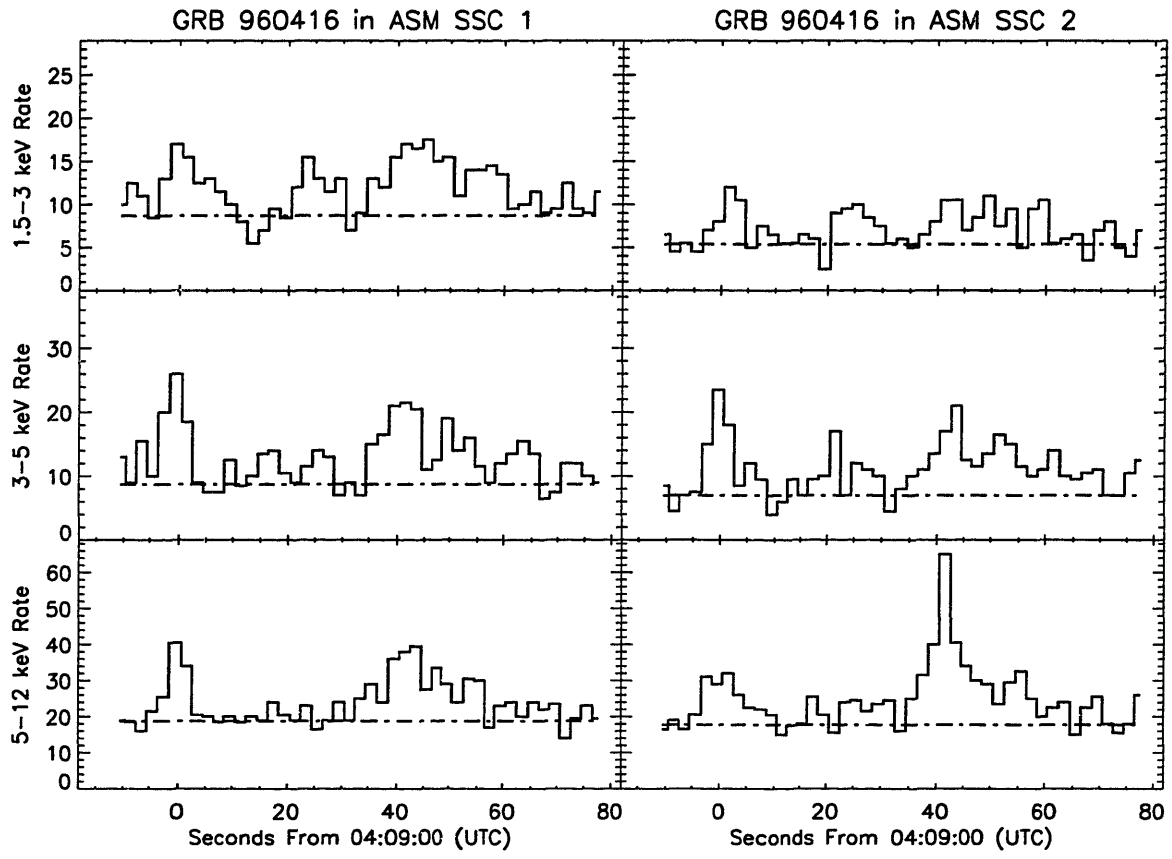

Figure 7-1 The time-series data in 2-s bins for observations of GRB 960416 in both SSC 1 and SSC 2. Broken lines estimate the contributions from all other sources in the FOV (Table A-2).

from the GRB. The burst intensity clearly increases at higher energies, although the brightest peak seen by SSC 2 has no counterpart in SSC 1. This is more likely a result of counting statistics than a physical difference in the detector response to a rising spectrum.

This burst was also observed by BATSE, and the BATSE count rate during this event is shown in Figure 7-2, compared with the ASM flux light curve derived from averaging the data from both SSCs. The BATSE data show a double-peaked structure lasting some 50 s. The ASM data show a clearly similar shape for the light curve, but with some significant differences. Most striking is an apparent extra peak in the X-ray light curve that is absent in the gamma-ray light curve. This peak is detected by both

ASM SSCs (Fig. 7-1), but its spectrum is remarkably soft. There is no significant emission detected above 5 keV during this event. If this is synchrotron radiation, Equation 6.34 suggests that the average bulk Lorentz factor for this interaction is less than about 20. Such a small Lorentz factor would imply a very small interaction radius for an internal shock, and the fireball would most likely still be opaque. It may be the result of a reverse shock, if the first peak is the result of a forward shock, but the 30 s delay is problematic. With the limited data available via the three ASM spectral channels it is impossible to convincingly support any particular scenario. The origin of this emission remains a mystery.

It is a prediction of the synchrotron shock model for GRBs that emission peaks should last longer at lower energies (Equation 6.57), and the peak at $t = 40$ s is clearly longer in the ASM data than in the BATSE data. The ASM light curve for this peak also decays more slowly than its BATSE counterpart, and there is a difference of a few seconds between the times of peak count rate in each instrument. The spectrum of the event seems to be softening rapidly within the peak itself.

The first peak is also much wider as seen by the ASM than by BATSE, although both peaks seem to reach their maxima at the same time (although the limited temporal resolution of the ASM could mask a delay of up to a second or two).

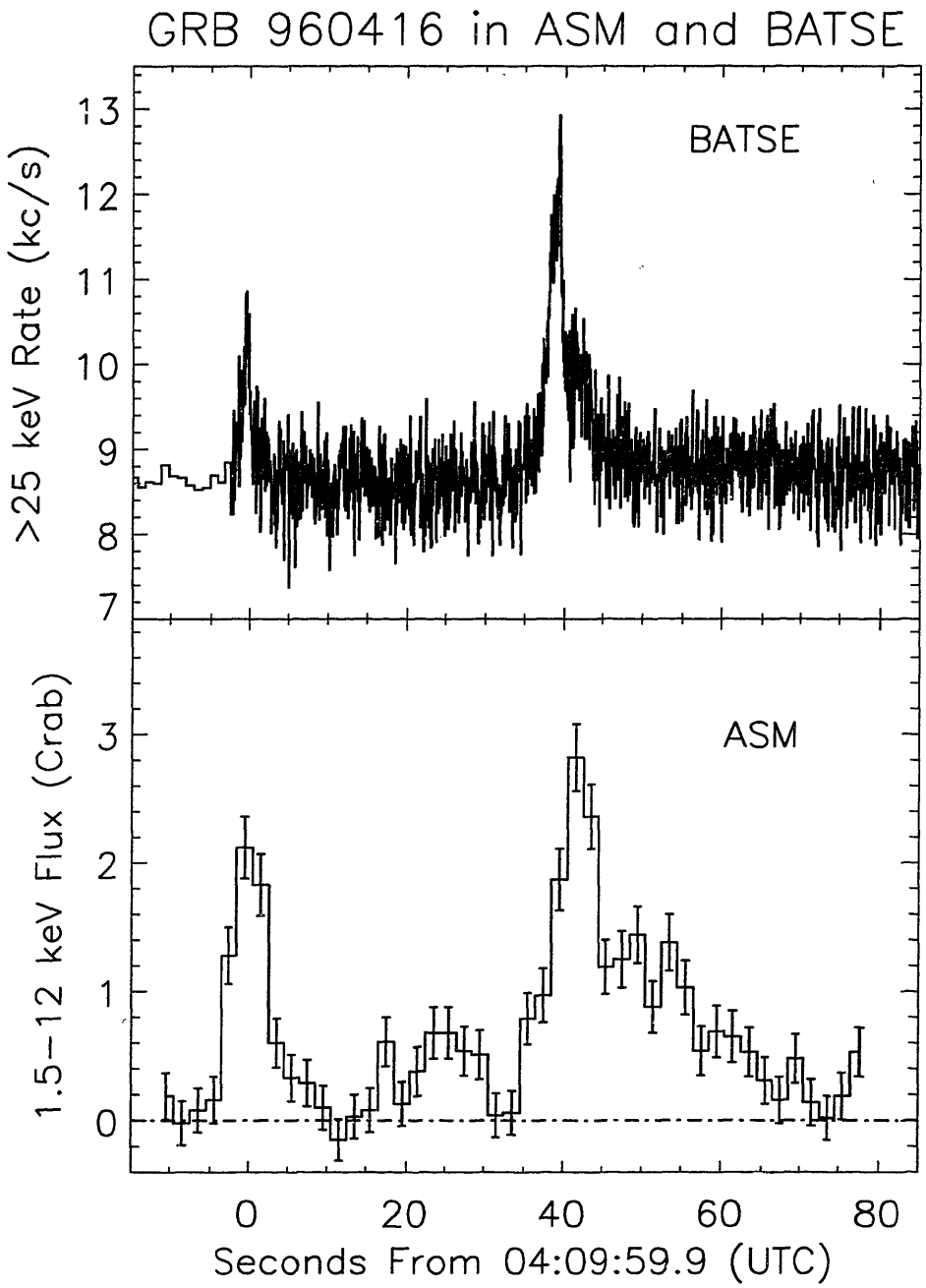

Figure 7-2 The time-series data for GRB 960416 in both the ASM (2-s bins; 1.5–12 keV) and BATSE (> 25 keV).

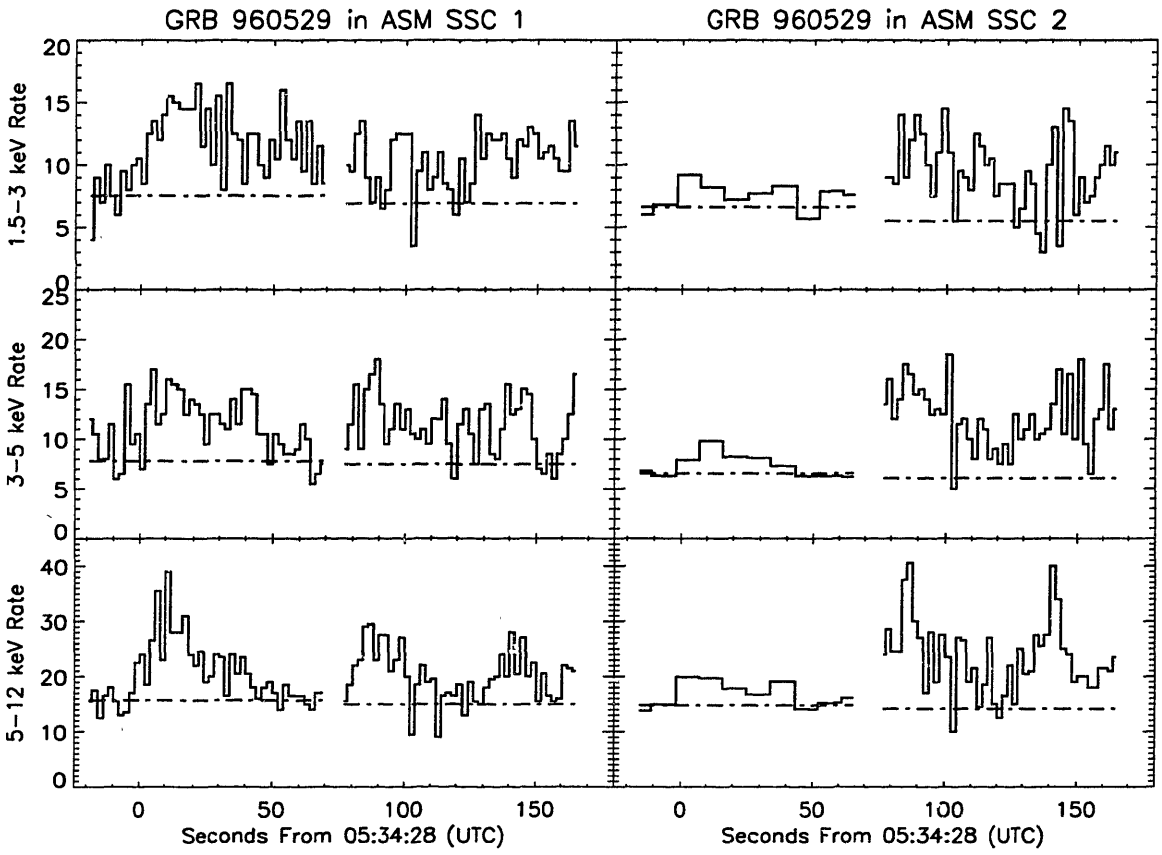

Figure 7-3 The time-series data in 2-s and 9-s bins for the two observations of GRB 960529 in both SSC 1 and SSC 2. Broken lines estimate the contributions from all other sources in the FOV (Table A-3).

GRB Candidate 960529 may not be a GRB at all. Beginning around 05:34 UT, three hard peaks were observed in the ASM time-series data from two SSCs over the course of two successive dwells (Fig. 7-3). A new source was detected in all four observations, all four error boxes overlapped at a consistent location (Section 5.1.2), and the intensity measurements in each SSC were mutually consistent. This source lies 21° north of the galactic plane, and no known X-ray sources lie near the ASM localization. Although BATSE did not detect this event, the KONUS experiment on the *WIND* satellite confirmed observing a triply-peaked event lasting approximately 200 s at this time (P. Butterworth, private communication).

However, the KONUS data also indicate that this event yielded no significant

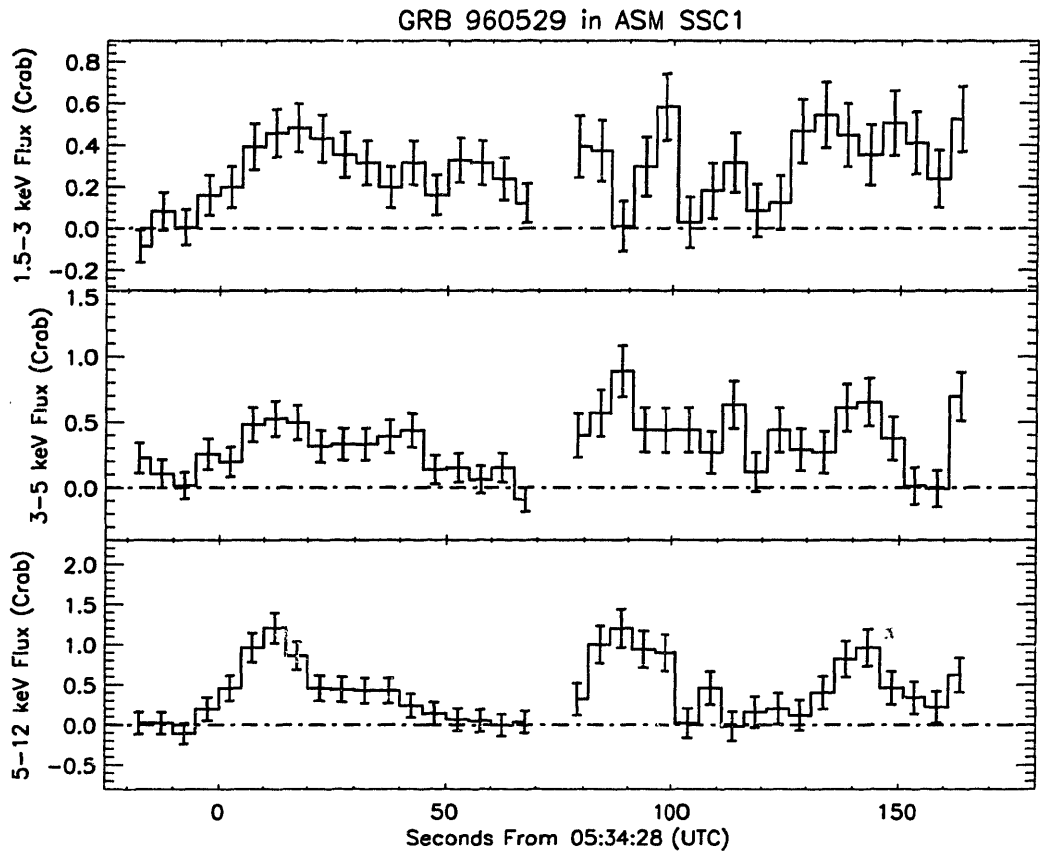

Figure 7-4 The time-series data for ASM observations of GRB Candidate 960529 in 5 s bins and three energy channels, background-subtracted and converted to flux units by comparison with the Crab flux. A gap indicates the 6 s interval between dwells when the ASM assembly was in motion.

emission above 50 keV, which is very soft for a GRB. If a GRB-type synchrotron shock model can be applied to this event, Equation 6.34 implies that the bulk Lorentz factor of the shocks must then lie below ~ 40. Equation 6.7 could then imply that the timescale for variability must be longer than 25 ms, but only if the radiation is non-thermal, which is unknown in this case. This prediction could be checked against the KONUS data. This event may be a very weak GRB or a quite different phenomenon. X-ray bursts have sometimes been known to show multi-peaked structure, but they typically have thermal temperatures of 1 or 2 keV, and would most likely not extend to the KONUS energy range [95].

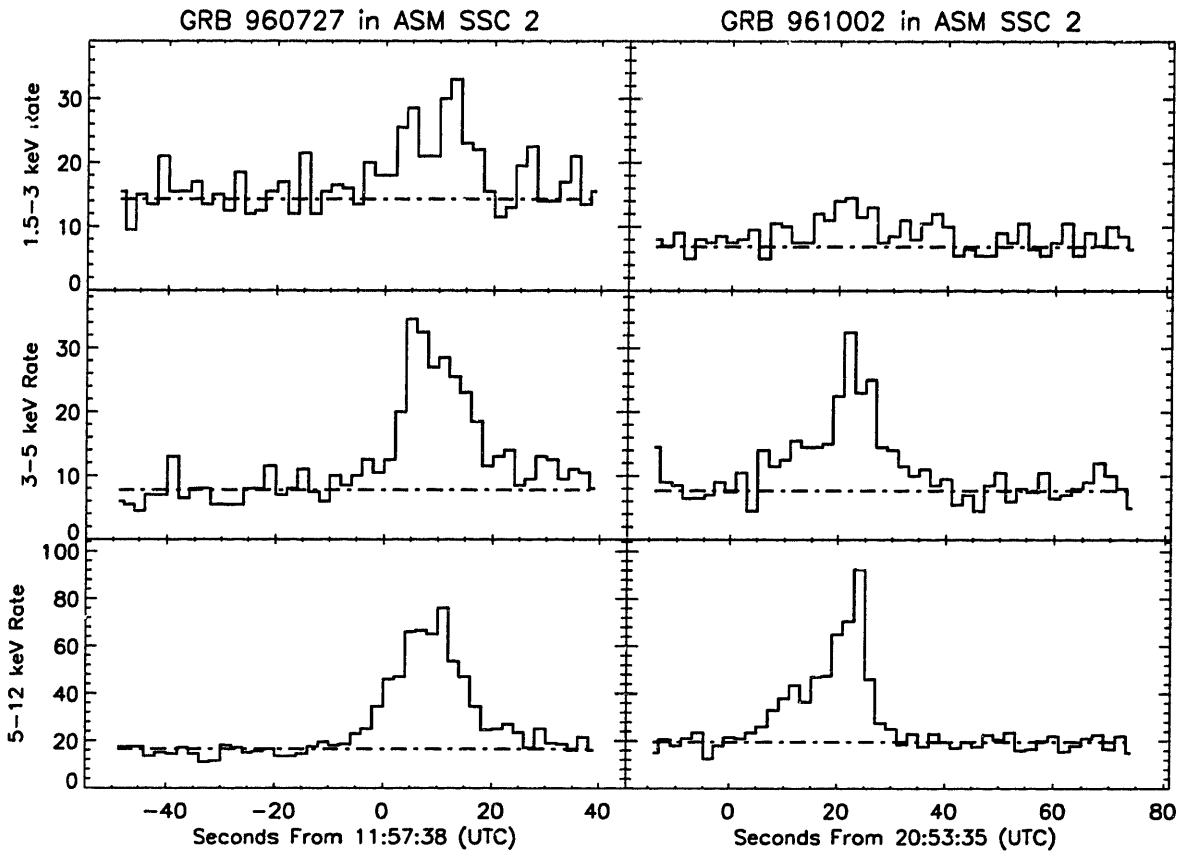

Figure 7-5 The time-series data in 2-s bins for the ASM observations of both GRB 960727 and 961002 in SSC 2. Broken lines estimate the contributions from all other sources in the FOV (Tables A-4 and A-5).

GRB 960727 and GRB 961002 were very similar. They were each detected only in SSC 2, they each lasted about 30 s, and they each showed a singly-peaked light curve without any significant structure on smaller time scales. Neither burst was detected by BATSE, but each was detected by KONUS and the GRB detector on *Ulysses* (Section 5.1.2). GRB 960727 reached a peak flux (2-s bins; 1.5–12 keV) of 6.0 ± 0.5 Crab, while GRB 961002 peaked at 6.8 ± 0.6 Crab. Both events seem to end in a weak extended tail that lasts for 10 or 20 s (Fig. 7-6). Although the significance of this tail is only between 1 and 2 σ, there seems to be a post-burst excess when compared to the scatter of the pre-burst count rate (and after $t = 40$ s

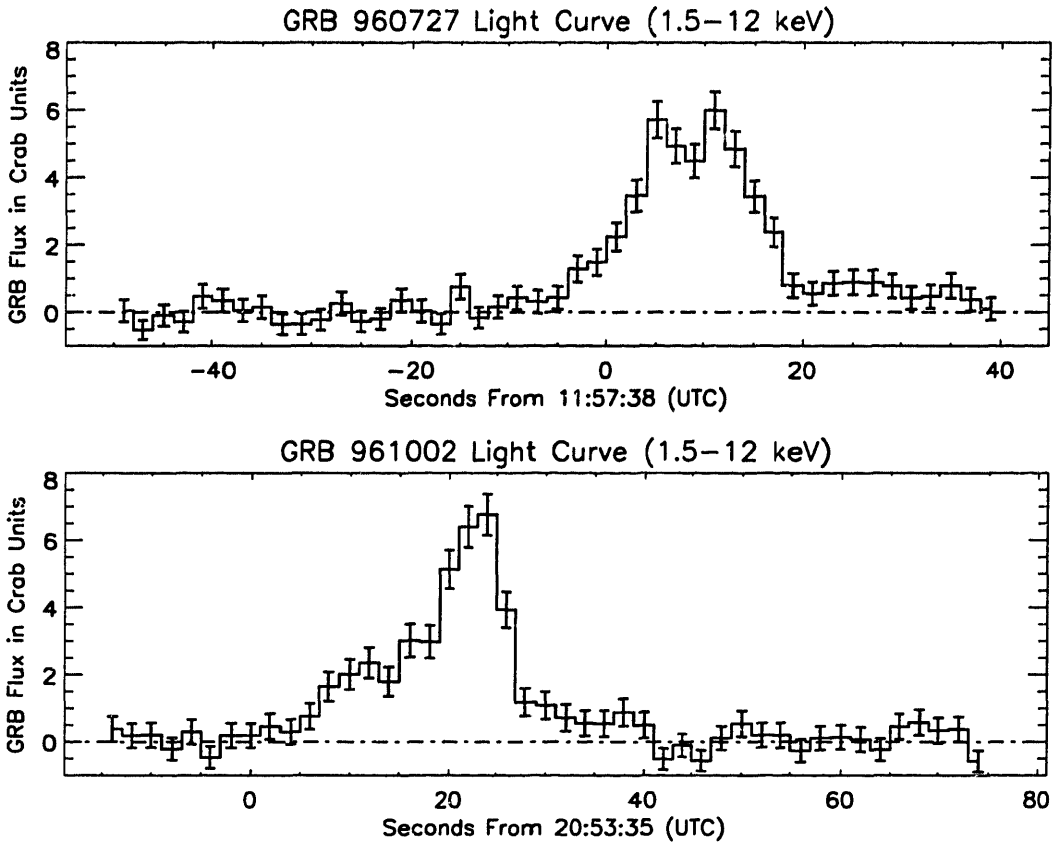

Figure 7-6 The time-series data for GRBs 960727 and 961002 (2-s bins) in Crab Flux Units (1.5-12 keV).

for GRB 961002) around zero. The accuracy of the background estimation before the burst lends credence to the existence of a post-burst excess.

Neither burst showed any features that can be easily interpreted within a simple fireball scenario. There is no obvious soft lag or spectral softening; the extended tail is too weak in the three sub-bands to make a statistically signficant measurement of different decay rates.

GRB 961019 was detected in a single observation of SSC 2, and it was also observed with BATSE. The BATSE light curve shows three sub-peaks, which may consist of two smaller bursts superimposed on a fast-rise/exponential-decay envelope. The GRB was off-axis in the ASM SSC by a large ϕ angle of $-4°.5 \pm 0.2$. This implies a transmission

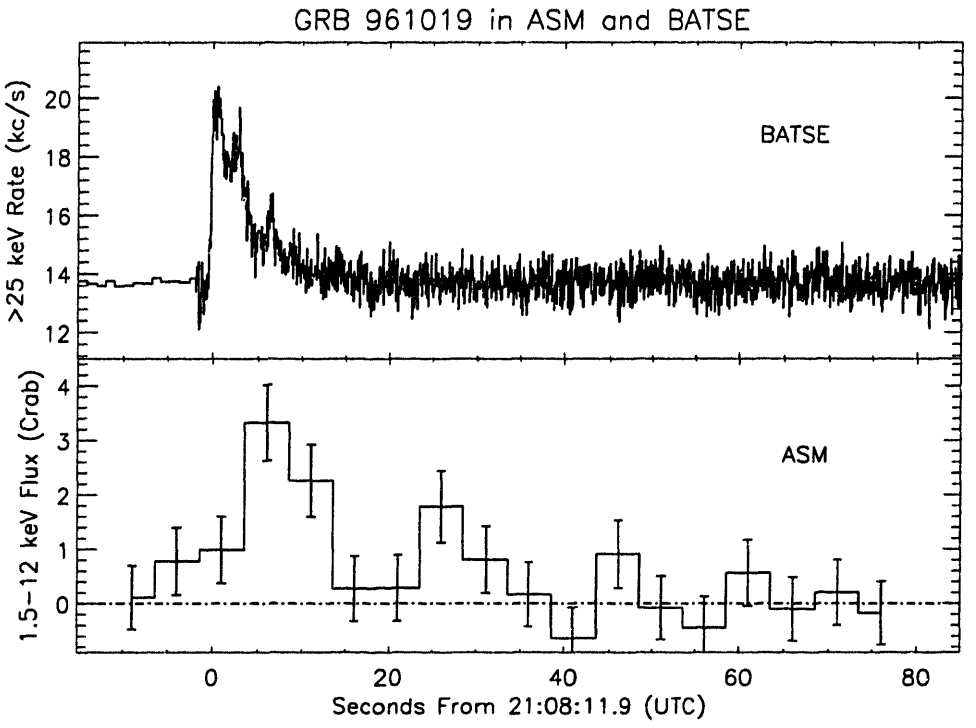

Figure 7-7 The time-series data for GRB 961019 in both the ASM (5-s bins; 1.5–12 keV) and BATSE (> 25 keV).

fraction of only 23.7%. Even when binned into 5-s bins, as shown in Figure 7-7, the light curve is ratty with large errors, despite reaching a peak flux of over 3 Crab (1.5–12 keV).

There is clearly a significant delay between the times of peak emission as measured by BATSE and as measured by the ASM. Although the weak ASM signal renders the delay difficult to measure, it seems to be on the order of $5 - 10$ s, a relatively large offset when compared to other bursts in this sample. It is also possible that the X-ray peak corresponds to spectral softening over the sub-peaks of the GRB, but the poor statistics render it impossible to distinguish between these two scenarios. Although it is tempting to the eye to see the high points in the ASM light curve at 27, 47, and 62 s as candidates for secondary peaks, like those seen in GRB 960416, none of them are statistically significant.

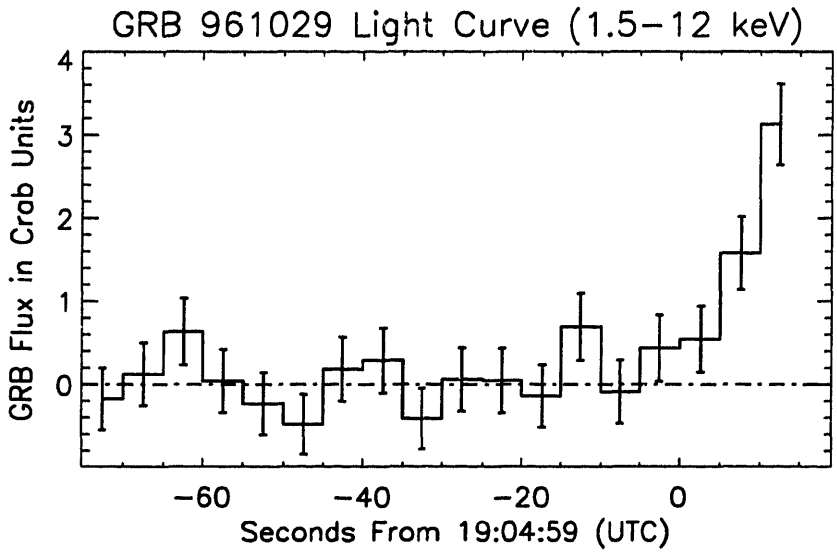

Figure 7-8 The time-series data for GRBs 961029 (5-s bins) in Crab Flux Units (1.5–12 keV).

GRB 961029 was a great disappointment. The count rate began a dramatic rise, but only a few seconds from the end of a dwell, and the FOV location of the source was such that it was only $2°.00 \pm 0.23$ (Table 5-2) from the edge of a single SSC (SSC 2). As the ASM rotated to begin its next dwell, the signal was lost before a maximum was reached. At the last measurement, the burst flux (1.5–12 keV) was 3 Crab and rising (Fig. 7-8). The 30% transmission function renders it impossible to measure structure within the burst light curve. We can be sure this is a GRB because KONUS reported a burst detection at 19:05:10 (UTC), exactly during the rise of the ASM event. Unfortunately, neither BATSE nor the *Ulysses* detector observed this GRB, so no other data are available for comparison.

The single ASM observation (SSC 2) of GRB 961216 suffered to an even greater degree than that of GRB 961029. The FOV location of GRB 961216 lay closer to the edge of the FOV than 1.4°, which is outside the region for which our position-determining ability is well-calibrated (Section 4.2). Without an accurate position, it is impossible to apply Equation 3.2 and derive a light curve. Figure 7-9 shows the

count rate as detected by the entire SSC in the time-series data, without background subtraction. The light curve is hard to interpret, as the transmission function is less than ~20%, but it seems to both lead and trail the gamma-ray activity as measured by BATSE.

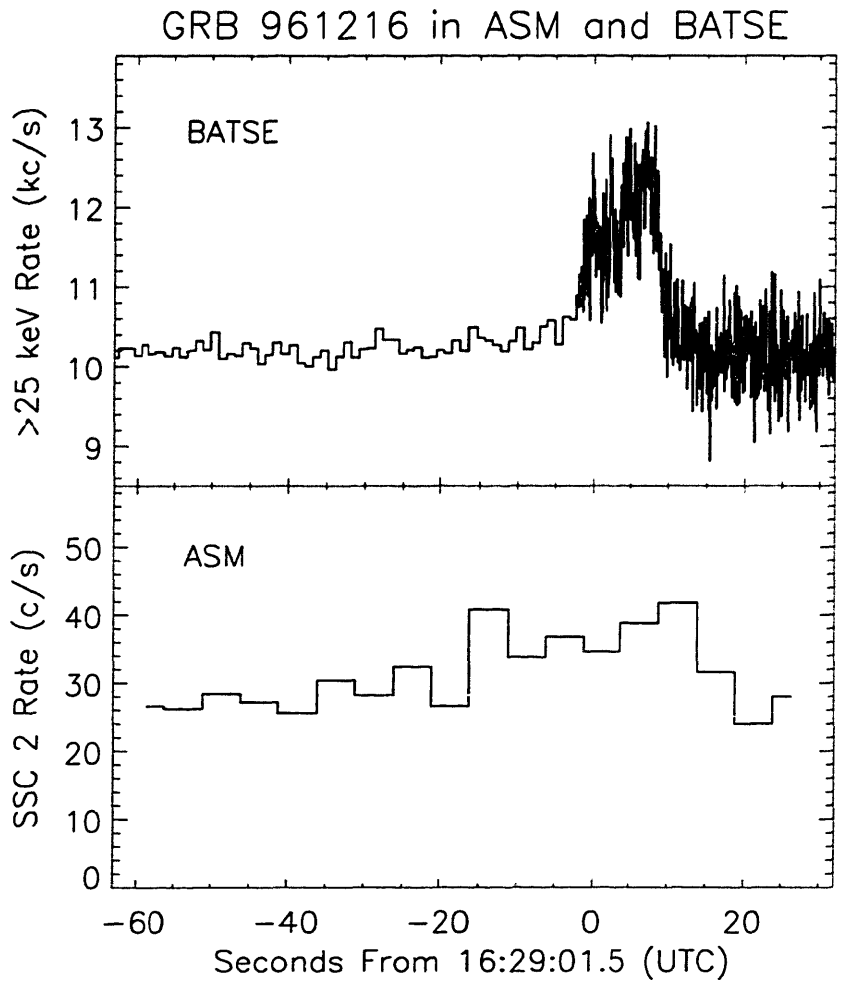

Figure 7-9 The time-series data for GRB 961216 in both the ASM (5-s bins; 1.5–12 keV) and BATSE (> 25 keV). No background subtraction has been performed on the ASM data.

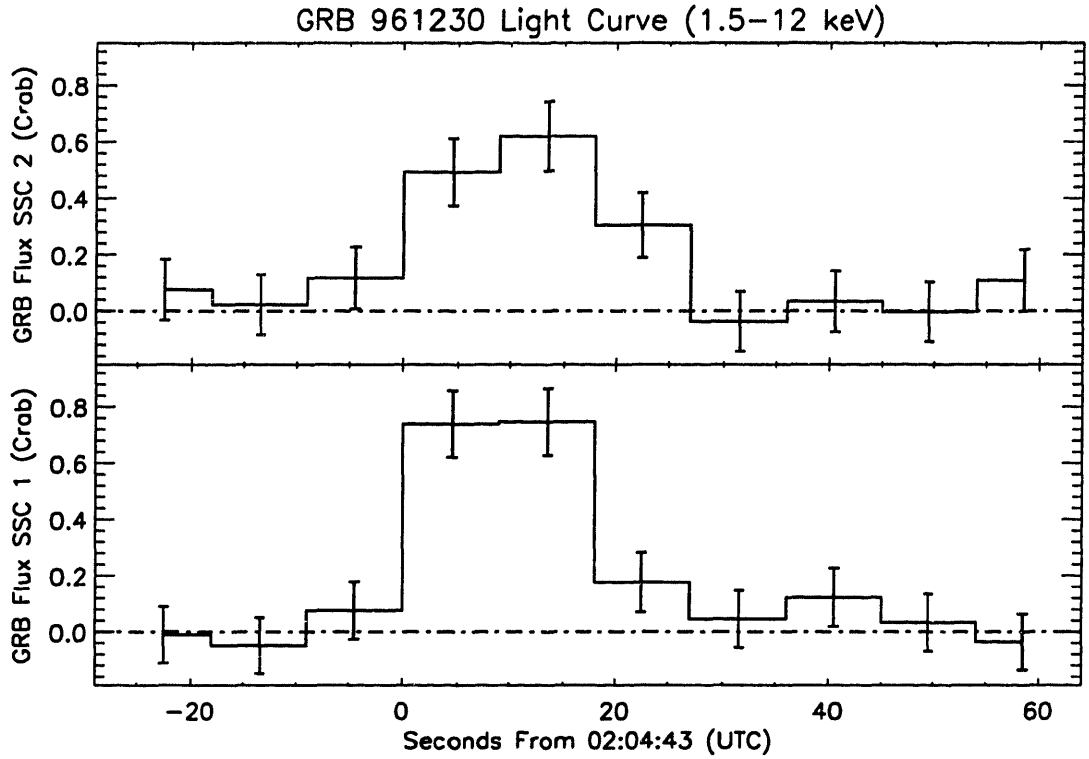

Figure 7-10 The time-series data for GRB 961230 (9-s bins) in Crab Flux Units (1.5–12 keV).

GRB 961230 was a weak burst that was nonetheless detected in both SSC 1 and SSC 2 during the same dwell. Figure 7-10 shows the light curve in 9-s bins as measured by each SSC. The GRB lasted about 25 s and reached a peak flux of 0.69 ± 0.08 Crab (The average of the measurement in each SSC). This burst was detected by the GRB detector on *Ulysses* at 02:04:52 (UTC), but by no other instrument. The *Ulysses* trigger time was consistent with the peak of the burst emission as measured by the ASM, but the temporal resolution of the ASM light curve is too coarse to derive an IPN-style position triangulation for the source. One might try to derive a time-delay by cross-correlating the light curves, but the radical differences between GRB light curve structure in different energy bands render such an action highly unlikely to result in a trustworthy answer.

7.2.2 GRBs Identified in Real-Time

We began looking for GRBs in the real-time ASM data stream in the Summer of 1997. The first detection occurred on August 15, shortly after we received an alert from BATSE over the GCN. We noticed strong, reliable detections of new source candidates in multiple SSCs over two dwells, with rapid variability in the corresponding time-series data. We were able to report a position to the scientific community within 12 h of the BATSE trigger time [144].

The burst lasted several minutes, with a multiply-peaked structure on smaller time scales. The total count rates in 1-s bins as observed by SSCs 1 and 2 in the three energy channels over the course of the three dwells during which this event was observed are graphed in Figure 7-11. Evidently SSC 2 scanned onto the source during the decay from an initial peak. For the first 90 s, the burst was only in the field of view of SSC 2. The time-series data show a falling count rate with a hard spectrum for the first 25-s of the dwell. A second peak began 40 s later, lasting until the end of the dwell. After the 6-s rotation interval, the GRB was in the FOV of both SSC 1 and SSC 2, and a large burst of emission was seen in both cameras. At the end of the second dwell, the burst was in rapid decline. Although the burst was still in the FOV of SSC 1 in the third dwell, its FOV location was at a ϕ angle of $-5°.2$, implying a transmission function of 15.8%. Although the position histogram analysis indicates an average flux of 30 ± 20 mCrab (1.5–12 keV) from this position during this 90-s dwell, this is not enough flux at that location to derive any temporal structure from the time-series data on smaller time-scales.

Figure 7-11 is complicated to interpret, since each 90-s interval contains counts from different sources, and GRB 970815 is detected in different cameras in different FOV locations. Figure 7-12 reconstructs the light curve of the GRB in the three energy channels over the interval during which it was observed by the ASM (the three lowermost panels). Here the triple-peaked structure of the burst is much clearer, although there is very little that can be said about the character of the first peak.

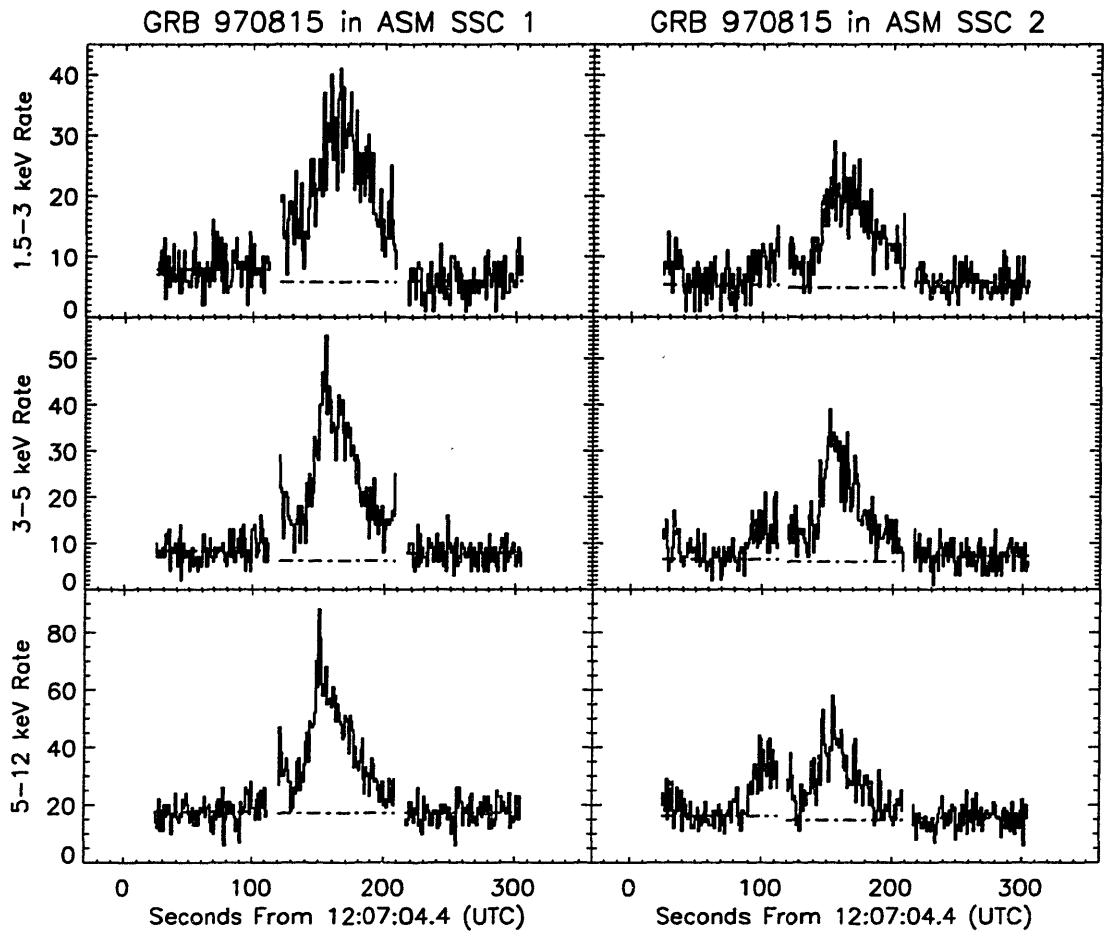

Figure 7-11 The time-series data in 1-s bins for the three observations of GRB 970815 in both SSC 1 and SSC 2. Gaps indicate the 6 s intervals between dwells when the ASM assembly was in motion. Broken lines estimate the contributions from all other sources in the FOV (Table A-9). The GRB was not in the FOV of SSC 1 during the first dwell, nor was it in the FOV of SSC 2 during the third dwell.

It is striking that the spectrum of the third peak is noticably softer than that of the second. The peak flux of the third peak is twice that of the second in the 1.5–3 keV band, but both fluxes are equal in the 5–12 keV band.

The difference in spectrum between the second and third peak becomes pronounced when one compares the ASM light curve with the BATSE counting rates during this event, as in the top three panels of Figure 7-12. Here, we see clearly the first peak of which the ASM only caught the decay tail. Although we cannot determine the relative strengths of these two peaks as seen by each instrument, we note that the decay time-scale seems much longer in the ASM light curve, indicative of the spectral softening that has been observed in the decay tails of many bursts. This spectral softening is present in the second peak, as well.

Most striking, however, is that the third peak, strongest in the ASM light curve, barely registers in the BATSE count rate. There is a slight bump in the BATSE rate, but only in the softest energy channel (25–50 keV). The spectrum of the burst seems to be evolving rapidly during this peak: Figure 7-12 shows a distinct soft lag between the times of peak burst flux between the three energy channels of the ASM, which does not seem to be the case in the other peaks.

An intriguing possibility is that the third peak is an external shock, and hence represents the beginning of the afterglow, while the first two peaks originate in internal shocks that occur before the outermost ejecta reach the deceleration radius and the external shock begins. The soft lag would in that case be the beginning of the decay of ν_m as shown in Equation 6.32. The observed delay of 13 s between the times of peak emission in the C band ($E \sim 7$ keV) and the A band ($E \sim 2.25$ keV) would imply that the shock began at $t_0 \sim 140$ s, which is consistent with the onset of the third peak.

If we use t_0 as an origin, the decay curve of the third peak can be fit with a power-law model, such that $F(t) \propto t^{-\alpha}$. All three ASM energy bands show a decay from the third peak consistent with $\alpha = 1.5$. There is no evidence for a softening in the decay,

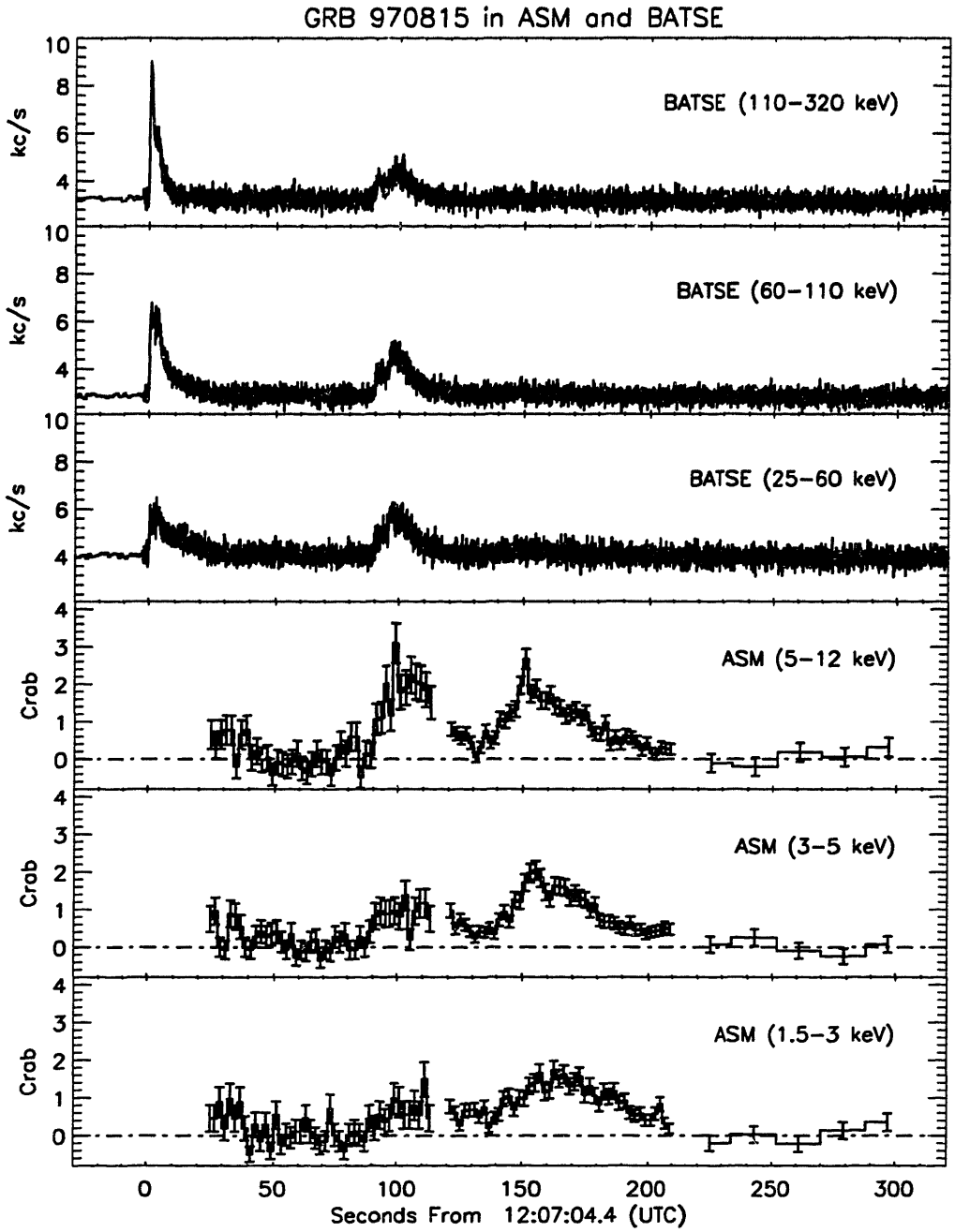

Figure 7-12 Light curves for GRB 970815 as measured by both the ASM and BATSE. The ASM scanned onto the GRB location during the decay of the first peak. Gaps in the ASM light curve indicate the 6 s intervals between dwells when the ASM assembly was in motion. The first two dwells are graphed in 2-s bins. The GRB is very dim during the third dwell, and although the data from the third dwell have been binned into 9-s bins, the flux in each bin is consistent with zero.

which is in marked contrast to the decay from GRB 970828, as described below, but consistent with the afterglow observations from other GRBs and the predictions of the external shock model (Section 6.2). X-ray afterglow curves have been measured from 22 GRBs to date, and the power-law indices for the decay range from 1.1 for GRB 970508 [122] to 1.57 for GRB 970402 [116]. The decay from GRB 970815 is thus fully consistent with an afterglow-type decay. If one extrapolates this decay to the time of the ASCA follow-up observation, $\sim 3.5 \times 10^5$ s after t_0, the predicted 2–10 keV flux is about 8×10^{-14} ergs cm^{-2} s^{-1}, below the ASCA upper limit of 10^{-13} ergs cm^{-2} s^{-1} [113]. The lack of an ASCA detection does not rule out the possibility that the third peak is the start of an afterglow decay.

However, a problem with this scenario is the long time delay between the arrival of the first and third peaks. All photons emitted prior to the shell's reaching the deceleration radius will arrive at the observer within ~ 10 s (Eq. 6.21). A 140 s interval, as measured by the arrival of photons at the observer's location, will correspond to $\sim 10^7$ s of relativistic flow as measured in the observer's rest frame. The lack of emission above 25 keV implies by Equation 6.34 that $\gamma_2 \lesssim 30$, but Equation 6.18 implies that after this time span, γ_2 will only be about $\eta/3$, constraining η to be about 100, which is at the lower edge of allowed values for η by Equation 6.7. While perhaps not impossible, it seems unlikely that the ejecta is moving slow enough to allow the burst to last 140 s as measured at the observer location, while still moving fast enough to emit 100 keV radiation.

Perhaps the most likely scenario is that both the second and third peaks result from shells catching up with the decelerating shell that produced the first shock. By 140 s, the shell that produced the first peak would have moved well past the deceleration radius (Eq. 6.19). The two later shells would shock this decelerating fluid and produce emission enhancements as observed. The second and third peaks would in this scenario be early versions of the enhancements seen late in the afterglow of other bursts, such as GRB 970508 [122], indicating that whatever processes produce

bursts continue to operate throughout the entire event. In this scenario, any emission from the deceleration of the shell that produced the first peak would have to be too dim for the ASM to detect. If this scenario is true, the afterglow and the burst cannot always be considered distinct events. It is possible, however, that the late pulses in the afterglow are not due to collisions from behind, as interpreted by [122], but instead are isolated instances of the remnant colliding with a dense patch of external medium.

The radiation from GRB 970828 arrived at Earth in the middle of the day on the Eastern coast of the United States, so the ASM team was able to respond quickly to evidence for a new GRB localization. In fact, two of us were proceeding through the analysis independently. Ron Remillard noticed that the ASM position histogram analysis had reported two strong detections of a new X-ray source, while I had received a BATSE position alert that showed a GRB localization coincident with the ASM FOV at the time of trigger. We jointly released an arcminute localization of this GRB to the community within two hours of the event [129].

As with GRB 970815, the sequence of observations of GRB 970828 is complex. The total ASM count rates during the GRB event are plotted for both SSCs 1 and 2 in Figure 7-13. The burst erupted mid-way through a 90-s dwell. Its FOV location was such that it was only observed by SSC 1. An ASM rotation shifted the GRB's FOV location such that it lay very close to the corner where the two SSCs' FOVs intersect; just 0°.5 inside the edge of the FOV of SSC 2. A second rotation brought the source to the center of the FOV of SSC 2, in time to witness the final decay of the event.

Despite the extremely low transmission factor for the GRB flux during the second dwell, the counting rate in SSC 2 as shown in Figure 7-13 appears to lie above the background level for at least part of the second dwell. When the background is subtracted and the data binned into 9-s bins, there is a clear detection of the GRB in at least two of the three energy channels. Figure 7-14 shows a composite light curve for this GRB in Crab flux units. The burst appears consistent with a single event

that lasts almost four minutes, although poor statistics may mask structure during the second dwell. There is an indication that the time of peak emission lags at lower energies, but the poor statistics during the peak mask this feature. The spectral softening during the final decay is apparent.

A comparison between the ASM light curve for GRB 970828 and the corresponding BATSE count rates, as shown in Figure 7-15, reveals a stunning difference in burst morphology. BATSE observed a very complex burst, with sharp peaks on short timescales after an initial, bright, 40-s event. The burst is completely over by 150 s after the trigger. For the ASM, on the other hand, this burst showed a single-peaked structure that lasted over 200 s. The X-ray flux climbs more slowly than the gamma-ray flux, and there may even be a few seconds lag at the beginning. Unfortunately, the interval when BATSE observed the most temporal structure in this burst corresponded to the second ASM dwell in this sequence, so it is impossible to tell if the gamma-ray structure is echoed at lower energies, or if it is entirely washed out. Certainly the structure in the first BATSE peak does not show parallel structure in the ASM light curve.

The long, smooth character of the X-ray light curve suggests that perhaps here the interaction radius for the internal shocks is the same as the deceleration radius. In this interpretation, the short bursts in the BATSE data originate in internal shocks superimposed on the longer process of an external shock. A power law decay curve, when fit to the sum band data in the last ASM dwell, indicates that the flux decays as roughly t^{-5}. All observed afterglow decay curves have indices around between 1.1 and 1.5, and the X-ray decay from this very GRB was measured by the PCA and ASCA over the following two days to decay as $t^{-1.4}$! [114]). There is nothing in the theory of external shocks to explain a decay index around 5 that later changes to 1.4. It is more likely that the burst resulted from the superposition of internal shocks, and the X-ray flux from one shock did not have time to decay before it was shocked again. The afterglow emission would then be from a separate, external shock.

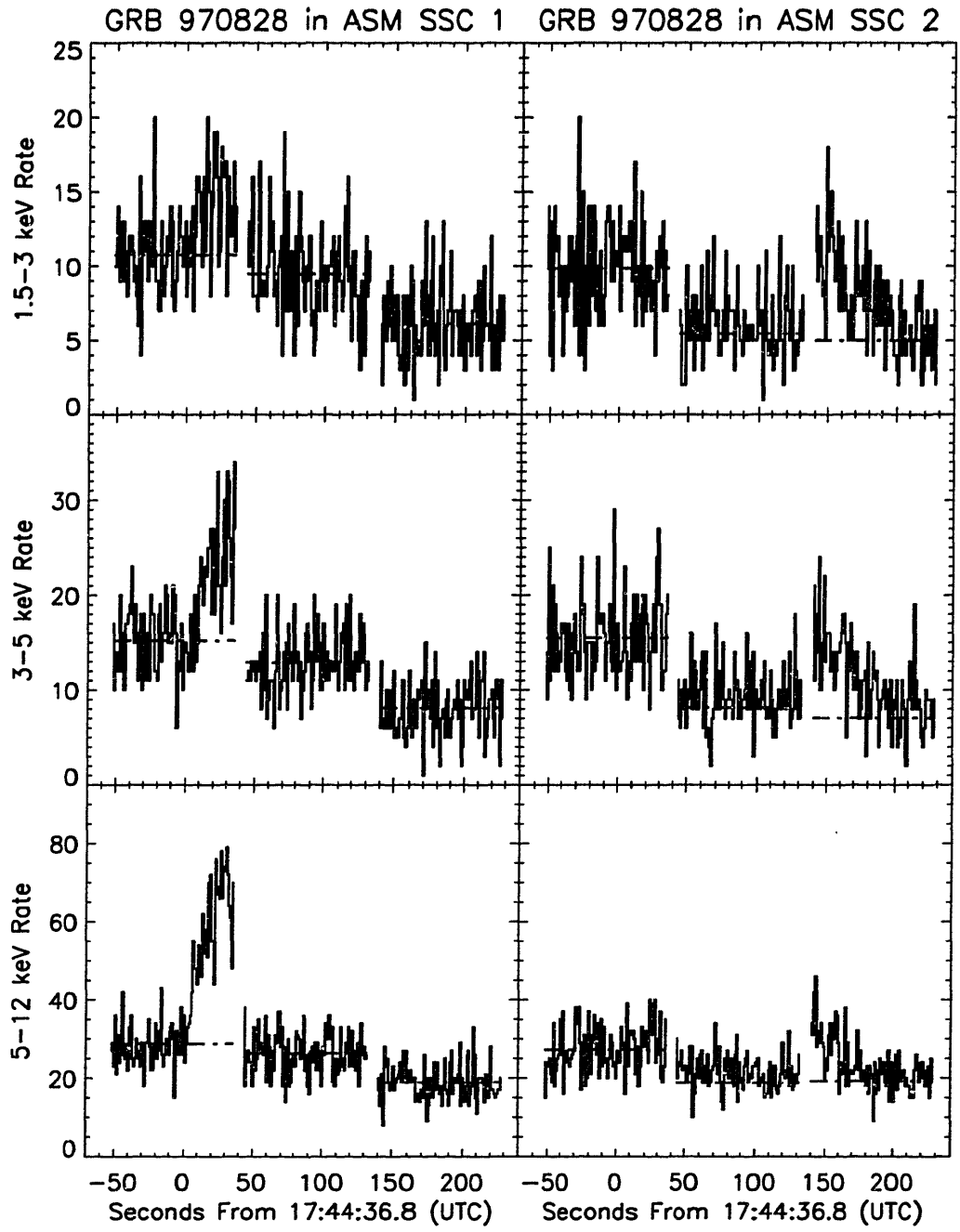

Figure 7-13 The time-series data in 1-s bins for the three observations of GRB 970828 in both SSC 1 and SSC 2. Gaps indicate the 6 s intervals between dwells when the ASM assembly was in motion. Broken lines estimate the contributions from all other sources in the FOV (Table A-10). The GRB was in the FOV of SSC 1 during the first dwell, at the edge of SSC 2 during the second, and near the center of SSC 2 during the last dwell.

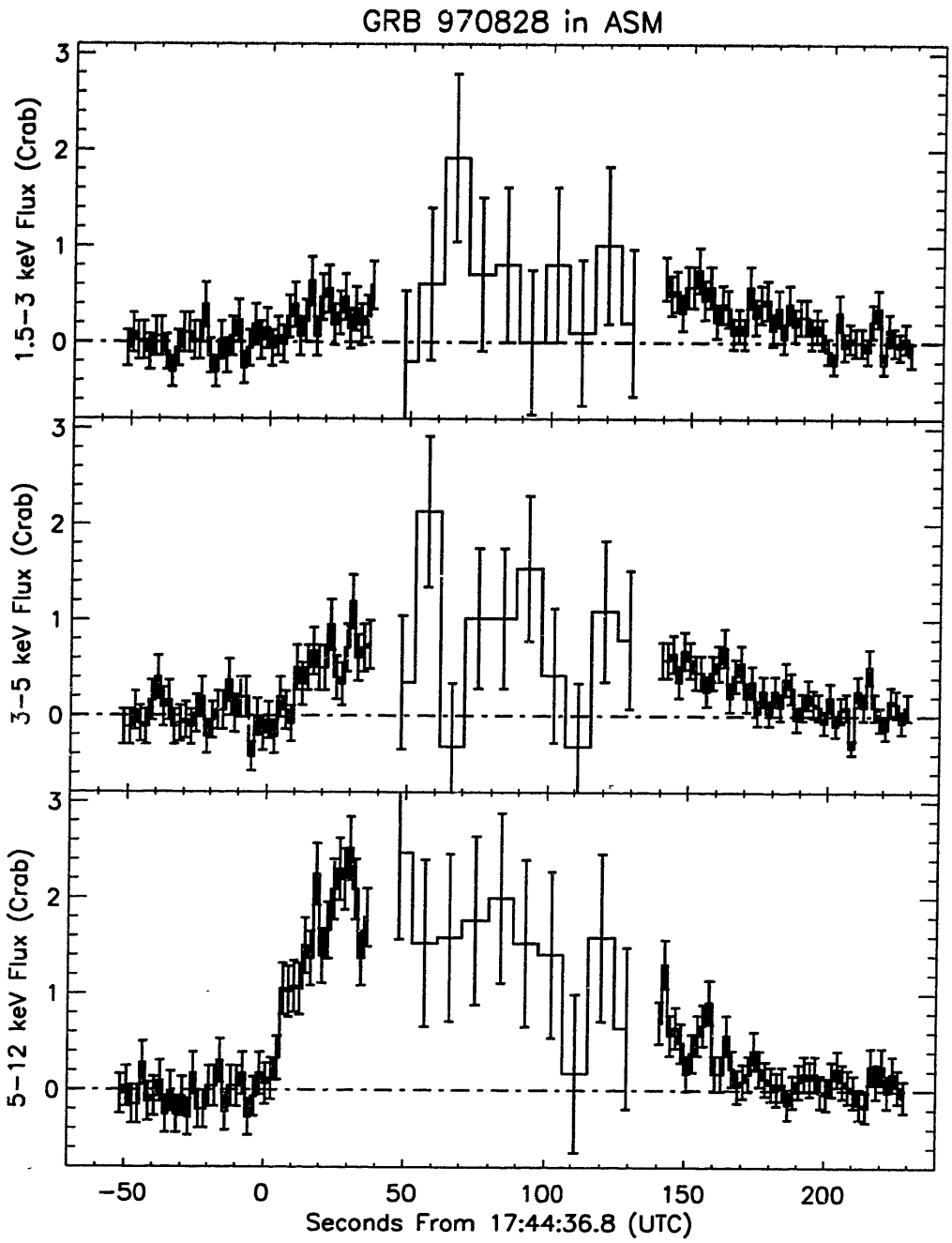

Figure 7-14 The light curve in Crab flux units of GRB 970828 in three energy channels. Gaps indicate the 6 s intervals between dwells when the ASM assembly was in motion. Due to the only 8% transmission during the second dwell, the data have been binned into 9-s bins. The other dwells are graphed in 2-s bins.

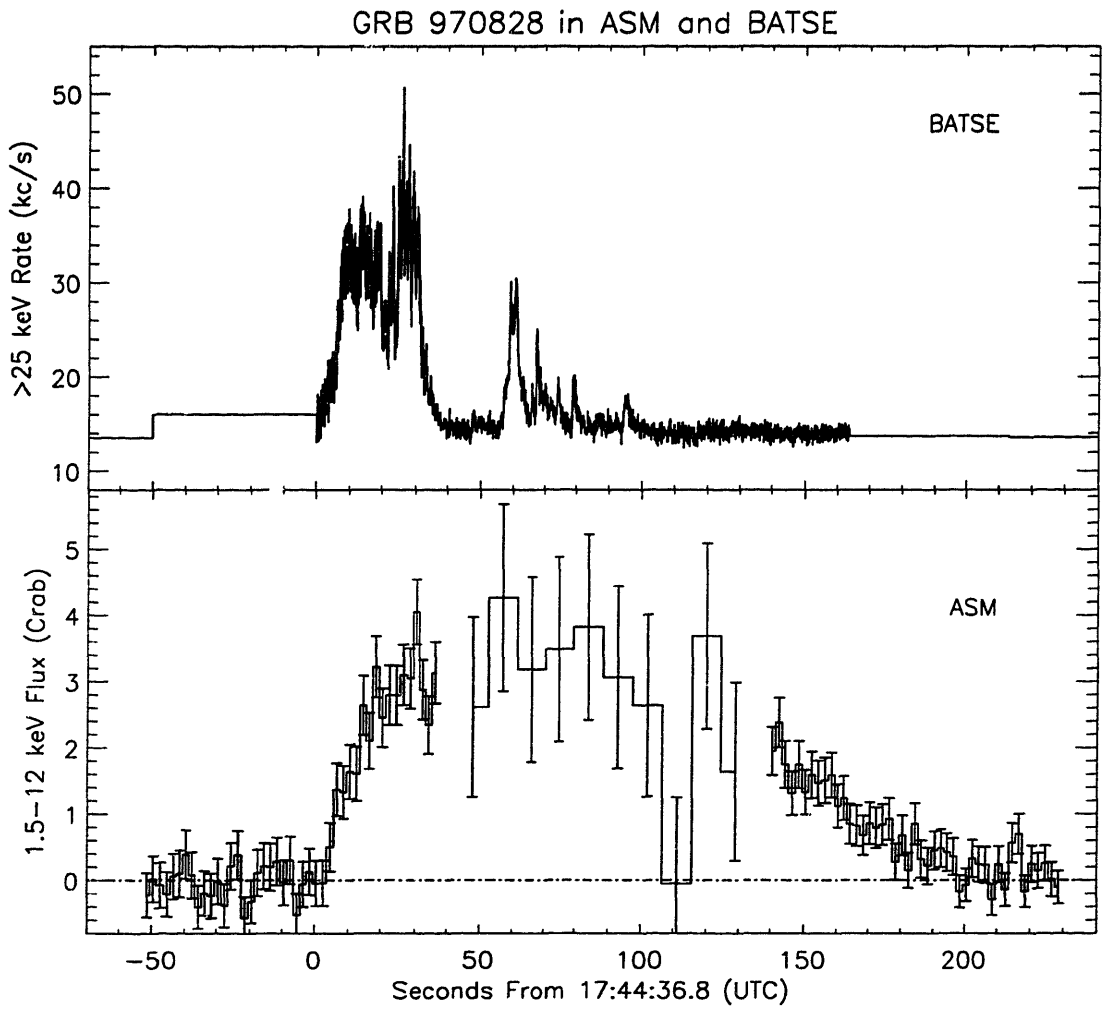

Figure 7-15 The ASM time-series data in 2-s and 9-s bins for GRB 970828 in Crab flux units (1.5–12 keV) as in Fig. 7-14, compared with data from BATSE (> 25 keV).

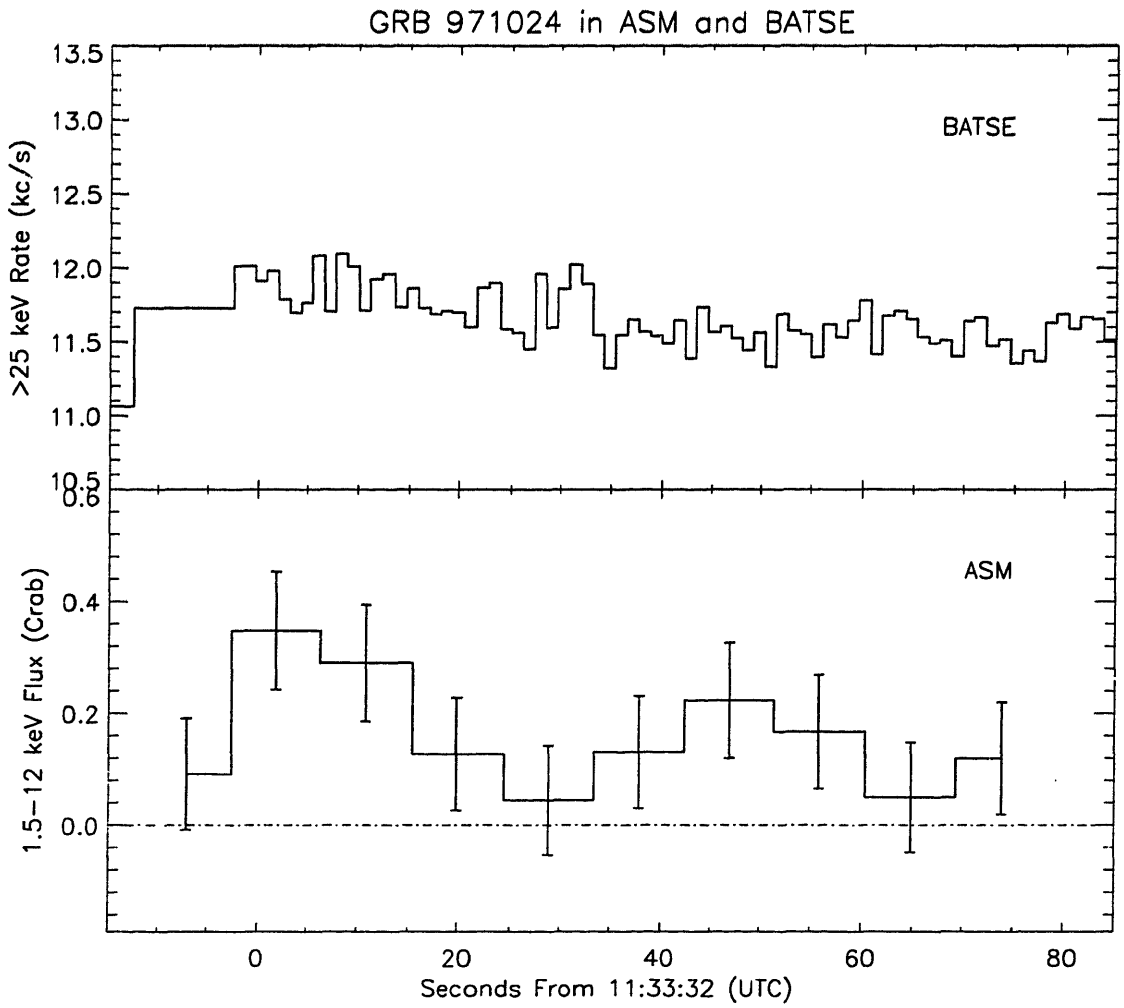

Figure 7-16 The time-series data for GRB 971024 in both the ASM (9-s bins; 1.5–12 keV) and BATSE (1.15-s bins; > 25 keV).

GRB 971024 was an extremely weak burst in all energy bands. Although it was detected in both SSCs 1 and 2, and a localization was released only 11 h after the burst, the detections were not strong. The position was relatively large (Section 5.2.1), and only two groups attempted follow-up observations. Images were taken at 14 h and 24 h after the burst, but no variable objects were discovered [163, 76]. Figure 7-16 compares the ASM light curve from SSC 1 in Crab flux units with the count rate from BATSE at the same time, and it is difficult to tell that there is any gamma-ray emission at all.

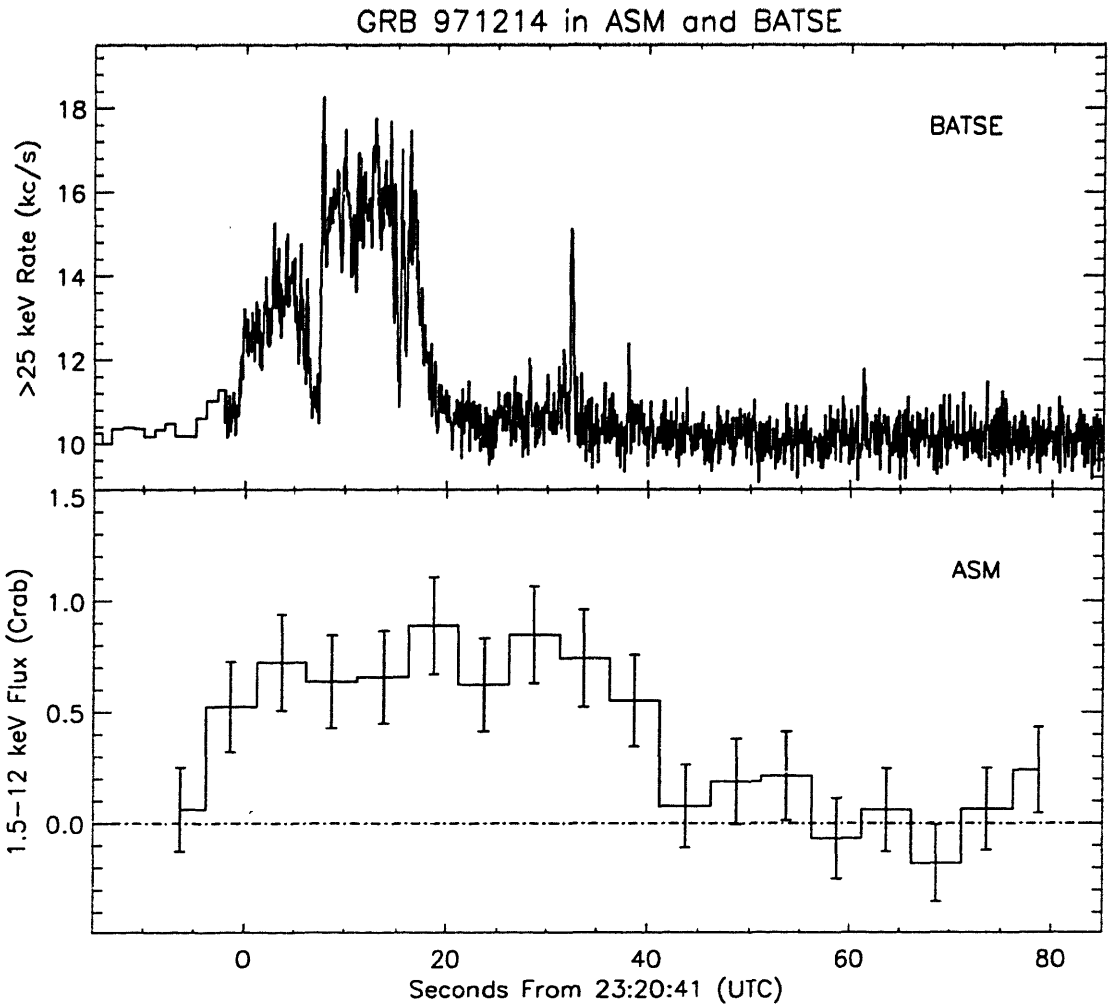

Figure 7-17 The time-series data for GRB 971214 in both the ASM (5-s bins; 1.5–12 keV) and BATSE (> 25 keV).

GRB 971214 was detected on a Sunday evening as a fairly bright singly-peaked event in SSC 3 during a single dwell. The event lasted around 40 s and displayed no significant substructure. A long, thin position was released over the GCN within 3.5 h. Largely due to a simultaneous serendipitous detection of this burst by the WFC on *BeppoSAX* [58], an optical counterpart to this event was rapidly identified [55], and later observations indicated that the host galaxy candidate had a redshift of $z = 3.42$ [87], which remains the highest redshift yet recorded for a GRB host galaxy (See Section 5.2.1 for details on the various localizations of this GRB).

Figure 7-17 shows both the ASM light curve for GRB 971214 in Crab flux units as well as the BATSE count rate during the corresponding time interval. As with GRB 970828, the gamma-ray data show a much more complex structure than the X-ray data, and the duration of the X-ray event is longer than its gamma-ray counterpart. If the X-ray event is only related to the initial burst seen in the BATSE data, and not the smaller spikes seen at 32 and 38 s after the trigger time, then the X-ray event is longer by a full factor of two. Certainly the spikes show no obvious response at energies below 12 keV, but perhaps they cannot be distinguished from the response to the initial burst, which is still bright at these times.

GRB 980703 was first detected in the common region of overlap between SSCs 1 and 2. The light curve of this GRB in both SSCs is shown in Figure 7-18. The flux began a rapid rise at roughly 60 s after the start of the 90-s dwell. It seems to have reached its peak intensity at the end of the dwell, perhaps shortly before the end in the hardest energy channel. As with GRBs 970815 and 960416, and perhaps 970828, there may be a soft lag in the times of peak emission in each energy channel. The behavior of the GRB at the peak is hard to determine, because the ASM rotated at precisely this moment. As the camera moves across the source, the transmission function and the normalization factors of the GRB change, and I have not tried to interpolate these values across the 6 s between dwells. During the second dwell, the GRB is not in the FOV of SSC 2, but it is 0°.6 from the edge of the FOV of SSC 1, so a light curve of the decay slope can still be reconstructed, albeit in large (9-s) time bins.

Figure 7-19 shows the 1.5–12 keV light curve from SSC 1 for GRB 980703 in comparison with the BATSE count rates. Although the overall similarity is clear, there are glaring differences between these events. The triply-peaked structure of the BATSE count rate is absent from the ASM light curve. There may be an X-ray response to the initial "plateau" at $\sim$ 30 s before the trigger, but at very low significance. The rise of the X-ray flux seems to precede that of the gamma-rays

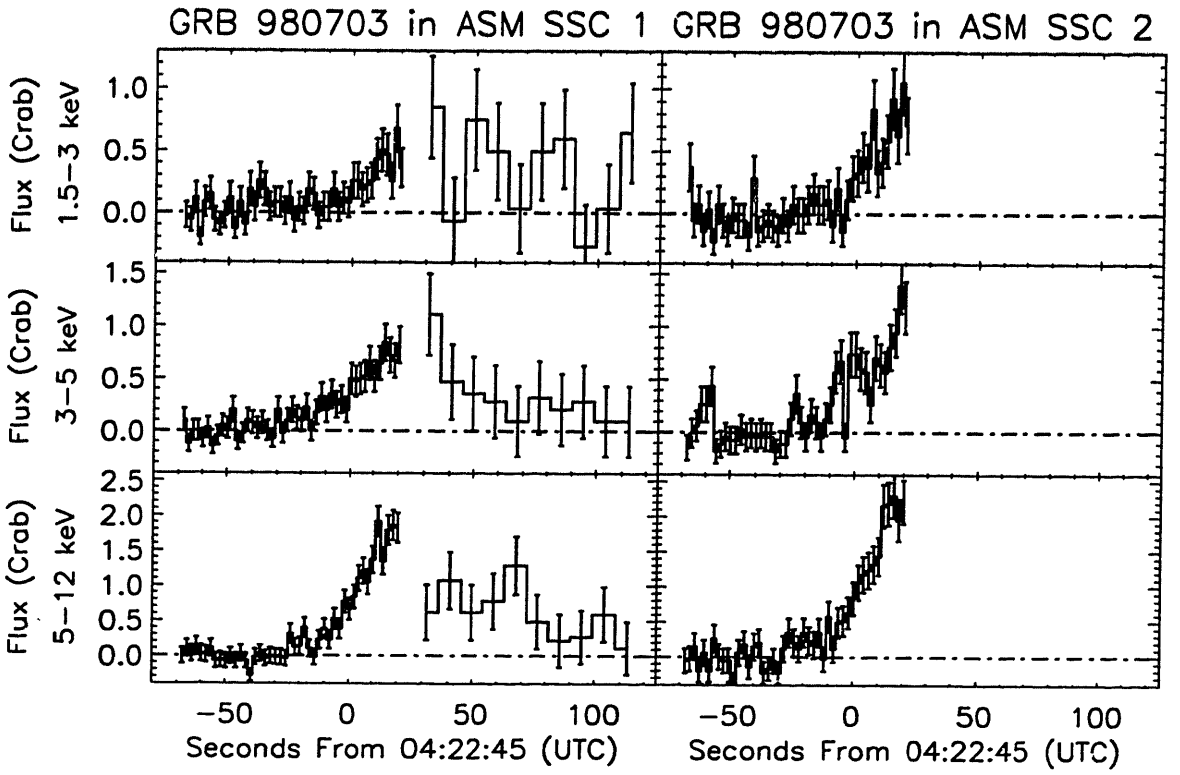

Figure 7-18 The time-series data for ASM observations of GRB 980703 in 5 s bins and three energy channels, background-subtracted and converted to flux units by comparison with the Crab flux. A gap indicates the 6 s interval between dwells when the ASM assembly was in motion. No data is shown for the second dwell in SSC 2 because the GRB was not within the FOV at this time. The apparent discrepancy between the peak fluxes in SSC 1 and SSC 2 is not statistically significant ($< 2\sigma$).

(unless the X-ray rise is a delayed response to the plateau), while the time of peak emission is later at lower energies. Both events show a lengthy decay tail, but it is difficult to say whether or not the X-ray light curve shares the change in decay timescales at $t \sim 25$ s.

It is worth noting that the BATSE count rates reveal a second interval of emission from this burst, roughly 300 s after the onset of the event, as shown in Figure 7-20. By this time, the ASM had scanned three more times, putting the burst location far outside the FOV, so the ASM cannot provide information about the X-ray properties of this second peak.

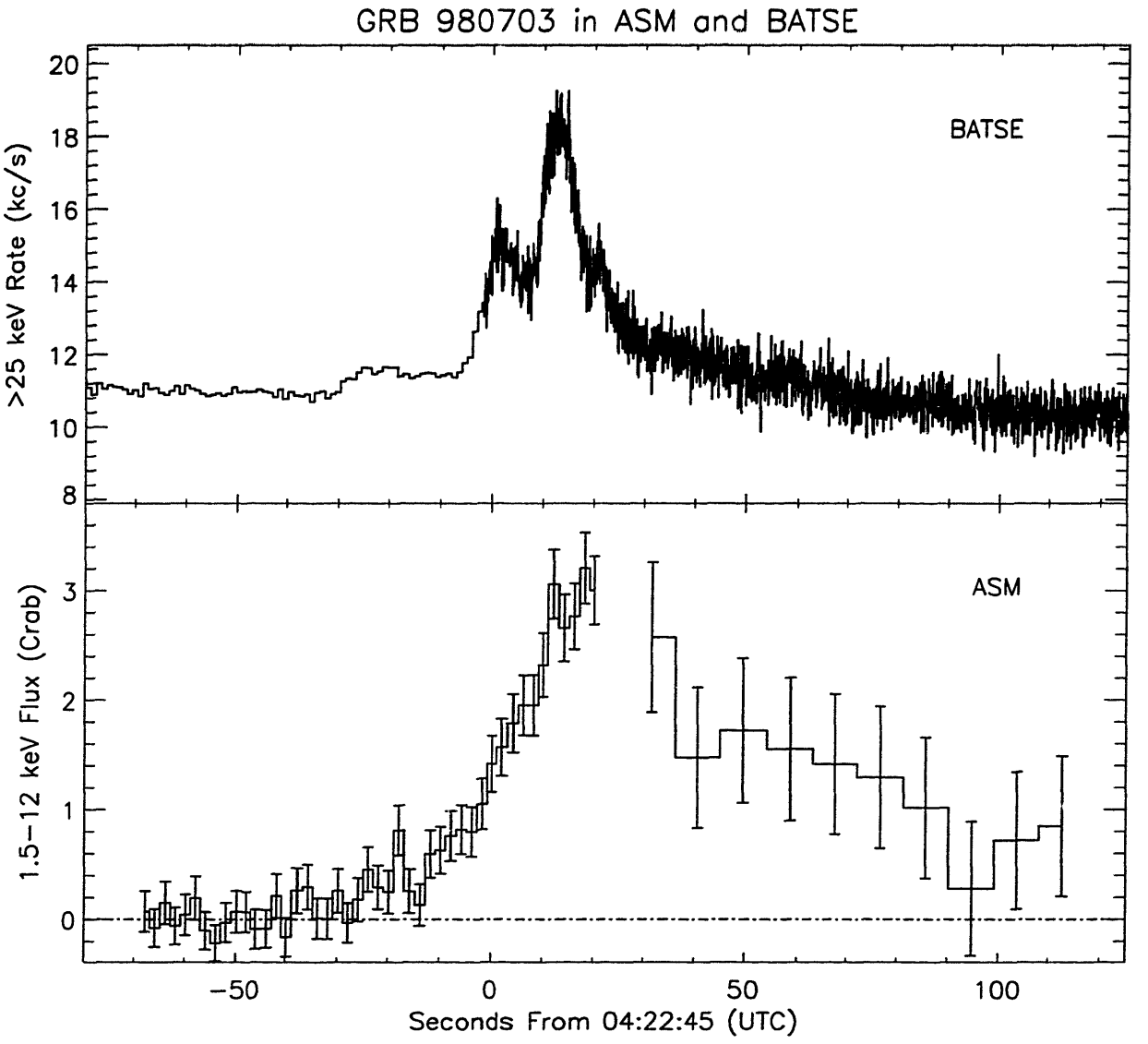

Figure 7-19 The time-series data for GRB 980703 in both the ASM SSC 1 (2-s and 9-s bins; 1.5–12 keV) and BATSE (> 25 keV).

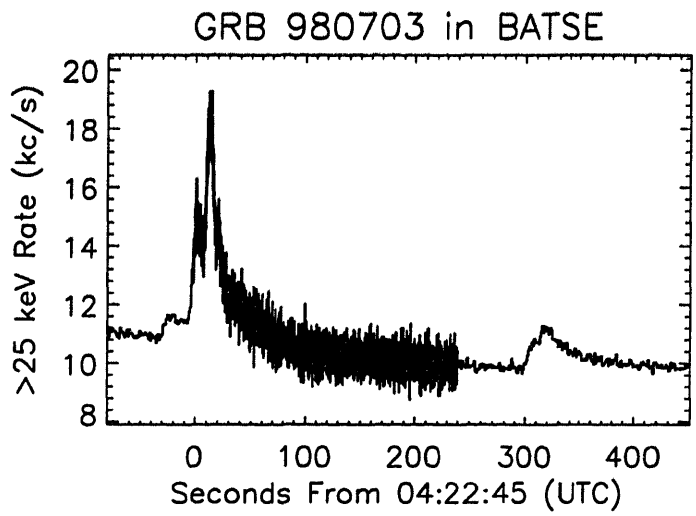

Figure 7-20 The time-series data for GRB 980703 as observed by BATSE (> 25 keV), showing the second peak that occured after the ASM had scanned off of the source.

GRB 981220 was observed in SSC 2 near the end of a 90-s dwell. This is the brightest GRB yet observed in the ASM data, reaching a total peak flux of over 13 Crabs! Although this event was not observed by BATSE, it was observed in the GRBM on board *BeppoSAX*. Figure 7-21 shows both the GRBM count rate for this event as well as the 1.5–12 keV light curve from the ASM in Crab flux units. The sharp spike at $t \sim 20$ s is an artifact, most likely caused by particle contamination (M. Feroci, 1999, private communication). This event shares the common properties of many GRBs where X-ray and gamma-ray data can be compared. The X-ray flux rise precedes the start of the gamma-ray event, the X-ray peak lags the gamma-ray peak, the spectrum softens during the decay, and the complex internal structure of the gamma-ray event is largely washed out.

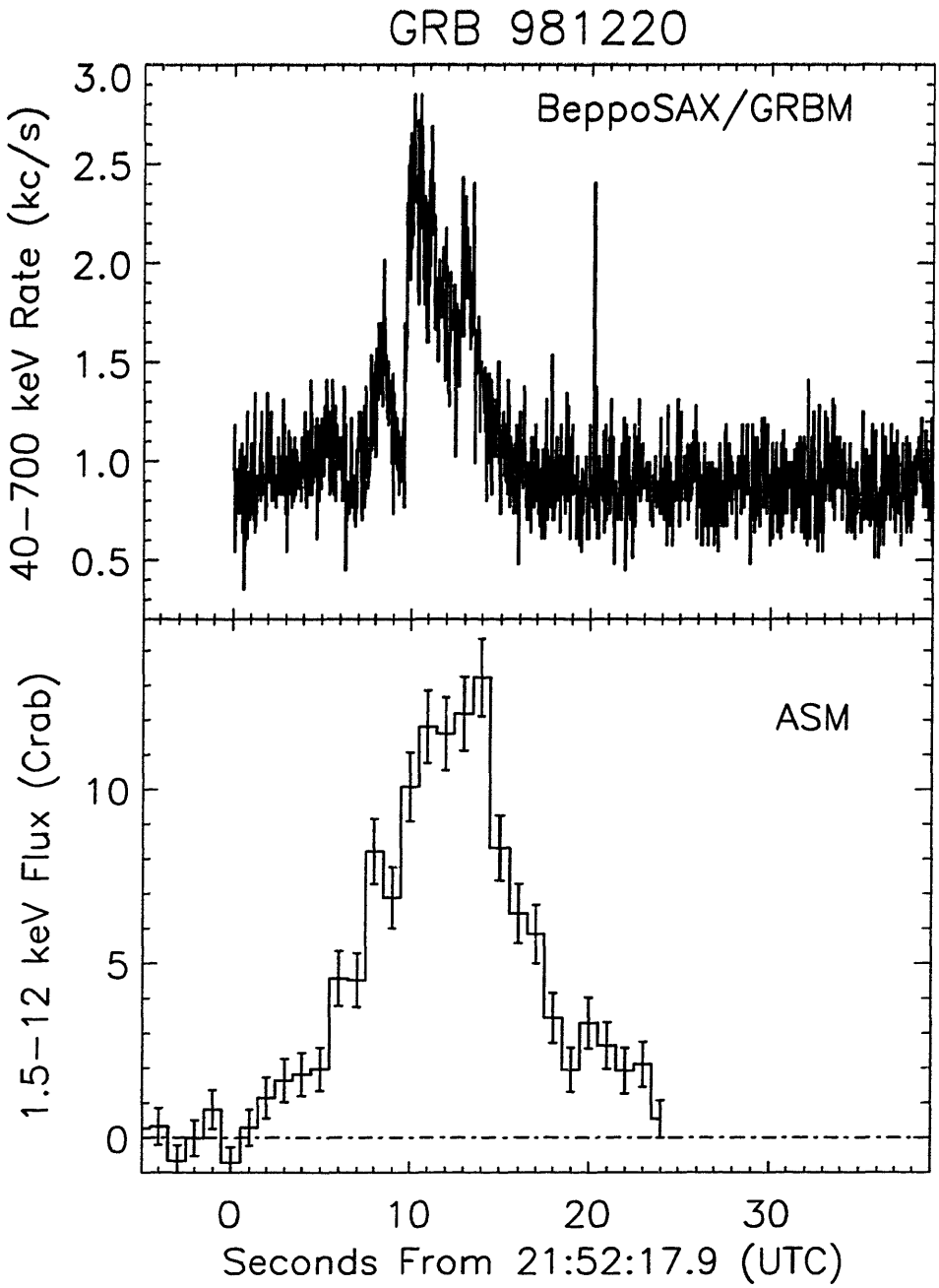

Figure 7-21 The bottom panel shows the time-series data (1.5–12 keV in Crab flux units) for the ASM observation of GRB 981220 in 2 s bins, while the top panel shows the count rate in the *BeppoSAX* GRB Monitor.

7.2.3 A Note About Errors

Equation 3.2, the equation that defines the procedure for using position histogram and multiple time-series data jointly to derive an event light curve on time scales shorter than 90-s, is a linear formula: $r_j = \alpha \times n_j - \beta$, where $\alpha \equiv a/(f\ s\ C_r)$ and

$$\beta \equiv \frac{N\ a}{f\ e\ C_r} - \frac{R}{C_r}.$$

To determine the error in the intrinsic flux, I have assumed that the scale change does not introduce any significant error into the result. That is, I assume that $\sigma_\alpha \approx 0$. In that case, $\sigma_r = \sigma_\beta$, and I derive σ_β through application of the standard error propagation formula (from, e.g., [7]): if $y = \mathcal{F}(x_i)$, then

$$\sigma_y^2 = \sum_i \left(\frac{\partial \mathcal{F}}{\partial x_i}\right)^2 \sigma_{x_i}^2.$$

In this case, $\mathcal{F}(x_i) = \frac{N\ a}{f\ e\ C_r} - \frac{R}{C_r}$, so

$$\sigma_\beta^2 = \left(\frac{\sigma_N\ a}{f\ e\ C_r}\right)^2 + \left(\frac{\sigma_R}{C_r}\right)^2,$$

where σ_R is taken directly from the results of the fit to the position histogram data, and σ_N is taken from the counting statistics of the observation: $\sigma_N = \sqrt{N}$.

7.3 Summary

There's a famous saying that "when you've seen one gamma-ray burst... you've seen one gamma-ray burst". Even the small sample of fourteen GRB X-ray light curves presented here provides a bewildering diversity of form. None of these bursts show the classic simplicity of the familiar fast-rise, exponential-decay envelope one might expect from an impulsive event. GRB 961019 is close, but has two minor peaks superposed on the decay curve. Several bursts show a near-symmetric single-

peak, with or without significant structure on smaller time scales. One or two bursts (GRBs 961002 and 961216) even seem to have a slow-rise, fast-decay structure! About half the bursts show multiple, distinct peaks, while two (GRBs 970828 and 971214) have a veritable forest of tiny peaks within the overall structure of their gamma-ray emission history.

Nevertheless, some general conclusions can be drawn from these data. First of all, the X-ray emission is clearly smoother and in almost all cases lasts longer than any associated gamma-ray flux. Some of this is due to the limitations of counting statistics in the ASM, when we are forced to use bins up to nine-seconds long, but the general result is easily understood within the context of synchrotron radiation theory, in which cooling timescales lengthen at lower frequencies. Equation 6.57 predicts that the cooling timescale should fall with the energy band of the observation as $E^{-1/2}$. Of the GRBs presented in this chapter, only GRB 960416 provides the opportunity to test this prediction across many energy bands. Light curves from other bursts are either incomplete (e.g., GRB 980703), lack high-energy data, or fail to provide enough counts to measure a useful width in multiple energy channels (e.g. GRB 971214). As shown in Figure 7-22, the widths of both peaks in GRB 960416 are consistent with a $E^{-1/2}$ scaling law. Piro et al. showed a similar result for GRB 960720 using data from *BeppoSAX*, but GRB 960720 was a very simple, single-peaked burst [123]. GRB 960416 was double-peaked, and each of the two peaks shows a similar scaling.

It should be noted that the timescale for synchrotron cooling at 10 keV is $\sim 10^{-2}$ s, according to Equation 6.57, while the timescale for angular spreading, as described in Section 6.3, could be much longer, depending on the Lorentz factor and the interaction radius. Angular spreading could therefore be enhancing the effect of the synchrotron cooling, but the fact that the peak widths do scale as $E^{-1/2}$ supports the idea that synchrotron radiation is indeed the underlying cause of the emission.

The ASM light curves for GRB 970828 and GRB 971214 do not match well with an extrapolation of the $\tau \sim E^{-1/2}$ law from $\sim$ 100 keV to $\sim$ 5 keV, using the width

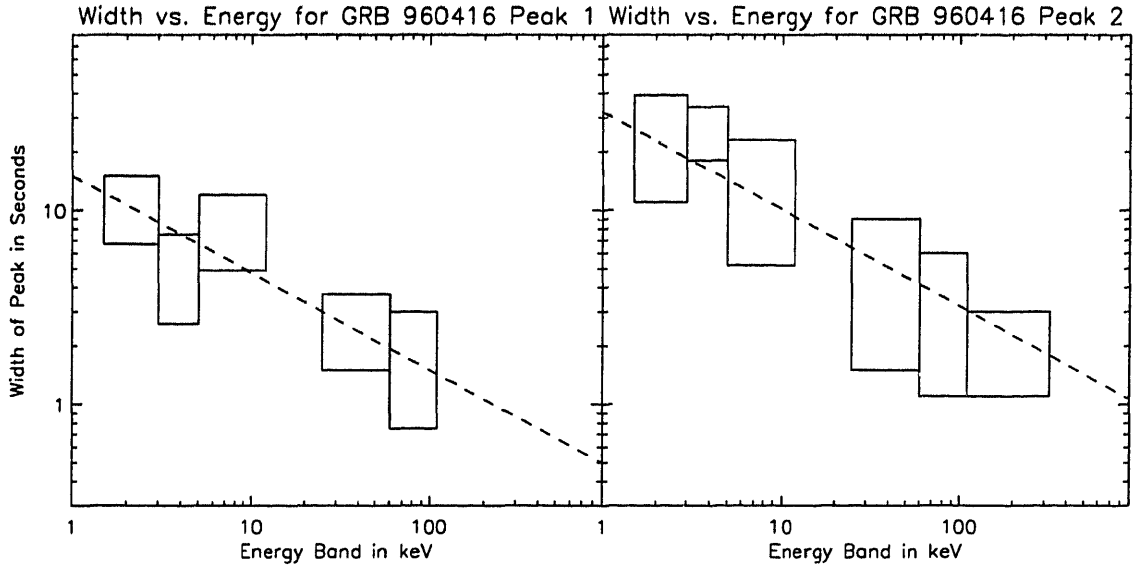

Figure 7-22 For each of the two peaks of GRB 960416 (Fig. 7-2), the 1σ, $1/e$ width is plotted versus the six available energy channels below 320 keV (using data from BATSE and the ASM). The first peak was not strong enough in the 110–320 keV band to measure a width. The dashed line shows a power law with index of -0.5 and a normalization chosen by inspection.

of the primary BATSE peak as the starting point. Based on this law, GRB 970828 should last $\sim$ 100 s, but its duration is closer to 200 s (Fig. 7-15). The main peak of GRB 971214, as recorded by BATSE, is 18 s wide, which would correspond to an ASM peak width of 80 s, which is clearly longer than the $\sim$ 40 s peak observed (Fig. 7-17). It is interesting to note that these GRBs are also the two GRBs that show a complex forest of peaks in the BATSE light curve. In neither of these cases is any evidence for the smaller peaks apparent in the ASM data, although in both cases, poor statistics diminish the ability to detect small fluctuations in the ASM count rate. Within the context of the internal shock model, the extended length of the ASM light curve for GRB 970828 is easily interpreted as the ongoing refreshing of the initial shock, which does not have time to cool in the X-ray regime before it is shocked again. In the case of GRB 971214, perhaps the main peak is actually the superposition of emission from many rapid shocks (indeed, there is clearly stucture

on small time-scales within the peak), and so the the relevant peak width is not that of the entire BATSE event, but rather that of the sub-peaks, in which case the ASM response, like that of GRB 970828, is greatly extended.

Many individual emission peaks show a soft lag in their times of maximum count rate, but it is worth noting that several do not, at least within the limitations of the time bins (Fig. 7-5). In the single case of GRB 970815, there is the tantalizing possibility that the final peak seen in the X-ray light curve may be the beginning of the afterglow associated with the external shock, but the data are not detailed enough to confirm or exclude this hypothesis.

In at least two cases, the X-rays can be seen to rise before the onset of the GRB in the higher-energy regime. The first peak of GRB 960416 seems to start before its BATSE counterpart, and GRB 981220 seems quite active in the ASM before the count rate in the *BeppoSAX* GRBM begins to rise. It's possible that the X-ray count rates precede the gamma-rays in GRB 961216, but the poor statistics of the ASM observation render this uncertain. GRB 980703 is difficult to interpret, as it is unclear if the rising X-ray emission is related to the pre-trigger plateau in the BATSE count rate or the onset of the burst proper. In no case, however, did we observe any candidate for a distinct X-ray precursor, such as that associated with GRB 980519 [74] or perhaps GRB 900126 [111]. These events are very rare, so their absence in the ASM sample is unsurprising.

What perhaps are more surprising in their absence are the total lack of GRBs shorter than 10 s in duration. The GRBs in the BATSE catalog have a well-known bi-modal duration distribution with peaks at 0.1 s and 10 s [86, 31, 84]. All the GRBs here are drawn from the longer sub-population. It is true that we are less likely to be able to localize short bursts because our positions depend on the number of counts available (Chapter 4), but our variability search was conducted on time-scales of 1/8-s, 1-s, and 9-s, so a bright 0.5 s burst should have easily triggered that alarm, as did the short bursts from SGR 1627–41 [148]. Yet we found no evidence for a population

of short GRBs in the 1.5–12 keV range. The short population represents roughly 25% of the first BATSE GRB catalog [86], so perhaps counting statistics have just worked against us, but it is noteworthy that all of the bursts localized to date by the *BeppoSAX* WFC have also been from the longer population. The BATSE data suggest that the shorter bursts also have harder spectra, so perhaps they are simply not bright enough in the 1.5–12 keV range for the ASM to detect them.

Chapter 8

Late-Time Radio Afterglow

8.1 Introduction

The driving force behind all the excitement in the field of gamma-ray burst studies in the last few years has been the proof that the rapid distribution of accurate positions for the bursts can lead to the identification of the fading remnants and possibly their host galaxies. The chief limiting factor is the short time over which the optical afterglow from a GRB is bright enough to observe. Fewer than 50% of the 33 rapidly-localized GRBs have been detected at optical wavelengths [50]. Groot et al. [53] attribute this deficit to a rapid power-law decay which quickly renders the source undetectable. This is especially troublesome when there may exist a delay of a day or more between the time when the GRB is detected and an accurate localization is provided.

One possibility for identifying additional host galaxies is through the study of long-lived radio afterglows from GRBs. According to the standard relativistic blast wave model for afterglows [127] the decay of the radio emission at ν_R is delayed from the optical ν_o by the ratio $(\nu_o/\nu_R)^{2/3} \sim 10^3$, as shown in Equation 6.32. Factors such as synchrotron cooling, a transition to sub-relativistic expansion, and the possibility of the shock parameters evolving in time [167, 135] will modify the exact value of this

delay. Nevertheless, the radio lifetime of afterglows can be large. GRB 970508 was still readily detectable at 1.4 GHz more than a year after the initial gamma-ray event [34]. An added advantage of the radio band over optical is that it allows for the detection of GRBs which are optically-obscured due to their dusty environments [157]. It is therefore possible that radio observations of GRB error boxes may yield counterpart detections even a year or more after the events.

In this chapter we present radio observations made at the Very Large Array[1] (VLA) and the Australia Compact Array Telescope[2] (ATCA) of several GRB error boxes which were identified in the archival searches of the ASM database (See Chapter 5), months to years after the event. The long delay between event and the determination of a position rendered a search for optical counterparts to these events infeasible, but these observations were carried out in the hope of detecting long-lived afterglow. In collaboration with Dr. D. Frail at NRAO and Dr. S. Kulkarni at CalTech, I traveled to Narrabri, NSW, and Soccoro, NM, to carry out observations of these six error boxes and reduce the data. Dr. Frail instructed me in the data analysis and contributed to the content of this chapter.

8.2 Observations

In a search of ASM archival data between January 1996 and July 1997, a total of eight GRB candidates have been identified (Chapter 5). Six of these eight GRBs were localized by the ASM, or by the ASM in conjunction with the interplanetary network (IPN), to error boxes small enough to merit a search for radio afterglow. These error boxes are plotted in Figures 5-1 and 5-2, and their characteristics are summarized in Table 8-1. Unlike some more recent ASM bursts – GRB 970815, GRB 970828,

[1]The Very Large Array is a facility of the National Science Foundation operated under cooperative agreement by Associated Universities, Inc.

[2]The Australia Telescope is funded by the Commonwealth of Australia for operation as a National Facility managed by CSIRO.

Date of GRB (yymmdd)	2-12 keV Fluence (10^{-7} ergs cm^{-2})	R.A. (J2000)	Decl. (J2000)	Error Box Area Sq. Arcmin.
960416	6.0 ± 0.3	04h15m30s	77°10′	19.6
960529	$> 17.5 \pm 0.6$	02h21m40s	83°24′	19.0
960727	9.5 ± 0.5	03h36m36s	27°26′	4.1
961002	9.2 ± 0.5	05h34m46s	−16°44′	6.7
961019	4.6 ± 0.6	22h49m00s	−80°08′	524.8
961230	1.5 ± 0.3	20h36m45s	−69°06′	229.1

Table 8-1: Properties of X-ray Error Boxes for Six GRBs

GRB 971024, GRB 971214, GRB 980703, and GRB 981220 – these were not localized soon enough to allow for a search to be made for an optical afterglow.

Observations of GRB 961019 and GRB 961230 were made beginning on 1998 January 3 with the ATCA. A bandwidth of 128 MHz, divided into 32 channels of 4 MHz each was employed at 1.4 GHz and 2.3 GHz. VLA observations at 1.4 GHz and 4.9 GHz were made of GRB 960416 and GRB 960529 on 1998 May 10. The VLA was in its A-array configuration so in order to image the entire error boxes the 50 MHz bandwidth was subdivided into eight channels. On 1998 June 14, when the VLA observations for GRB 960727 and GRB 961002 were carried out, the VLA had moved to its more compact B-array configuration. In this instance two 25 MHz-wide continuum channels were used at frequency (1.4 GHz and 4.9 GHz) giving maximum sensitivity over the entire error box. During both the VLA and ATCA runs known extragalactic sources were observed to calibrate the flux density scale and the instrumental phase. Off-line processing of these data was carried out using the AIPS package following standard practices.

8.3 Results

The final images of each GRB error box were inspected for radio sources at both frequencies. A source above 5σ was considered a possible detection but to be verified

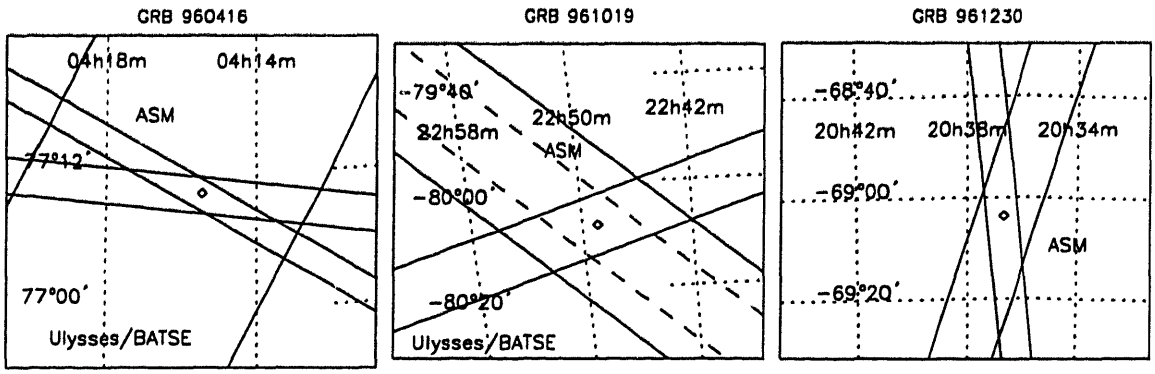

Figure 8-1 The ASM localizations of three gamma-ray bursts, compared with position information from other satellites when available. ASM and BATSE locations are given at 90% confidence, while IPN annuli are 3 σ. A 1 σ error box for GRB 961019 is also shown as a dashed line. Positions of three radio sources are also plotted as diamonds (See Table 8-2).

it had to be seen in different subsets of the data divided in time and frequency. By these criteria three radio sources were found in three separate GRB error boxes. The flux densities and positions of our detections are listed in Table 8-2 and their locations within the error box are plotted as diamond symbols in Figure 8-1. The rms noise limits for each image are given in Table 8-3.

A 180 μJy radio source was detected at 4.9 GHz in the error box for GRB 960416. The source is unresolved by our 0.4″ beam. It was not seen at 1.4 GHz but the rms noise is high due to a 5 Jy source in the field-of-view which limits the final dynamic range in the image. The absence of emission at 1.4 GHz constrains the spectrum to have a slope $\alpha > -0.5$ (where $S_\nu \propto \nu^\alpha$).

Near the center of the error box for GRB 961019 is a 450 μJy source at 2.6 GHz, unresolved at our resolution of 3″. The absence of emission at 1.4 GHz constrains the spectrum to have a slope $\alpha > 2.0$. Although the 2-12 keV fluence of GRB 961019 was well above the ASM detection threshhold, the position of the source was near the edge of the field of view, significantly reducing the observed photon count and increasing the width of the (non-Gaussian) error distribution. Both the 90% and the 68% error boxes are shown in Figure 8-1, with widths of 40′ and 8′, respectively (Chapter 4).

Date of GRB (yymmdd)	Peak Flux Density (μJy)	Frequency (GHz)	R.A.[1] (J2000)	Decl.[1] (J2000)	Probability of Chance Detection
960416	180	4.9	04h 15m 26.850s	+77°09′49.4″	0.63
961019	450	2.6	22h 48m 55.027s	−80°07′22.4″	1.00
961230	400	2.6	20h 36m 41.616s	−69°03′42.5″	1.00

Table 8-2: Source Properties for Radio Afterglow Candidates

Date of GRB (yymmdd)	RMS Noise 1.5 GHz (μJy)	RMS Noise 2.6 GHz (μJy)	RMS Noise 4.9 GHz (μJy)
960416	110	–	30
960529	50	–	30
960727	70	–	75
961002	120	–	80
961019	50	50	–
961230	110	60	–

Table 8-3: Radio Noise in ASM GRB Error Boxes

GRB 961230 was very dim in X-rays, but it was observed in two ASM cameras simultaneously. Therefore there are two, intersecting, lines of position, of width 7.4′ and 12.2′. The ATCA observations show an unresolved source, comparable to the source in the box for GRB 961019, near the center of the intersection of the ASM error boxes. This source was 400 μJy at 2.6 GHz and 550 μJy at 1.5 GHz, yielding a spectral index of $\alpha = -0.6$. Near the edge of this intersection diamond at R.A.=$20^h36^m25.498^s$, Decl.=−69°03′59.2″ is a 1 mJy source. However, it is clearly extended with a size of order 4″ and thus we do not consider it to be an afterglow candidate.

[1]The position error in both right ascension and declination is typically ±0.2″.

8.4 Discussion and Conclusions

We have identified three radio sources inside the error boxes of six GRBs. It remains to be determined whether any of these are the radio afterglow from a GRB or just background radio sources along the line of sight. It is encouraging that two of these identifications are toward the two most recent GRBs (GRB 961019 and GRB 961230) in our sample. On the other hand these are also the three largest error boxes in our sample. The *a posteriori* probability of detecting a weak background radio source at these frequencies with these large error boxes is nearly unity. We present the results of such calculations in Table 8-2, using the source counts of [33] and scaling to 2.6 GHz assuming $\alpha = -0.35$.

There are a few aspects of the characteristics of these three candidates that hint at a distinction from the population of sub-milliJansky radio sources described in Fomalont et al. [33]. The median angular size of the general population increases from 0.8″ to 1.3″ as the flux density decreases, but the candidate for GRB 960416 is unresolved at a beam of 0.4″. The majority of the population has flat spectral indices ($< \alpha >= -0.4$), while the limit on the spectral index for the candidate to GRB 961019 is $\alpha > 2.0$. However, for late times in the fireball model for GRB afterglows, the synchrotron emission spectrum is expected to have a falling spectrum, as shown in Equation 6.47. Clearly we need some other means to distinguish which if any of these radio sources is a GRB afterglow.

A re-observation of these fields with the VLA or ATCA at some later date may be useful, but even if significant variability is measured between observations, very little is known about the variability of sub-milliJansky radio sources [34], so this in itself would not be definitive. However, AGN variability tends to be achromatic [34], while GRB radio afterglow has shown strong frequency dependence in its behavior [38], so further multifrequency radio monitoring could provide further evidence to distinguish between the two.

Optical images and spectroscopy would be most useful. Sources below a few

milliJanskys are preferentially identified with normal nearby spirals or disturbed, faint blue galaxies (median $V \sim 27.5$); most identifications were coincident with the nuclear regions of a galaxy, although some were associated with a spiral arm or knot of emission [33, 130]. With two exceptions at R$\sim$22, the nine GRB host galaxies detected so far tend to cluster around 25th magnitude [62, 10], and the majority show evidence of star-formation (not counting GRB 980425, which may be a different class of GRB [88].).

We examined the DSS and the APM catalogs towards these three GRBs. We estimate that the plate limits are at R$\simeq$20.6 and B$\simeq$22.8. There is a moderately bright galaxy 4″ to the north of the radio candidate for GRB 960416 in both the DSS and the APM. According to the APM, the magnitudes of this galaxy are B=18.21, R=16.83. Unless the GRB was ejected from this galaxy it is too far away to be the host. The other two GRBs have no optical source within about 10-20″ down to the plate limits.

Deeper optical searches could identify the host galaxies for these objects and resolve the uncertainty about their identities. Only seven radio counterparts to GRBs have yet been detected, and only seven GRB host galaxies have a measured redshift (not including GRB 980425). The results presented here are tantalizingly inconclusive, but they open the possibility for significant further development in the understanding of the origin of GRBs.

Chapter 9

Conclusions

The last two years have seen a remarkable evolution in the field of gamma-ray burst (GRB) studies. The availability of rapid, accurate localizations provided by X-ray telescopes such as the Wide-Field Camera (WFC) on *BeppoSAX* and the All-Sky Monitor (ASM) on the *Rossi X-ray Timing Explorer* (*RXTE*), coupled with quick responses by astronomers with other telescopes, have shown that these elusive explosions can be detected and studied in many wavelength bands. A wealth of new data has emerged that has settled long-standing debates about GRBs and raised new questions. Absorption and emission lines in the fading burst afterglows and the host galaxy candidates have shown that at least some GRBs originate in galaxies at cosmological distances. The salient properties of the afterglow behavior are in general agreement with the predictions of the fireball class of models. These models begin with some catastrophic event that releases more than a solar mass of energy into a relatively small volume as a photon-pair plasma along with much less than a solar mass of baryonic matter. This plasma expands at highly relativistic speeds, and it develops shocks which emit the observed radiation.

As more GRBs have been studied with rapid response campaigns, more and more complicating features have been observed that don't fit within the simplest fireball scenario. The afterglow from several GRBs show deviations from a simple powerlaw

decay in the form of flares or dips [173, 122, 43]. Recent work has suggested that the afterglow decay curves from GRB 970228 and GRB 980326 reveal evidence that a SN-type shell is catching up to the remnant of the GRB [128, 9]. A strong case has been made for the association of GRB 980425 with the relatively nearby supernova SN 1998bw, suggesting that GRBs may contain multiple classes of progenitor objects [88]. These discoveries demonstrate that our understanding of the diversity and range of characteristics of GRB sources depends on observations and followup of many GRBs.

This thesis presents my program to use the ASM to provide rapid, accurate GRB localizations that represent a valuable contribution to the ongoing effort to study the diversity of GRBs. We use coded-mask imaging techniques to determine the position and brightness of sources in the field of view. A single detection of an X-ray source can be used to localize that source to within a long, thin error box. Over time, as error boxes at different orientations are computed, they will pivot around the true source location, and the occasional spurious position can be easily excluded. With just one or two detections, however, it becomes more difficult to accurately constrain the source location to a reliable confidence level.

On occasion, the ASM serendipitously observes a GRB in progress. In the 2–12 keV band, GRBs rarely last more than a few hundred seconds at intensities bright enough for the ASM to detect them. In order to provide the rapid positions crucial for the study of GRBs, it is necessary to determine the exact reliability of an error box from only one or two ASM source detections.

I have undertaken a thorough empirical study of the ASM's ability to localize a source from a single detection. I found that the error box size could be accurately characterized by a function that depends only on the total number of counts detected from the source of interest. For a given confidence level, a detection yielding more counts from a source will result in a smaller error box, until a limiting systematic error is reached. This limit is different in each camera, but is on the order of $\pm 1.5'$ in

the short direction and $\pm 15'$ in the long direction. As the number of detected counts drops below 1000, the error box size increases rapidly, as does the probability that the detection is not the source at all, but actually a noise peak. For numbers of counts below 200 (300 in SSC 3), the detection is completely unreliable.

I, and other members of the ASM team, began looking for GRBs in the ASM data in mid-1997. We conducted a search of the 1.5 y of ASM observations available at that time, and we began inspecting the real-time data. From these inspections we developed a set of criteria to optimize the identification of real GRBs in the ASM data. I developed software to apply these criteria to the real-time data stream from the ASM as it arrives here at MIT. The time-series data from each 90-s observation is examined for excess variability that could be due to a GRB. The position-histogram data is routinely searched for new sources, and I archive all detected candidates. The vast majority of these are caused by solar X-rays that scatter off of the Earth's atmosphere or the inside of the ASM collimator and cause a soft response in the detectors. These spurious detections are filtered out. Of the remaining candidates, if two detections within 300 s produce error boxes that cross, or if a single observation yields both a new source candidate and excess time-series variability, alerts are distributed, and web pages are automatically generated that present the error boxes, time series data, and other information for myself or another ASM team member to evaluate. GRB detections from BATSE and the *BeppoSAX* GRB Monitor are sent to us over the internet, and if the ASM is taking data at the times of those triggers, my software subjects those observations to heightened scrutiny.

For the best, most reliable GRB-detection candidates, the alert is distributed automatically through the internet to any interested observers around the world. This system could in the best cases provide astronomers with a GRB position in less than 10 minutes of the event. However, the ASM has not observed a GRB under such optimal conditions since the system was fully implemented in January of 1999. An early version of the system led to the rapid localization of two X-ray novae in

September of 1998 [146, 151].

These efforts led to the identification of eight GRBs in the archived data and have enabled six GRB localizations between May 1997 and December 1998 to be distributed within 2 to 32 h after each event. Six of these fourteen bursts yielded detections in two ASM cameras, and so could be localized to a small, diamond-shaped error box. Five of the single-camera detections were also detected by instruments in the Interplanetary Network (IPN). The annuli that were derived from the IPN time-delay analysis were used to considerably shrink the long dimension of the associated ASM error box.

All in all, this work has provided the GRB community with four rapid locations to study which would not have otherwise been available. Our detection of GRB 970828 resulted in the fastest-yet community response to a GRB alert (it has since been superceded), with optical, radio and X-ray telescopes on source within four hours of the event. Remarkably, although the X-ray afterglow was readily visible, no optical counterpart was detected to startlingly low upper limits. Some interpreted this as evidence for heavy absorption near the GRB site, while others cautioned that a rapid temporal decay could be responsible. A late radio flare was only much later recognized to be associated with this GRB, and has since led to the identification of a host galaxy and the measurement of its redshift at $z = 0.96$ [21, 35]. GRB 980703 led to follow-up observations within 22 h, and fading counterparts were found at optical and radio wavelengths [10]. A spectroscopic redshift of $z = 0.97$ was measured from the optical transient [24]. The ASM GRB program presented in this thesis has thus made possible the measurement of two of the ten well-determined cosmological redshifts associated with GRBs (Table 2-1).

Since the radio emission from GRB 970508 remained visible to the VLA for well over a year after the event [34], I proposed with Dale Frail and Shri Kulkarni to search for late-time radio afterglows from the six well-localized GRBs found in the search through the ASM archival data. I traveled to Narrabri, Australia, and Socorro, NM to conduct the observations. These observations yielded weak detections of three

candidate sources. It was unfortunately not possible to unambiguously determine the relationship between these sources and the GRBs, and an association looks doubtful, but they offer an opportunity for future investigation.

The ASM time-series data provided the opportunity to study the light curves of these fourteen GRBs in the X-ray band. Although the time-series data records the counts from all sources in the FOV, I developed a procedure to isolate the light curve of a variable source under the assumption that it was the only variable source in the FOV. Although the observations of these GRBs were often incomplete (the ASM sometimes scanned away from a GRB in progress, as with GRB 961029), or suffered from poor statistics (as with GRB 961230 or GRB 971024), they were all in isolated regions of the sky where this technique could be reliably applied. In nine cases, the count rate from either BATSE or the *BeppoSAX* GRBM was available to compare the X-ray behavior of a burst with that of its high-energy counterpart.

GRB 960416 has two clearly defined, bright bursts, and inspection of their widths over the six available energy channels between 2 and 320 keV shows that both peaks are wider at lower energies. In fact, the dependence of width on energy is consistent with $E^{-1/2}$, as would be expected if the radiation mechanism were synchrotron radiation. A 1995 study of 45 peaks in BATSE bursts showed that the width of individual peaks goes as $E^{-0.4}$ [25], but GRB 960416 is only the second GRB where this analysis has been extended into the X-ray regime. Piro et al. (1998) found the singly-peaked burst GRB 960720 to widen as $E^{-0.46}$ [123], and GRB 960416 shows that this dependence can also apply to multiple peaks within the same burst.

Also intriguing are the episodes of X-ray emission with no corresponding gamma-ray activity. The final peak of GRB 970815 may actually represent a transition to the afterglow. The soft lag in the time of peak emission is consistent with a $t^{-3/2}$ delay, as predicted by the synchrotron shock model. The final decay is achromatic, also predicted in an external shock, and the decay rate is consistent with measured afterglow decay rates from other GRBs. This result, indicates that the cause of

individual peaks within a GRB may continue erratically throughout the entire event. Outbursts late in the afterglow decay curve have been interpreted as emission from collisions ejected at late times [122]. This highlights the importance of improved temporal coverage of more GRBs, to look for outbursts over the entire decay process.

The X-ray widths of other GRBs (GRB 970828 and GRB 971214) are clearly inconsistent with a $E^{-1/2}$ scaling from gamma-ray energies. Since these bursts are also the two most complex bursts in this sample, with many tiny bursts on small time-scales, this result can be understood in the context of the internal shock model, where the small peaks in the gamma-rays reflect the collision of ejecta shells within the expanding fireball. These shocks do not have time to cool enough to fade in the X-rays before they are shocked again. The rapid decay of ASM light curves for these bursts is also more consistent with internal shocks than the smooth fading expected from external shocks, so the tail of X-ray emission in these cases is most likely unrelated to an X-ray afterglow.

This work has provided the opportunity for the community to discover important results about the origin and behavior of GRBs from broad-band follow-up studies made possible by the rapid distribution of accurate localizations. It has also interpreted the X-ray behavior of these bursts in the context of the current most popular models for GRB emission, and provided support for the presence of synchrotron emission in bursts. It also suggests that both internal and external shocks may account for individual peaks during bursts and indicates that outbursts from a refreshed external shock may occur throughout the entire evolution of a GRB event.

Appendix A

Observational Parameters

This appendix contains data relevant to interpreting the ASM light curves presented in Chapter 7. Table A-1 contains the physical parameters for each ASM observation of a GRB: the field of view (FOV) location of the burst in terms of the FOV coordinates θ and ϕ (See Fig. 3-4 for a definition of the FOV coordinates.), the fractional area of the detector face exposed to the source, and a normalizing coefficient for each energy band. The latter two numbers correspond to f and a in Equation 3.2, respectively.

Tables A-2 through A-14 present the predicted average time-series count rate from every source in the FOV during a given observation. These count rates are derived from fits to the position histogram data. For diffuse backgrounds, the count rates are derived directly from the fit, but for discrete sources, the software automatically normalizes the amplitude of each source vector (See section 3.3.1) to yield an intrinsic source intensity at the center of the FOV of SSC 1. The contribution of each source to the total detected count rate in an SSC can be recovered by multiplying by the transmission factor and dividing by the normalization factor. For example, the position histogram fit for the single observation of GRB 981220 yields a normalized average intensity in the sum band over the 90-s observation of 37.1 $\pm$ 1.4 c/s. The transmission fraction at the GRB's FOV location is 0.59, and the normalizing factor for the sum band is 1.16. The prediction is therefore that GRB 981220 will contribute

an average of 18.8±0.7 c/s to the time series data (Table A-14). Identical calculations were performed for all detectable sources in the FOV of each observation.

The recovery of the GRB light curves at time scales shorter than 90 s (as described in Section 3.3.2) depends on the assumption that the GRB is the only variable source in the FOV during any given observation. Tables A-2 through A-14 show all the sources in the ASM FOV during the GRB observations, and none of them is known to vary dramatically on short time scales. The assumption is therefore reasonable, and the resulting GRB light curves are trustworthy.

GRB (YYMMDD)	Dwell No.	SSC No.	Theta (Degrees)	Phi (Degrees)	Trans. Fract.	Norm. S Band	Norm. A Band	Norm. B Band	Norm. C Band
960416	1	1	-6.284	2.012	0.669	1.0119	0.9664	0.9893	1.0593
960416	1	2	-6.562	-0.697	0.765	1.1195	1.4741	1.0299	0.9544
960529	1	1	6.820	2.502	0.572	1.0226	0.9932	0.9993	1.0491
960529	1	2	5.226	5.055	0.190	1.1849	1.5848	1.0966	0.9812
960529	2	1	5.570	-3.415	0.414	1.0570	1.0630	1.0288	1.0511
960529	2	2	6.468	-0.841	0.730	1.1236	1.4805	1.0338	0.9570
960727	1	2	27.476	0.093	0.710	1.1962	1.7147	1.0910	0.9738
961002	1	2	27.417	-1.600	0.551	1.1713	1.6609	1.0764	0.9527
961019	1	2	23.537	-4.501	0.237	1.2471	1.7445	1.1475	1.0081
961029	1	2	-8.192	4.009	0.303	1.1699	1.5655	1.0814	0.9734
961230	1	1	3.027	-0.742	0.837	1.0061	1.1084	0.9791	0.9322
961230	1	2	3.064	0.564	0.849	1.1174	1.4726	1.0283	0.9532
970815	1	2	-7.467	3.874	0.339	1.1710	1.5687	1.0825	0.9746
970815	2	1	-6.516	0.646	0.834	1.0132	1.2646	0.9835	0.8585
970815	2	2	-6.221	-2.044	0.598	1.1607	1.5403	1.0688	0.9799
970815	3	1	-7.757	-5.241	0.158	1.1284	1.4586	1.0888	0.9096
970828	1	1	-28.221	1.061	0.632	1.0488	1.3945	1.0162	0.8548
970828	2	2	-27.282	-5.483	0.076	1.2917	1.8578	1.1886	1.0230
970828	3	2	-28.529	0.413	0.704	1.1675	1.6779	1.0701	0.9478
971024	1	1	-5.027	-0.409	0.872	1.0363	1.3596	1.0016	0.8517
971024	1	2	-10.339	-4.125	0.238	1.2234	1.6440	1.1271	1.0152
971214	1	3	13.959	-1.366	0.525	1.0950	1.7493	1.0056	0.8338
980703	1	1	5.081	-0.476	0.871	1.0431	1.6421	1.0053	0.7788
980703	1	2	4.836	1.635	0.658	1.1369	1.5112	1.0486	0.9609
980703	2	1	6.327	5.433	0.137	1.1177	1.6880	1.0802	0.8390
981220	1	2	24.183	1.399	0.586	1.1551	1.6190	1.0640	0.9471

Table A-1: Observational Parameters for GRBs

Dwell No.	SSC No.	Name	Sum Rate (c/s)	A Rate (c/s)	B Rate (c/s)	C Rate (c/s)
1	1	Prtcle. BG	5.6 ± 0.5	0.1 ± 0.4	0.8 ± 0.4	4.5 ± 0.5
1	1	Diff X-ray	26.2 ± 1.2	6.6 ± 0.6	6.9 ± 0.6	12.6 ± 0.7
1	1	Tycho SNR	1.1 ± 0.6	0.8 ± 0.3	0.3 ± 0.3	0.0 ± 0.4
1	1	Cas A	1.0 ± 0.3	0.6 ± 0.2	0.6 ± 0.2	0.0 ± 0.2
1	1	GRB 960416	12.1 ± 0.6	3.2 ± 0.3	4.0 ± 0.3	5.0 ± 0.4
1	2	Prtcle. BG	4.1 ± 0.5	0.1 ± 0.4	0.6 ± 0.4	3.3 ± 0.4
1	2	Diff X-ray	22.6 ± 1.0	4.3 ± 0.5	5.9 ± 0.5	12.3 ± 0.8
1	2	X 0142+614	0.4 ± 0.6	0.3 ± 0.2	0.0 ± 0.3	0.2 ± 0.4
1	2	GRB 960416	12.8 ± 0.7	1.8 ± 0.3	4.0 ± 0.3	7.0 ± 0.5

Table A-2: Sources of Counts in ASM Observations of GRB 960416

Dwell No.	SSC No.	Name	Sum Rate (c/s)	A Rate (c/s)	B Rate (c/s)	C Rate (c/s)
1	1	Prtcle. BG	4.4 ± 0.5	0.2 ± 0.4	0.5 ± 0.4	3.3 ± 0.4
1	1	Diff X-ray	22.5 ± 0.9	5.4 ± 0.5	6.7 ± 0.5	10.5 ± 0.7
1	1	Tycho SNR	0.0 ± 0.3	0.2 ± 0.2	0.0 ± 0.2	0.0 ± 0.2
1	1	Cas A	2.2 ± 0.4	1.2 ± 0.2	0.3 ± 0.2	0.7 ± 0.3
1	1	GRB 960529	11.8 ± 0.5	3.8 ± 0.3	3.4 ± 0.3	4.5 ± 0.4
1	2	Prtcle. BG	3.4 ± 0.4	0.0 ± 0.4	0.2 ± 0.4	3.0 ± 0.4
1	2	Diff X-ray	20.2 ± 1.0	4.7 ± 0.5	5.9 ± 0.5	9.4 ± 0.6
1	2	Tycho SNR	0.7 ± 0.5	0.8 ± 0.2	0.1 ± 0.2	0.0 ± 0.4
1	2	Gamma Cas	1.2 ± 0.5	0.7 ± 0.2	0.0 ± 0.2	0.7 ± 0.3
1	2	GRB 960529	3.5 ± 0.3	0.8 ± 0.1	0.8 ± 0.1	1.9 ± 0.2
2	1	Prtcle. BG	4.4 ± 0.5	0.3 ± 0.4	0.8 ± 0.4	3.1 ± 0.4
2	1	Diff X-ray	22.4 ± 1.1	5.7 ± 0.6	6.4 ± 0.6	10.3 ± 0.7
2	1	Tycho SNR	0.5 ± 0.6	0.6 ± 0.3	0.0 ± 0.3	0.0 ± 0.4
2	1	Gamma Cas	1.1 ± 0.4	0.3 ± 0.2	0.4 ± 0.2	0.6 ± 0.3
2	1	GRB 960529	12.2 ± 0.5	3.4 ± 0.3	3.9 ± 0.3	5.1 ± 0.4
2	2	Prtcle. BG	3.6 ± 0.4	0.1 ± 0.4	0.2 ± 0.4	3.1 ± 0.4
2	2	Diff X-ray	19.5 ± 0.8	4.5 ± 0.5	5.5 ± 0.5	9.3 ± 0.6
2	2	Gamma Cas	0.0 ± 0.3	0.0 ± 0.1	0.0 ± 0.1	0.0 ± 0.2
2	2	GRB 960529	19.2 ± 0.7	3.9 ± 0.3	6.1 ± 0.4	9.2 ± 0.5

Table A-3: Sources of Counts in ASM Observations of GRB 960529

Dwell No.	SSC No.	Name	Sum Rate (c/s)	A Rate (c/s)	B Rate (c/s)	C Rate (c/s)
1	2	Prtcle. BG	2.3 ± 0.4	0.0 ± 0.4	0.1 ± 0.4	2.0 ± 0.4
1	2	Diff X-ray	31.3 ± 1.3	13.2 ± 0.8	6.3 ± 0.6	11.9 ± 0.8
1	2	uxari	0.3 ± 0.4	0.3 ± 0.3	0.1 ± 0.2	0.0 ± 0.3
1	2	X Per	1.8 ± 0.7	0.2 ± 0.4	0.7 ± 0.3	0.9 ± 0.4
1	2	GRB 960727	16.9 ± 0.8	3.1 ± 0.4	4.3 ± 0.4	9.4 ± 0.5

Table A-4: Sources of Counts in ASM Observations of GRB 960727

Dwell No.	SSC No.	Name	Sum Rate (c/s)	A Rate (c/s)	B Rate (c/s)	C Rate (c/s)
1	2	Prtcle. BG	3.2 ± 0.4	0.1 ± 0.4	0.1 ± 0.4	2.8 ± 0.4
1	2	Diff X-ray	28.3 ± 0.8	6.4 ± 0.5	7.2 ± 0.5	14.8 ± 0.7
1	2	GRB 961002	12.6 ± 0.6	1.8 ± 0.3	3.4 ± 0.3	7.5 ± 0.5

Table A-5: Sources of Counts in ASM Observations of GRB 961002

Dwell No.	SSC No.	Name	Sum Rate (c/s)	A Rate (c/s)	B Rate (c/s)	C Rate (c/s)
1	2	Prtcle. BG	3.7 ± 0.4	0.1 ± 0.4	0.3 ± 0.4	3.1 ± 0.4
1	2	Diff X-ray	31.1 ± 1.3	6.8 ± 0.5	7.2 ± 0.6	16.1 ± 0.9
1	2	XTEJ0111.2-7317	0.2 ± 0.7	0.0 ± 0.3	0.0 ± 0.3	0.6 ± 0.5
1	2	SMC X-1	0.7 ± 0.6	0.0 ± 0.3	0.1 ± 0.3	0.8 ± 0.5
1	2	ic4329a	0.6 ± 0.5	0.4 ± 0.2	0.3 ± 0.2	0.0 ± 0.4
1	2	GRB 961019	2.9 ± 0.4	0.8 ± 0.2	0.8 ± 0.2	1.2 ± 0.3

Table A-6: Sources of Counts in ASM Observations of GRB 961019

Dwell No.	SSC No.	Name	Sum Rate (c/s)	A Rate (c/s)	B Rate (c/s)	C Rate (c/s)
1	2	Prtcle. BG	3.8 ± 0.4	0.0 ± 0.4	0.1 ± 0.4	3.4 ± 0.4
1	2	Diff X-ray	25.0 ± 0.7	5.0 ± 0.5	7.2 ± 0.4	12.7 ± 0.6
1	2	hr1099	0.2 ± 0.2	0.0 ± 0.1	0.0 ± 0.1	0.2 ± 0.2
1	2	GRB 961029	2.4 ± 0.3	0.3 ± 0.1	0.7 ± 0.2	1.4 ± 0.3

Table A-7: Sources of Counts in ASM Observations of GRB 961029

Dwell No.	SSC No.	Name	Sum Rate (c/s)	A Rate (c/s)	B Rate (c/s)	C Rate (c/s)
1	1	Prtcle. BG	4.1 ± 0.5	0.2 ± 0.4	0.4 ± 0.4	3.3 ± 0.4
1	1	Diff X-ray	28.4 ± 0.9	6.7 ± 0.5	8.1 ± 0.5	13.8 ± 0.7
1	1	GRB 961230	3.9 ± 0.6	1.3 ± 0.3	1.1 ± 0.3	1.5 ± 0.4
1	2	Prtcle. BG	3.0 ± 0.4	0.0 ± 0.4	0.0 ± 0.4	0.0 ± 0.4
1	2	Diff X-ray	26.8 ± 0.9	6.2 ± 0.4	7.1 ± 0.4	15.8 ± 0.7
1	2	GRB 961230	3.4 ± 0.6	0.9 ± 0.3	1.1 ± 0.3	1.4 ± 0.4

Table A-8: Sources of Counts in ASM Observations of GRB 961230

Dwell No.	SSC No.	Name	Sum Rate (c/s)	A Rate (c/s)	B Rate (c/s)	C Rate (c/s)
1	1	Prtcle. BG	3.1 ± 0.4	0.0 ± 0.4	0.0 ± 0.4	0.0 ± 0.4
1	1	Diff X-ray	25.3 ± 0.8	5.7 ± 0.4	6.6 ± 0.4	15.5 ± 0.6
1	1	Cas A	3.6 ± 0.5	1.7 ± 0.3	1.3 ± 0.3	0.5 ± 0.4
1	2	Prtcle. BG	3.5 ± 0.4	0.1 ± 0.4	0.2 ± 0.4	2.8 ± 0.4
1	2	Diff X-ray	20.1 ± 1.0	4.4 ± 0.4	5.3 ± 0.6	10.6 ± 0.8
1	2	Tycho SNR	1.1 ± 0.4	0.4 ± 0.2	0.0 ± 0.2	0.6 ± 0.3
1	2	Gamma Cas	0.6 ± 0.5	0.0 ± 0.2	0.2 ± 0.2	0.5 ± 0.4
1	2	x0115+634	0.4 ± 0.4	0.0 ± 0.2	0.4 ± 0.2	0.1 ± 0.3
1	2	GRB 970815	9.6 ± 0.5	1.7 ± 0.2	2.8 ± 0.2	5.1 ± 0.4
2	1	Prtcle. BG	3.7 ± 0.4	0.1 ± 0.4	0.2 ± 0.4	3.1 ± 0.4
2	1	Diff X-ray	22.3 ± 1.2	4.9 ± 0.6	5.4 ± 0.6	12.1 ± 0.9
2	1	e2259+586snr	0.6 ± 0.9	0.1 ± 0.4	0.1 ± 0.4	0.5 ± 0.7
2	1	Cas A	1.0 ± 0.3	0.5 ± 0.2	0.2 ± 0.1	0.2 ± 0.2
2	1	GRB 970815	55.3 ± 1.0	15.9 ± 0.5	17.7 ± 0.5	21.8 ± 0.7
2	2	Prtcle. BG	3.3 ± 0.4	0.4 ± 0.4	0.3 ± 0.4	2.5 ± 0.4
2	2	Diff X-ray	19.6 ± 0.8	4.1 ± 0.4	5.2 ± 0.4	10.5 ± 0.6
2	2	Gamma Cas	0.2 ± 0.2	0.1 ± 0.1	0.0 ± 0.1	0.1 ± 0.2
2	2	GRB 970815	33.2 ± 0.8	9.3 ± 0.4	10.9 ± 0.4	13.1 ± 0.5
3	1	Prtcle. BG	3.7 ± 0.4	0.2 ± 0.4	0.1 ± 0.4	3.2 ± 0.4
3	1	Diff X-ray	25.4 ± 0.7	5.4 ± 0.4	7.3 ± 0.4	12.8 ± 0.6
3	1	Cep X-4	0.1 ± 0.3	0.0 ± 0.1	0.1 ± 0.1	0.1 ± 0.2
3	1	GRB 970815	0.3 ± 0.2	0.1 ± 0.1	0.0 ± 0.1	0.2 ± 0.2
3	2	Prtcle. BG	3.3 ± 0.4	0.1 ± 0.4	0.5 ± 0.4	2.5 ± 0.4
3	2	Diff X-ray	21.1 ± 0.8	4.1 ± 0.4	6.3 ± 0.4	10.8 ± 0.6
3	2	e2259+586snr	0.3 ± 0.3	0.3 ± 0.1	0.0 ± 0.1	0.1 ± 0.2
3	2	Cas A	1.4 ± 0.4	0.7 ± 0.2	0.2 ± 0.2	0.5 ± 0.3

Table A-9: Sources of Counts in ASM Observations of GRB 970815

Dwell No.	SSC No.	Name	Sum Rate (c/s)	A Rate (c/s)	B Rate (c/s)	C Rate (c/s)
1	1	Prtcle. BG	3.1 ± 0.4	0.2 ± 0.4	0.1 ± 0.4	2.7 ± 0.4
1	1	Diff X-ray	28.9 ± 1.3	5.1 ± 0.6	8.3 ± 0.7	15.7 ± 1.0
1	1	GRO J2058+42	0.7 ± 0.6	0.3 ± 0.2	0.0 ± 0.3	0.2 ± 0.4
1	1	Cyg X-2	19.9 ± 0.7	4.6 ± 0.3	6.5 ± 0.4	8.9 ± 0.5
1	1	GRB 970828	15.2 ± 0.8	1.4 ± 0.3	2.8 ± 0.4	11.0 ± 0.6
1	2	Prtcle. BG	3.1 ± 0.4	0.0 ± 0.4	0.0 ± 0.4	0.0 ± 0.4
1	2	Diff X-ray	26.8 ± 0.8	4.7 ± 0.4	7.9 ± 0.4	16.4 ± 0.5
1	2	Cyg X-3	0.2 ± 0.2	0.0 ± 0.1	0.0 ± 0.1	0.4 ± 0.1
1	2	GRO J2058+42	0.0 ± 0.4	0.0 ± 0.2	0.2 ± 0.2	0.0 ± 0.3
1	2	Cyg X-2	19.4 ± 0.6	4.6 ± 0.3	6.7 ± 0.4	8.0 ± 0.4
2	1	Prtcle. BG	3.4 ± 0.4	0.0 ± 0.4	0.0 ± 0.4	0.0 ± 0.4
2	1	Diff X-ray	28.3 ± 0.8	5.5 ± 0.3	7.2 ± 0.3	18.3 ± 0.5
2	1	Cyg X-2	15.1 ± 0.5	3.5 ± 0.2	5.3 ± 0.3	6.2 ± 0.4
2	2	Prtcle. BG	3.4 ± 0.4	0.0 ± 0.4	0.0 ± 0.4	0.0 ± 0.4
2	2	Diff X-ray	26.8 ± 0.7	5.1 ± 0.2	7.6 ± 0.3	16.8 ± 0.5
2	2	GRB 970828	4.5 ± 0.3	0.7 ± 0.1	1.2 ± 0.1	2.8 ± 0.2
3	1	Prtcle. BG	2.6 ± 0.4	0.1 ± 0.4	0.1 ± 0.4	2.2 ± 0.4
3	1	Diff X-ray	27.8 ± 0.8	5.0 ± 0.4	7.8 ± 0.4	14.9 ± 0.7
3	1	Cep X-4	0.9 ± 0.5	0.6 ± 0.2	0.0 ± 0.2	0.6 ± 0.4
3	2	Prtcle. BG	3.6 ± 0.4	0.0 ± 0.4	0.2 ± 0.4	3.2 ± 0.4
3	2	Diff X-ray	25.3 ± 0.9	4.5 ± 0.4	6.4 ± 0.6	14.3 ± 0.7
3	2	GRB 970828	10.4 ± 0.7	2.6 ± 0.3	3.7 ± 0.4	4.2 ± 0.5

Table A-10: Sources of Counts in ASM Observations of GRB 970828

Dwell No.	SSC No.	Name	Sum Rate (c/s)	A Rate (c/s)	B Rate (c/s)	C Rate (c/s)
1	1	Prtcle. BG	3.2 ± 0.4	0.4 ± 0.4	0.2 ± 0.4	2.4 ± 0.4
1	1	Diff X-ray	27.7 ± 1.1	5.3 ± 0.5	7.4 ± 0.6	15.0 ± 0.9
1	1	mkn501	0.8 ± 0.5	0.1 ± 0.2	0.2 ± 0.3	0.6 ± 0.4
1	1	Her X-1	1.0 ± 0.4	0.1 ± 0.2	0.1 ± 0.2	0.9 ± 0.3
1	1	Cep X-4	0.1 ± 0.3	0.0 ± 0.1	0.0 ± 0.1	0.2 ± 0.2
1	1	GRB 971024	3.6 ± 0.6	0.5 ± 0.2	1.0 ± 0.3	2.1 ± 0.4
1	2	Prtcle. BG	3.4 ± 0.4	0.1 ± 0.4	0.1 ± 0.4	3.0 ± 0.4
1	2	Diff X-ray	25.2 ± 0.9	4.1 ± 0.5	7.3 ± 0.5	13.7 ± 0.7
1	2	hd154791cv	1.7 ± 0.5	0.3 ± 0.2	0.3 ± 0.3	1.2 ± 0.4
1	2	Cas A	0.1 ± 0.3	0.2 ± 0.1	0.0 ± 0.2	0.0 ± 0.2
1	2	GRB 971024	0.6 ± 0.3	0.1 ± 0.1	0.1 ± 0.1	0.4 ± 0.2

Table A-11: Sources of Counts in ASM Observations of GRB 971024

Dwell No.	SSC No.	Name	Sum Rate (c/s)	A Rate (c/s)	B Rate (c/s)	C Rate (c/s)
1	3	Prtcle. BG	1.7 ± 0.3	0.0 ± 0.3	0.0 ± 0.3	0.0 ± 0.3
1	3	Diff X-ray	19.7 ± 0.7	3.7 ± 0.4	5.1 ± 0.3	12.3 ± 0.5
1	3	GRB 971214	5.0 ± 0.5	0.8 ± 0.2	1.2 ± 0.2	3.0 ± 0.4

Table A-12: Sources of Counts in ASM Observations of GRB 971214

Dwell No.	SSC No.	Name	Sum Rate (c/s)	A Rate (c/s)	B Rate (c/s)	C Rate (c/s)
1	1	Prtcle. BG	3.0 ± 0.4	0.0 ± 0.4	0.0 ± 0.4	0.0 ± 0.4
1	1	Diff X-ray	25.4 ± 0.9	4.0 ± 0.3	6.7 ± 0.4	17.2 ± 0.6
1	1	GRB 980703	17.7 ± 0.7	1.8 ± 0.3	4.4 ± 0.4	11.5 ± 0.6
1	2	Prtcle. BG	3.3 ± 0.4	0.0 ± 0.4	0.0 ± 0.4	0.0 ± 0.4
1	2	Diff X-ray	24.9 ± 0.8	4.8 ± 0.3	7.1 ± 0.4	15.8 ± 0.5
1	2	GRB 980703	13.9 ± 0.6	1.8 ± 0.2	3.7 ± 0.3	8.3 ± 0.5
2	1	Prtcle. BG	2.4 ± 0.4	0.0 ± 0.4	0.0 ± 0.4	0.0 ± 0.4
2	1	Diff X-ray	26.9 ± 0.7	4.2 ± 0.3	7.3 ± 0.3	17.3 ± 0.5
2	1	GRB 980703	4.3 ± 0.3	0.8 ± 0.1	1.0 ± 0.1	2.5 ± 0.2
2	2	Prtcle. BG	2.8 ± 0.4	0.2 ± 0.4	0.0 ± 0.4	0.0 ± 0.4
2	2	Diff X-ray	24.7 ± 0.7	4.5 ± 0.4	6.8 ± 0.3	15.2 ± 0.4

Table A-13: Sources of Counts in ASM Observations of GRB 980703

Dwell No.	SSC No.	Name	Sum Rate (c/s)	A Rate (c/s)	B Rate (c/s)	C Rate (c/s)
1	2	Prtcle. BG	3.1 ± 0.4	0.0 ± 0.4	0.2 ± 0.4	2.7 ± 0.4
1	2	Diff X-ray	25.3 ± 0.9	4.4 ± 0.4	7.2 ± 0.5	13.9 ± 0.7
1	2	Crab	11.2 ± 0.5	1.5 ± 0.2	3.8 ± 0.3	5.9 ± 0.4
1	2	GRB 981220	18.8 ± 0.7	2.5 ± 0.3	4.3 ± 0.4	12.0 ± 0.5

Table A-14: Sources of Counts in ASM Observations of GRB 981220

Bibliography

[1] A. Achterberg. Particle Acceleration Near Astrophysical Shocks. In Brickmann et al., editors, *Physical Processes in Hot Cosmic Plasmas,* page 67, 1990.

[2] A. Antonelli, R. Butler, L. Piro, G. Celidonio, A. Coletta, A. Tesseri, and C. De Libero. IAU Circ. No. 6792, 1997.

[3] J. L. Atteia, et al. A Second Catalog of Gamma-Ray Bursts - 1978-1980 Localizations from the Interplanetary Network. *The Astrophysical Journal Supplement Series,* **64**:305, 1987.

[4] J.-L. Atteia et al. Localization, Time Histories, and Energy Spectra of a New Type of Recurrent High-energy Transient Source. *The Astrophysical Journal,* **320**:105, 1987.

[5] D. Band, et al. Batse observations of gamma-ray burst spectra. i - spectral diversity. *The Astrophysical Journal,* **413**:281–292, 1993.

[6] C. Barat, G. Chambon, K. Hurley, M. Niel, and G. Vedrenne. The log N-log S Curve of Gamma-Ray Bursts Detected by the SIGNE Experiments. *Astronomy and Astrophysics,* **109**:L9, 1982.

[7] Philip R. Bevington. *Data Reduction and Error Analysis for the Physical Sciences.* McGraw-Hill Book Company, 1969.

[8] R. Blandford and C. McKee. Fluid Dynamics of Relativistic Blast Waves. *Phys. Fluids,* **19**:1130, 1976.

[9] J. Bloom et al. The unusual afterglow of grb 980326: evidence for the gamma-ray burst/supernova connection. *Nature,* 1999. in press.

[10] J. S. Bloom, et al. The Discovery and Broadband Follow-up of the Transient Afterglow of GRB 980703. *The Astrophysical Journal,* **508**:L21, 1998.

[11] H. V. Bradt, R. E. Rothschild, and J. H. Swank. X-ray Timing Explorer Mission. *Astronomy and Astrophysics Supplement Series,* **97**:355, 1993.

[12] G. Cavallo and M. J. Rees. A Qualitative Study of Cosmic Fireballs and Gamma-Ray Bursts. *Monthly Notices of the Royal Astronomical Society,* **183**:359, 1978.

[13] T. L. Cline, et al. Precise Source Location of the Anomalous 1979 March 5 Gamma-Ray Transient. *The Astrophysical Journal,* **255**:L45, 1982.

[14] S. A. Colgate. Early Gamma Rays from Supernovae. *The Astrophysical Journal,* **187**:333, 1974.

[15] A. Connors and G. J. Hueter. The X-Ray Characteristics of a Classical Gamma-Ray Burst and Its Afterglow. *The Astrophysical Journal,* **501**:307, 1998.

[16] E. Costa, et al. IAU Circ. No. 6576, 1997.

[17] E. Costa, et al. Discovery of an X-ray Afterglow Associated with the Gamma-ray Burst of 28 February 1997. *Nature,* page 783, 1997.

[18] F. Daigne and R. Mochkovitch. Gamma-ray Bursts from Internal Shocks in a Relativistic Wind: Temporal and Spectral Properties. *Monthly Notices of the Royal Astronomical Society,* **296**:275, 1998.

[19] A. Dar. GCN Circ. No. 346, 1999.

[20] C. D. Dermer, M. Boettcher, and J. Chiang. The External Shock Model of Gamma-Ray Bursts: Three Predictions and a Paradox Resolved. *The Astrophysical Journal,* **515**:L49, 1999.

[21] S. Djorgovski. Oral presentation, 1999. `http://www.itp.ucsb.edu/online/gamma_c99/djorgovski/`.

[22] S. Djorgovski, S. Kulkarni, J. Bloom, and D. Frail. GCN Circ. No. 289, 1999.

[23] S. Djorgovski, S. Kulkarni, J. Bloom, D. Frail, F. Chaffee, and R. Goodrich. GCN Circ. No. 189, 1998.

[24] S. Djorgovski, S. Kulkarni, R. Goodrich, D. Frail, and J. Bloom. GCN Circ. No. 137, 1998.

[25] E. Fenimore, J. in't Zand, J. Norris, J. Bonnell, and R. Nemiroff. Gamma-ray Burst Peak Duration as a Function of Energy. *The Astrophysical Journal,* **448**:L101, 1995.

[26] E. Fenimore, C. Madras, and S. Nayakshin. Expanding Relativistic Shells and Gamma-Ray Burst Temporal Structure. *The Astrophysical Journal,* **473**:998, 1996.

[27] E. Fenimore and E. Ramirez-Ruiz. The Observational Basis for Central Engines in Gamma-Ray Bursts. In *PASP Conf. Proc. Gamma-Ray Bursts: The First Three Minutes,* 1999. astro-ph/9906125.

[28] M. Feroci, et al. In-flight Performances of the BeppoSAX Gamma-ray Burst Monitor. In Siegmund and Gummin, editors, *SPIE Conference Proceedings,* volume 3114, page 186, 1997. astro-ph/9708168.

[29] G. Fishman et al. The First BATSE Gamma-Ray Burst Catalog. *The Astrophysical Journal Supplement Series,* **92**:229, 1994.

[30] G. Fishman and C. Meegan. Gamma-Ray Bursts. *Annual Reviews of Astronomy & Astrophysics,* **33**:415, 1995.

[31] G. J. Fishman, et al. The First BATSE Gamma-Ray Burst Catalog. *The Astrophysical Journal Supplement Series,* **92**:229, 1994.

[32] G. J. Fishman, et al. The BATSE Experiment on the Gamma Ray Observatory: Solar Flare, Hard X-ray, and Gamma-ray Capabilities. In *Developments in Observations and Theory for Solar Cycle 22,* page 96, 1989.

[33] E. Fomalont, R. Windhorst, J. Kristian, and K. Kellerman. The Micro-Jansky Radio Source Population at 5 GHz. *Astronomical Journal,* **102**:1258, 1991.

[34] D. Frail. Radio Counterparts of Gamma-Ray Bursts. In Meegan, Preece, and Koshut, editors, *Proceedings of 4th Huntsville GRB Symposium,* page 563, 1998.

[35] D. Frail. Afterglows: Near and Far. *American Astronomical Society, HEAD meeting #31, #01.01,* **31**:0101, 1999.

[36] D. Frail, J. Halpern, J. Bloom, S. Kulkarni, and S. Djorgovski. GCN Circ. No. 128, 1998.

[37] D. Frail and S. Kulkarni. GCN Circ. No. 170, 1998.

[38] D. Frail, S. Kulkarni, L. Nicastro, M. Feroci, and G. Taylor. The Radio Afterglow from the Gamma-ray Burst of 8 May 1997. *Nature,* **389**:261, 1997.

[39] D. Frail, S. Kulkarni, and G. Taylor. GCN Circ. No. 269, 1999.

[40] F. Frontera, E. Costa, D. Dal Fiume, M. Feroci, L. Nicastro, M. Orlandini, E. Palazzi, and G. Zavattini. The High Energy Instrument PDS On-board the BeppoSAX X-ray Astronomy Satellite. *Astronomy and Astrophysics Supplement Series,* **122**, 1997.

[41] F. Frontera, et al. Spectral Properties of the Prompt X-Ray Emission and Afterglow from the Gamma-ray Burst of 1997 February 28. *The Astrophysical Journal,* **493**:L67, 1998.

[42] A. Fruchter. Was GRB 980329 at z∼5? *The Astrophysical Journal,* **512**:L1, 1999.

[43] A. S. Fruchter, et al. The Fading Optical Counterpart of GRB 970228, 6 Months and 1 Year Later. *The Astrophysical Journal,* **516**:683, 1999.

[44] T. Galama, J. van Paradijs, L. Antonelli, P. Vreeswijk, C. Kouveliotou, V. Torroni, and C. Pastor. GCN Circ. No. 127, 1998.

[45] T. Galama, et al. GCN Circ. No. 338, 1999.

[46] T. Galama, P. Vreeswijk, J. van Paradijs, C. Kouveliotou, R. Strom, and G. de Bruyn. GCN Circ. No. 168, 1998.

[47] T. Galama, R. Wijers, M. Bremer, P. Groot, R. Strom, C. Kouveliotou, and J. van Paradijs. The Radio-to-X-Ray Spectrum of GRB 970508 on 1997 May 21.0 UT. *The Astrophysical Journal.* **500**:L97, 1998.

[48] S. V. Golenetskii. On the Spatial Distribution of Gamma-Ray Burst Sources. *Advances in Space Research.* **8**:653, 1988.

[49] J. Goodman. Are Gamma-Ray Bursts Optically Thick? *The Astrophysical Journal,* **308**:L47, 1986.

[50] J. Greiner. Gamma-Ray Bursts. World Wide Web, 1999. `http://www.aip.de:8080/ jcg/grbgen.html`.

[51] J. Greiner, R. Schwarz, P. Groot, and T. Galama. IAU Circ. No. 6757, 1997.

[52] P. Groot et al. A Search for Optical Afterglow from GRB 970828. *The Astrophysical Journal,* **493**:27, 1998.

[53] P. J. Groot, et al. The Rapid Decay of the Optical Emission from GRB 980326 and Its Possible Implications. *The Astrophysical Journal,* **502**:L123, 1998.

[54] D. E. Gruber, P. R. Blanco, W. A. Heindl, M. R. Pelling, R. E. Rothschild, and P. L. Hink. The High Energy X-ray Timing Experiment on XTE. *Astronomy and Astrophysics Supplement Series,* **120**:C641, 1996.

[55] J. Halpern, J. Thorstensen, D. Helfand, and E. Costa. IAU Circ. No. 6788, 1997.

[56] F. A. Harrison and S. E. Thorsett. Determining the Gamma-Ray Burst Distance Scale: Observational Prospects. *The Astrophysical Journal,* **460**:L99, 1996.

[57] M. Harwit and E. Salpeter. Radiation From Comets Near Neutron Stars. *The Astrophysical Journal,* **186**:L37, 1973.

[58] J. Heise et al. IAU Circ. No. 6787, 1997.

[59] J. Higdon and R. Lingenfelter. Gamma-ray Bursts. *Annual Reviews of Astronomy & Astrophysics,* **28**:401, 1990.

[60] J. C. Higdon and R. E. Lingenfelter. Size / frequency distribution of gamma-ray bursts from thermonuclear runaway on neutron stars accreting interstellar gas. In Woosley, editor, *High Energy Transients in Astrophysics,* page 568, 1984.

[61] J. Hjorth et al. GCN Circ. No. 219, 1999.

[62] D. W. Hogg and A. S. Fruchter. The Faint-Galaxy Hosts of Gamma-Ray Bursts. *The Astrophysical Journal,* **520**:54, 1999.

[63] J. Horack and C. Kouveliotou. "blasts from the Past". World Wide Web, 1998. `http://science.msfc.nasa.gov/newhome/headlines/ast06may98_1.htm`.

[64] K. Hurley. Cosmic Gamma-Ray Bursts. In Lewin, van Paradijs, and van den Heuvel, editors, *X-Ray Binaries,* volume 26 of *Cambridge Astrophysics Series,* chapter 13, page 523. Cambridge University Press, Cambridge, UK, 1995.

[65] K. Hurley. A Gamma-Ray Burst Bibliography, 1973-1997. In Meegan, Preece, and Koshut, editors, *Proceedings of 4th Huntsville GRB Symposium,* page 87, 1998.

[66] K. Hurley. A Gamma-Ray Burst Bibliography. World Wide Web, 1999. `http://ssl.berkeley.edu/ipn3/bibliogr.html`.

[67] K. Hurley. IPN3 Home Page. World Wide Web, 1999. `http://ssl.berkeley.edu/ipn3/`.

[68] K. Hurley, M. S. Briggs, R. M. Kippen, C. Kouveliotou, C. Meegan, G. Fishman, T. Cline, and M. Boer. The ULYSSES Supplement to the BATSE 3B Catalog of Cosmic Gamma-Ray Bursts. *The Astrophysical Journal Supplement Series,* **120**:399, 1999.

[69] K. Hurley, T. Cline, E. Mazets, S. Golenetskii, and D. Smith. GCN Circ. No. 160, 1998.

[70] K. Hurley et al. *The Astrophysical Journal,* 1999. *submitted.*

[71] K. Hurley and C. Kouveliotou. GCN Circ. No. 125, 1998.

[72] K. Hurley, C. Kouveliotou, G. Fishman, C. Meegan, V. Connaughton, and J. van Paradijs. IAU Circ. No. 6728, 1997.

[73] K. Hurley, C. Kouveliotou, P. Woods, E. Mazets, S. Golenetskii, D. D. Frederiks, T. Cline, and J. Van Paradijs. Precise Interplanetary Network Localization of a New Soft Gamma Repeater, SGR 1627-41. *The Astrophysical Journal,* **519**:L143, 1999.

[74] J. J. M. In 'T Zand, J. Heise, J. Van Paradijs, and E. E. Fenimore. The Prompt X-Ray Emission of Gamma-Ray Burst 980519. *The Astrophysical Journal,* **516**:L57, 1999.

[75] K. Jahoda, J. H. Swank, A. B. Giles, M. J. Stark, T. Strohmayer, W. Zhang, and E. H. Morgan. In-orbit Performance and Calibration of the Rossi X-ray Timing Explorer (RXTE) Proportional Counter Array (PCA). In Siegmund and Gummin, editors, *EUV, X-Ray, and Gamma-Ray Instrumentation for Astronomy VIII,* volume 2808, page 59, 1996.

[76] B. Jannuzi and J. Rhoads. GCN Circ. No. 3, 1997.

[77] D. Kelson, G. Illingworth, M. Franx, D. Magee, and P. van Dokkum. IAU Circ. No. 7096, 1999.

[78] R. Kippen, P. Woods, V. Connaughton, D. Smith, A. Levine, R. Remillard, and K. Hurley. IAU Circ. No. 6789, 1997.

[79] R. Klebesadel. The History of Gamma-Ray Burst Observations. In Tanaka, editor, *Physics of Neutron Stars and Black Holes,* page 387, 1988.

[80] R. Klebesadel, et al. A Catalog of Gamma-Ray Bursts with Earth Crossing Times. *The Astrophysical Journal,* **259**:L51, 1982.

[81] R. Klebesadel, I. Strong, and R. Olson. Observations of Gamma-Ray Bursts of Cosmic Origin. *The Astrophysical Journal,* **182**:L85, 1973.

[82] S. Kobayashi, T. Piran, and R. Sari. Can Internal Shocks Produce the Variability in Gamma-Ray Bursts? *The Astrophysical Journal,* **490**:92, 1997.

[83] S. Kobayashi, T. Piran, and R. Sari. Hydrodynamics of a Relativistic Fireball: The Complete Evolution. *The Astrophysical Journal,* **513**:669, 1999.

[84] T. M. Koshut, W. S. Paciesas, C. Kouveliotou, J. Van Paradijs, G. N. Pendleton, G. J. Fishman, and C. A. Meegan. Systematic Effects on Duration Measurements of Gamma-Ray Bursts. *The Astrophysical Journal,* **463**:570, 1996.

[85] C. Kouveliotou et al. SMM Hard X-ray Observations of the Soft Gamma-ray Repeater 1806-20. *The Astrophysical Journal,* **322**:21, 1987.

[86] C. Kouveliotou, C. A. Meegan, G. J. Fishman, N. P. Bhat, M. S. Briggs, T. M. Koshut, W. S. Paciesas, and G. N. Pendleton. Identification of two classes of gamma-ray bursts. *The Astrophysical Journal,* **413**:L101, 1993.

[87] S. R. Kulkarni, et al. Identification of a Host Galaxy at Redshift z = 3.42 for the Gamma-Ray Burst of 14 December 1997. *Nature,* **393**:35, 1998.

[88] S. R. Kulkarni, D. A. Frail, M. H. Wieringa, R. D. Ekers, E. M. Sadler, R. M. Wark, J. L. Higdon, E. S. Phinney, and J. S. Bloom. Radio Emission from the Unusual Supernova 1998bw and its Association with the Gamma-Ray Burst of 25 April 1998. *Nature,* **395**:663, 1998.

[89] J. Laros et al. A New Type of Repetitive Behavior in a High-energy Transient. *The Astrophysical Journal,* **320**:L111, 1987.

[90] J. G. Laros, W. D. Evans, E. E. Fenimore, R. W. Klebesadel, S. Shulman, and G. Fritz. 3 keV to 2 MeV Observations of Four Gamma-ray Bursts. *The Astrophysical Journal,* **286**:681, 1984.

[91] J. G. Laros, E. E. Fenimore, M. M. Fikani, R. W. Klebesadel, M. Van Der Klis, and M. Gottwald. GB 841215, the Fastest Gamma-Ray Burst? *Nature,* **318**:448, 1985.

[92] D. Lazzati, G. Ghisellini, and A. Celotti. Constraints on the Bulk Lorentz Factor in the Internal Shock Scenario for Gamma-Ray Bursts. *Monthly Notices of the Royal Astronomical Society,* 1999. in press, astro-ph/9907070.

[93] A. Levine, E. Morgan, and M. Muno. IAU Circ. No. 6966, 1998.

[94] A. M. Levine, H. Bradt, D. Chakrabarty, W. Cui, J. G. Jernigan, E. Morgan, R. Remillard, R. Shirey, and D. A. Smith. IAU Circ. No. 6390, 1996.

[95] W. Lewin, J. van Paradijs, and R. Taam. Cosmic Gamma-Ray Bursts. In Lewin, van Paradijs, and van den Heuvel, editors, *X-Ray Binaries,* volume 26 of *Cambridge Astrophysics Series,* chapter 4, page 175. Cambridge University Press, Cambridge, UK, 1995.

[96] H. Li and E. Fenimore. Log-normal Distributions in Gamma-Ray Burst Time Histories. *The Astrophysical Journal,* **469**:L115, 1996.

[97] H. Li, E. E. Fenimore, and E. P. Liang. Detectability of Gamma-Ray Burst Excess Toward M31. *The Astrophysical Journal,* **461**:L73, 1996.

[98] T. J. Loredo and I. M. Wasserman. Inferring the Spatial and Energy Distribution of Gamma-Ray Burst Sources. III. Anisotropic Models. *The Astrophysical Journal,* **502**:108, 1998.

[99] R. Malozzi and M. Briggs. BATSE Gamma-Ray Burst Skymap. World Wide Web, 1999. `http://www.batse.msfc.nasa.gov/batse/grb/skymap/`.

[100] F. Marshall, J. Cannizzo, and R. Corbet. IAU Circ. No. 6727, 1997.

[101] E. P. Mazets, et al. Catalog of Cosmic Gamma-Ray Bursts from the KONUS Experiment Data. I, II, III, IV. *Astrophysics & Space Science,* **80**:3, 1981.

[102] C. Meegan et al. The Third BATSE Gamma-Ray Burst Catalog. *The Astrophysical Journal Supplement Series,* **106**:65, 1996.

[103] C. A. Meegan, et al. Current BATSE Gamma-Ray Burst Catalog. World Wide Web, 1999. `http://www.batse.msfc.nasa.gov/data/grb/catalog/`.

[104] P. Mészáros and M. Rees. Tidal Heating and Mass Loss in Neutron Star Binaries - Implications for Gamma-Ray Burst Models. *The Astrophysical Journal,* **397**:570, 1992.

[105] P. Mészáros and M. Rees. Optical and Long-Wavelength Afterglow From Gamma-Ray Bursts. *The Astrophysical Journal,* **476**:232, 1997.

[106] A. E. Metzger, R. H. Parker, D. Gilman, L. E. Peterson, and J. I. Trombka. Observation of a Cosmic Gamma-ray Burst on Apollo 16. I - Temporal Variability and Energy Spectrum. *The Astrophysical Journal,* **194**:L19, 1974.

[107] M. Metzger, J. Cohen, F. Chaffee, and R. Blandford. IAU Circ. No. 6676, 1997.

[108] M. R. Metzger, S. G. Djorgovski, S. R. Kulkarni, C. C. Steidel, K. L. Adelberger, D. A. Frail, E. Costa, and F. Frontera. Spectral Constraints on the Redshift of the Optical Counterpart to the Gamma-ray Burst of 8 May 1997. *Nature,* **387**:879, 1997.

[109] C. Motch, S. A. Ilovaisky, C. Chevalier, H. Pedersen, K. Hurley, and G. Pizzichini. The Optical Content of the 1979 April 6 Gamma-Ray Burst Error Box. *Astronomy and Astrophysics,* **145**:201, 1985.

[110] T. Murakami, et al. The Gamma-ray Burst Detector System on Board Ginga. *Publications of the Astronomical Society of Japan,* **41**:405, 1989.

[111] T. Murakami, H. Inoue, J. Nishimura, J. Van Paradijs, and E. E. Fenimore. A Gamma-Ray Burst Preceded by X-ray Activity. *Nature,* **350**:592, 1991.

[112] T. Murakami, J. Nishimura, N. Kawai, B. A. Cooke, and M. Katoh. Ginga X-ray Observations of Two Gamma-Ray Burst Error Boxes. *Astronomy and Astrophysics,* **227**:451, 1990.

[113] T. Murakami, Y. Ueda, M. Ishida, R. Fujimoto, A. Yoshida, and N. Kawai. IAU Circ. No. 6722, 1997.

[114] T. Murakami, Y. Ueda, A. Yoshida, N. Kawai, F. Marshall, R. Corbet, and T. Takeshima. IAU Circ. No. 6732, 1997.

[115] R. Narayan, B. Paczyński, and T. Piran. Gamma-ray Bursts as the Death Throes of Massive Binary Stars. *The Astrophysical Journal,* **395**:L83, 1992.

[116] L. Nicastro et al. BeppoSAX Observations of GRB 970402. *Astronomy and Astrophysics,* **338**:L17, 1998.

[117] Y. Ogasaka, T. Murakami, J. Nishimura, A. Yoshida, and E. E. Fenimore. V/V(max) Test Applied to Ginga Gamma-ray Bursts. *The Astrophysical Journal,* **383**:L61, 1991.

[118] W. S. Paciesas, et al. BATSE 4B Gamma-Ray Burst Catalog. *The Astrophysical Journal Supplement Series,* 1999. astro-ph/9903205. Also at `http://www.batse.msfc.nasa.gov/batse/grb/catalog/4b/`.

[119] B. Paczyński. Gamma-Ray Bursters at Cosmological Distances. *The Astrophysical Journal,* **308**:L43, 1986.

[120] T. Piran. Gamma-Ray Bursts and the Fireball Model. *Physics Reports,* **314**(6):575, 1999. astro-ph/9810256.

[121] T. Piran, A. Shemi, and R. Narayan. Hydrodynamics of Relativistic Fireballs. *Monthly Notices of the Royal Astronomical Society,* **263**:861, 1993.

[122] L. Piro et al. Evidence for a Late-Time Outburst of the X-ray Afterglow of GRB 970508 from BeppoSAX. *Astronomy and Astrophysics,* **331**:L41, 1998.

[123] L. Piro, et al. The First X-ray Localization of a Gamma-ray Burst by BeppoSAX and its Fast Spectral Evolution. *Astronomy and Astrophysics,* **329**:906, 1998.

[124] R. D. Preece, M. S. Briggs, G. N. Pendleton, W. S. Paciesas, J. L. Matteson, D. L. Band, R. T. Skelton, and C. A. Meegan. BATSE Observations of Gamma-Ray Burst Spectra. III. Low-Energy Behavior of Time-averaged Spectra. *The Astrophysical Journal,* **473**:310, 1996.

[125] M. Rees. Appearance of Relativistically Expanding Radio Sources. *Nature,* **211**:468, 1966.

[126] M. Rees and P. Mészáros. Relativistic Fireballs - Energy Conversion and Timescales. *Monthly Notices of the Royal Astronomical Society,* **258**:41, 1992.

[127] M. Rees and P. Mészáros. Refreshed Shocks and Afterglow Longevity in Gamma-Ray Bursts. *The Astrophysical Journal,* **496**:L1, 1998.

[128] D. Reichert. GRB 970228 Revisited: Evidence for a Supernova in the Light Curve and Late Spectral Energy Distribution of the Afterglow. *The Astrophysical Journal,* 1999. in press.

[129] R. Remillard, A. Wood, D. Smith, and A. Levine. IAU Circ. No. 6726, 1997.

[130] E. Richards, K. Kellermann, E. Fomalont, R. Windhorst, and R. Partridge. Radio Emission from Galaxies in the Hubble Deep Field. *Astronomical Journal,* **116**:1039, 1998.

[131] G. Rybicki and A. Lightman. *Radiative Processes in Astrophysics.* John Wiley & Sons, New York, 1979.

[132] R. Sari, R. Narayan, and T. Piran. Cooling Timescales and Temporal Structure of Gamma-Ray Bursts. *The Astrophysical Journal,* **473**:204, 1996.

[133] R. Sari and T. Piran. Hydrodynamic Timescales and Temporal Structure of Gamma-Ray Bursts. *The Astrophysical Journal,* **455**:L143, 1995.

[134] R. Sari and T. Piran. Cosmological Gamma-ray Bursts: Internal Versus External Shocks. *Monthly Notices of the Royal Astronomical Society,* **287**:110, 1997.

[135] R. Sari, T. Piran, and R. Narayan. Spectra and Light Curves of Gamma-Ray Burst Afterglows. *The Astrophysical Journal,* **497**:L17, 1998.

[136] S. Y. Sazonov, R. A. Sunyaev, O. V. Terekhov, N. Lund, S. Brandt, and A. J. Castro-Tirado. GRANAT/WATCH Catalogue of Cosmic Gamma-ray Bursts: December 1989 to September 1994. *Astronomy and Astrophysics Supplement Series,* **129**:1, 1998.

[137] B. E. Schaefer, et al. Gamma-Ray Burster Counterparts - Radio. *The Astrophysical Journal,* **340**:455, 1989.

[138] B. E. Schaefer, et al. Gamma-Ray Burster Counterparts - Infrared. *The Astrophysical Journal,* **313**:226, 1987.

[139] L. Sedov. *Prikl. Mat. i Mekh.,* **10**:241, 1946.

[140] F. O. Seward. A Trip to the Crab Nebula. *Journal of the British Interplanetary Society,* **31**:83, 1978.

[141] N. Shaviv and A. Dar. Fireballs in Dense Stellar Regions as an Explanation of Gamma-ray Bursts. *Monthly Notices of the Royal Astronomical Society,* **277**:287, 1995.

[142] A. Shemi and T. Piran. The Appearance of Cosmic Fireballs. *The Astrophysical Journal,* **365**:L55, 1990.

[143] F. Shu. *The Physics of Astrophysics, Vol. II.* University Science Books, Mill Valley, CA, 1992.

[144] D. Smith, A. Levine, E. Morgan, and A. Wood. IAU Circ. No. 6718, 1997.

[145] D. Smith, R. Remillard, J. Swank, T. Takeshima, and E. Smith. IAU Circ. No. 6855, 1998.

[146] D. A. Smith. IAU Circ. No. 7008, 1998.

[147] D. A. Smith, et al. Localizations of Thirteen Gamma-ray Bursts by the All-Sky Monitor on RXTE. *The Astrophysical Journal,* 1999. in press, astro-ph/9907332.

[148] D. A. Smith, H. V. Bradt, and A. M. Levine. RXTE All-Sky Monitor Localization of SGR 1627–41. *The Astrophysical Journal,* **519**:L147, 1999.

[149] D. A. Smith, A. Levine, and A. Wood. IAU Circ. No. 6932, 1998.

[150] D. A. Smith, E. H. Morgan, and H. Bradt. Rossi X-Ray Timing Explorer Discovery of Coherent Millisecond Pulsations during an X-Ray Burst from KS 1731-260. *The Astrophysical Journal,* **479**:L137–+, 1997.

[151] D. A. Smith and T. Takeshima. IAU Circ. No. 7014, 1998.

[152] T. E. Strohmayer, E. E. Fenimore, T. Murakami, and A. Yoshida. X-Ray Spectral Characteristics of Ginga Gamma-Ray Bursts. *The Astrophysical Journal,* **500**:873, 1998.

[153] R. E. Taam and D. N. C. Lin. The Evolution of the Inner Regions of Viscous Accretion Disks Surrounding Neutron Stars. *The Astrophysical Journal,* **287**:761, 1984.

[154] M. Tavani. A Shock Emission Model for Gamma-Ray Bursts. II. Spectral Properties. *The Astrophysical Journal,* **466**:768, 1996.

[155] M. Tavani. X-Ray Emission of Gamma-Ray Bursts. *The Astrophysical Journal,* **480**:351, 1997.

[156] G. Taylor. *Proceedings of the Royal Society of London A,* **201**:159, 1950.

[157] G. Taylor, D. Frail, S. Kulkarni, D. Shepherd, M. Feroci, and F. Frontera. The Discovery of the Radio Afterglow from the Optically Dim Gamma-Ray Burst of 1998 March 29. *The Astrophysical Journal,* **502**:L115, 1998.

[158] C. Tinney, R. Stathakis, R. Cannon, and T. Galama. IAU Circ. No. 6896, 1998.

[159] J. I. Trombka, E. L. Eller, R. L. Schmadebeck, I. Adler, A. E. Metzger, D. Gilman, P. Gorenstein, and P. Bjorkholm. Observation of a Cosmic Gamma-ray Burst on Apollo 16. II - X-ray Time Profile and Source Location. *The Astrophysical Journal,* **194**:L27, 1974.

[160] J. Van Paradijs, et al. Transient Optical Emission from the Error Box of the Gamma-ray Burst of 28 February 1997. *Nature,* **386**:686, 1997.

[161] J. Villasenor. HETE - High Energy Transient Explorer. World Wide Web, 1999. `http://space.mit.edu/HETE/`.

[162] J. von Neumann. Technical Report 7, Los Alamos Sci. Lab. Tech. Ser., 1947.

[163] F. Vrba and J. Munn. GCN Circ. No. 2, 1997.

[164] P.M. Vreeswijk, et al. GCN Circ. No. 324, 1999.

[165] E. Waxman. Angular Size and Emission Timescales of Relativistic Fireballs. *The Astrophysical Journal,* **491**:L19, 1997.

[166] E. Waxman. Gamma-Ray Burst Afterglow: Confirming the Cosmological Fireball Model. *The Astrophysical Journal,* **489**:L33, 1997.

[167] E. Waxman, S. R. Kulkarni, and D. A. Frail. Implications of the Radio Afterglow from the Gamma-Ray Burst of 1997 May 8. *The Astrophysical Journal,* **497**:288, 1998.

[168] S. Weinberg. *Gravitation and Cosmology.* John Wiley & Sons, New York, 1973.

[169] W. A. Wheaton, et al. The direction and spectral variability of a cosmic gamma-ray burst. *The Astrophysical Journal,* **185**:L57, 1973.

[170] R. Wijers and T. Galama. Physical Parameters of GRB 970508 and GRB 971214 from their Afterglow Synchrotron Emission. *The Astrophysical Journal,* 1999. *submitted*, astro-ph/9805341.

[171] R. Wijers, M. Rees, and P. Mészáros. Shocked by GRB 970228: the Afterglow of a Cosmological Fireball. *Monthly Notices of the Royal Astronomical Society,* **288**:L51, 1997.

[172] P. M. Woods, C. Kouveliotou, J. Van Paradijs, K. Hurley, R. M. Kippen, M. H. Finger, M. S. Briggs, S. Dieters, and G. J. Fishman. Discovery of a New Soft Gamma Repeater, SGR 1627–41. *The Astrophysical Journal,* **519**:L139, 1999.

[173] A. Yoshida, M. Namiki, C. Otani, N. Kawai, T. Murakami, Y. Ueda, R. Shibata, and S. Uno. An X-ray Afterglow from GRB 970828 Observed with ASCA. In *Huntsville Gamma-Ray Burst Symposium,* page 441, 1998.

[174] Martin V. Zombeck. *Handbook of Space Astronomy and Astrophysics, Second Edition.* Cambridge University Press, Cambridge, UK, 1990.

THESIS PROCESSING SLIP

FIXED FIELD: ill. _____ name _____

index _____ biblio _____

▶ COPIES: (Archives) Aero Dewey Eng Hum

Lindgren Music Rotch (Science)

TITLE VARIES: ▶☐ _____

NAME VARIES: ▶☐ _____

IMPRINT: (COPYRIGHT) _____

▶ COLLATION: 191 P

▶ ADD: DEGREE: _____ ▶ DEPT.: _____

SUPERVISORS: _____

NOTES:

cat'r: date:

page: 556

▶ DEPT: Phy

▶ YEAR: 1999 ▶ DEGREE: Ph.D.

▶ NAME: SMITH Donald Andrew